Hybrid Photonic-Plasmonic Devices with Single Nanoscale Light Sources

Esteban Bermúdez Ureña

ICFO- The Institute of Photonic Sciences

Universitat Politècnica de Catalunya

Castelldefels (Barcelona), July 2017

Thesis committee:

Prof. Dr. Oliver Benson (Humboldt University Berlin, Germany)

Prof. Dr. Anatoly Zayats (Kings College London, United Kingdom)

Prof. Dr. Niek van Hulst (ICFO – The Institute of Photonic Sciences, Spain)

Hybrid Photonic-Plasmonic Devices with Single Nanoscale Light Sources

Esteban Bermúdez Ureña

under the supervision of

Prof. Dr. Romain Quidant

submitted this thesis in partial fulfillment
of the requirements for the degree of

Doctor

by the
Universitat Politècnica de Catalunya
Castelldefels (Barcelona), July 2017

To Dani, and my family.

Acknowledgements

The work and time spent during this thesis would not have been as successful and enjoyable without the help, support and presence of many people, both in and outside our institute.

ICFO is a great place and every year grows stronger as a research institution. I wouldn´t be surprised if in ten year it extends all the way to the beach. High impact publications aside, without a doubt, the pillars of ICFO's success are the people inside it, and I´m forever thankful to every member of ICFO´s community that made a positive impact, either on my work, or in my daily life over the past years.

First of all, I would like to thank Romain for giving me the opportunity to join his group but most importantly for providing his continuous support and guidance throughout my PhD. I´m very grateful to have had everything I needed during my PhD and I also thank him for providing the right amount of scientific freedom to carry my own ideas and lead projects with our collaborators. I highly esteem having Romain as my mentor over these years, thank you for all the patience and support.

Besides earning all the available grants, one of Romain´s achievements has been to select the right people to build a group with a great environment, my dear PNOs! Many have come and go during these years but I keep good memories of our times together. I was lucky to share my office with great people, starting from Giorgio and Srdjan, whom I also thank for their help and cleanroom training during my first stage of the PhD. Then came the second generation in the office with Ozlem and only Jose, it was always easy to have a laugh together. Finally came Mikael, whom I thank for all the nice discussions and his help during the last sprint of my PhD. Thank you all for making the office life enjoyable.

To the rest of past and present PNO members, thank you all who either helped me greatly during my project, like Mark, Michael, Renaud, Johann, Yury and Vanessa, or simply made lunch, coffee or beer times fun: Jan G, Jan R, Jay D, Mariale, Vale, Chris, Ignacio, Paulina, Pascal, Marko, Pau, Raul, LuisMi, Mathieu, Andreas, Nadine, fRaN, Irene, Mohammed, Gerard, Sebas, Alex, Laurent, Jaime, Vincenzo, Clara, Jordi, Ivan, Victor, Roger, Marc, Bea, and with such a long list I hope I didn´t miss someone important.

Special thanks all the ICFO staff that make everything run smoothly and facilitate the life for us. Starting from our director Lluis who´s vision and motivation has taken the institute as far as it goes, and Dolors for making sure it gets there. Infinite thanks go to the HR team lead by Laia, with a special mention to Manu, Mery, Anne and Cristina, thank you for always going the extra mile, and genially caring for us! Thanks to ever present Carlos who keeps ICFO running, and Jonas and Adria for all their logistics efforts. To Xavi´s, Jose Carlos´ and Goncal´s teams at the workshops and IT dept. for their prompt and reliable support. Also to the cleanroom team, Luis, Javi and Johann, thank you for the excellent work

you do in keeping the cleanroom operational. Also thanks to Santi and Magda at purchasing, Elena and Maria for help with travels, and Moni, Maria and Merce for starting our working days with a warm smile. As well as many others who were always willing to help and create a good atmosphere at ICFO (Esther, Rob, Rafa G, Javi E, Thomas, Silvia, Ferran, Alina, Brook, etc).

During my PhD I was honoured to take part of several successful collaborations, all of which enriched me as a researcher. In particular, I would like to kindly acknowledge those whom I actively interacted with and gained knowledge from through our discussions: Jerome Wenger and Guillaume Baffou from the Fresnel Institute; Carlos Ballestero, Javi Cuerda, Jorge Bravo and Francisco J García-Vidal from the only "Madrid team" I can be a fan of; Ilya Radko, Cameron Smith and Sergey Bozhevolnyi from Denmark (our source of great V-grooves); and Gozde Tutuncuoglu, Luca Francaviglia and Anna Fontcuberta I Morral from EPFL, whom I thank not only for the great collaboration but also the hospitality during a couple of measuring weeks.

The list is too long but I would also thank people from the other groups at ICFO with whom I interacted and made good friendships, from the members of ICONS to those joining the different spare time activities like the fútbol and futbolin groups.

A special mention does go to the people whom I establish friendships that go beyond life at ICFO, thank you Michael, Michelle, Jan, Camila, Jon, Nilli, Domi, Iris, Gabi, Nico and Gustavo for the good times together.

Thanks to my friends and family in Costa Rica for their unconditional support, in particular to my parents, Leda and Victor, thank you for all the support you´ve always gave me, especially all these years I´ve spent abroad. Finally Dani, thank you for being by my side supporting and encouraging me every single day.

Abstract

The field of photonics comprehends the generation, manipulation and detection of light (photons). Over the past decades, it has underpinned many of the technological advances upon which we rely on a daily basis, from our personal electronic devices and data communication channels (fibre optics), to medical instruments and lighting technologies. In line with this dependence, the photonics community is constantly seeking to develop novel technologies that can enable ever faster and powerful data communications, as well as compact and ultrasensitive monitoring systems. Advances made in this field depend greatly on the understanding and control we have over the light-matter interactions at play, with a strong focus on integrated photonic chip platforms due to their small footprint and scalability potential.

One of the main challenges to achieve fully integrated photonic chips deals with the emission coupling from nanoscale light sources to the on-chip photonic components. Ideally, the energy of a given light emitter should efficiently couple to sub-wavelength confined modes in order to fulfil scalability requirements. One solution is to implement metallic structures supporting surface plasmon polariton modes (i.e., coupled oscillations between photons and the free-electrons of the metal), which enable confinements beyond the diffraction limit of light.

This thesis deals with the development of hybrid photonic devices that enable the coupling of nanoscale light sources with on-chip plasmonic structures. These hybrid systems allowed us to influence the emission dynamics of the light sources, as well as transferring the emitted energy across the surface of a chip via subwavelength confined propagating modes. We implement state-of-the-art nanopositioning techniques to demonstrate various functioning hybrid devices operating with down to a single nanoscale emitter.

We start by exploiting a double high-resolution lithography approach combined with chemical functionalization, to assemble colloidal semiconductor quantum dots (QDs) at the hotspot of plasmonic nanoantennas. The antennas, designed to resonate with the excitation wavelength of our experiment, allow us to study the excitation enhancement provided by the metallic nanostructures by means of fluorescence lifetime measurements. New insights about the limitations of the implemented positioning method are also provided.

Next, we turn our attention to explore the potential of a particular type of plasmonic waveguide, namely the V-groove (VG) channel plasmon waveguides, to couple and transfer the emission from various nanoscale light sources across the surface of a chip. The initial experiments explore the coupling of quantum emitters (i.e., particles able to emit single photons) to the supported waveguide modes, with a focus on Nitrogen Vacancy (NV) centres in nanodiamonds and self-assembled QDs in semiconductor nanowires. In both cases, an

atomic force microscope (AFM) based nanopositioning technique was employed to bring the particles into the VG channels. We demonstrate for the first time in the field, the coupling of these type of quantum emitters to the channel plasmon polariton (CPP) modes supported by the VG waveguides, even down to the single emitter-VG coupling scenarios.

Finally, plasmonic waveguide-integrated nanowire laser devices are demonstrated. To achieve this, the AFM nanopositioning technique allow assembling core-shell-cap semiconductor nanowires into wafer-scale compatible VG waveguides. Room temperature operation of this hybrid plasmon nanolaser is realized, with a remarkable performance in terms of the transfer of energy from the hybrid plasmonic-photonic mode to the subwavelength confined propagating CPP mode supported by the VG.

The results presented in this thesis contribute to the list of potential hybrid photonic-plasmonic platforms applicable in future integrated photonic chip technologies. In particular, our devices based on the VG plasmonic waveguides, pave the way for the further development of more complex heterogeneous photonic circuitry.

Resumen

El campo de la fotónica comprende la generación, manipulación y detección de la luz (fotones). Durante las últimas décadas, la fotónica ha sido la base de muchos de los avances tecnológicos de los que dependemos diariamente, desde nuestros dispositivos electrónicos personales y canales de comunicación de datos (fibra óptica), hasta los instrumentos médicos y las tecnologías de iluminación. En línea con esta dependencia, la comunidad fotónica continuamente dedica esfuerzos para desarrollar nuevas tecnologías que permitan una comunicación de datos cada vez más rápida y potente, así como sistemas de monitoreo compactos y ultrasensibles.

Los avances en este campo dependen en gran medida de la comprensión y control que tenemos sobre las interacciones de luz-materia que está en juego, con un fuerte enfoque en los circuitos integrados fotónicos por su tamaño y escalabilidad. Idealmente, se quiere acoplar la energía de nano-emisores de luz a los modos confinados en dimensiones por debajo de la longitud de onda de operación. Una solución consiste en implementar estructuras metálicas que soportan modos de polaritón de plasmón de superficie (oscilaciones acopladas entre los fotones y los electrones de conducción de un metal), los cuales permiten confinamientos más allá del límite de difracción de la luz.

Esta tesis aborda el desarrollo de dispositivos fotónicos híbridos que permiten el acoplamiento de nano-fuentes de luz con estructuras plasmónicas en un substrato (chip). Estos sistemas híbridos nos permiten influir en las dinámicas de emisión de las partículas, así como transferir la energía emitida por medio de modos de propagación confinados. Para esto, hemos implementado técnicas de nano-posicionamiento de última generación para demostrar varios dispositivos híbridos que operan incluso con un único emisor nanoscópico.

Comenzamos implementando un doble método de alta resolución de litografía combinado con la funcionalización química de superficies, para ensamblar puntos cuánticos semiconductores coloidales en las áreas de interacción aumentada de nano-antenas plasmónicas. Las antenas, diseñadas para resonar con la longitud de onda de excitación de nuestro experimento, nos permiten estudiar el incremento de excitación proporcionado por las nanoestructuras metálicas mediante mediciones del tiempo de vida de la fluorescencia. También aportamos nuevas perspectivas en cuanto a las limitaciones del método de posicionamiento usado.

Luego, enfocamos nuestra atención en explorar el potencial de las guías de onda plasmónicas en forma de canales en V [*V-grooves* (VG) por su notación en inglés], para acoplar y guiar la emisión de diferentes nano-fuentes de luz a través de la superficie de un chip. En primer lugar, exploramos el acoplamiento de emisores cuánticos (es decir, partículas capaces de emitir fotones individuales), en particular de los centros de vacancia

de nitrógeno (NV) en nano-diamantes y puntos cuánticos auto-ensamblados en nano-cables semiconductores. En ambos casos, utilizamos una técnica de nano-posicionamiento basada en un microscopio de fuerza atómica (AFM por sus siglas en inglés) para posicionar las partículas dentro de las VG. En este trabajo, demostramos por primera vez en este campo, el acoplamiento de este tipo de emisores cuánticos a los modos plasmónicos soportados por las guías de onda VG, incluso hasta el escenario de acoplamiento con un emisor individual.

Finalmente, emprendemos la realización de dispositivos de nano-láser basados en nano-cables semiconductores integrados con las guías de onda plasmónica VGs. De nuevo, implementamos la técnica de nano-posicionamiento de AFM para ensamblar nano-cables de semiconductores dentro de las guías de onda VG. Demostramos el funcionamiento a temperatura ambiente de este nanolaser híbrido de plasmones, con un rendimiento notable en términos de la transferencia de energía desde el modo híbrido fotónico-plasmónico al modo propagativo de las VG.

Los resultados presentados en esta tesis contribuyen a la lista de plataformas híbridas fotónicas-plásmonicas aplicables en futuras tecnologías de chips fotónicos integrados. En particular, nuestros dispositivos basados en las guías de ondas plasmónicas VG, que son los primeros de este tipo en este campo, allanan el camino para el desarrollo de circuitos fotónicos heterogéneos más complejos.

Contents

Chapter 1 Introduction

Flashback 70 years in time and we find ourselves on the verge of one of the most influential inventions of our time, it was the year 1947 and the team integrated by William Shockley, John Bardeen and Walter Brattain at the Bell Laboratories in New Jersey were about to introduce the semiconductor transistor to our society. Shortly after a decade, Theodore H. Maiman demonstrated the first operational laser at the Hughes Research Laboratories in California, another keystone in modern technologies. Although these inventions started rather bulky in size, they soon progressed into compact platforms (i.e., integrated circuits and laser diodes), setting the stage for the optoelectronics era that revolutionized every aspect of modern technologies.

Fast-forward to our time, where we are witnessing the rapid advance of on-chip integrated electronic and photonic technologies, which are constantly shaping our daily lives. Conversely, our demand of ever faster and powerful communication and computation platforms, as well as the need for extremely accurate and ultrasensitive monitoring systems, whether in health, environment or security, are pushing fundamental research to explore novel technologies that can provide improved performances and functionalities while fulfilling miniaturization requirements.

Photonics relies on light-matter interactions to generate, manipulate and detect photons (i.e., light quanta) in a myriad of applications. One of the ongoing challenges in photonics research is the control of light emission from nanoscale light sources, both for free-space and on-chip applications, and it is the branch of nanophotonics in particular, the one providing the necessary tools to address this challenge, whether in terms of novel nanofabrication techniques or optical characterization methods.[1]

Over the last decades, there has been increasing efforts to develop solid-state nanoscale light sources such as single quantum emitters (QEs)[2,3] and small lasers,[4] as well as schemes of deterministic emission control,[5] which generally involves interfacing the emitters with other photonic components into so-called integrated photonic systems. This interfacing is fundamental to enhance and control the emission dynamics and improve the collection efficiencies into the available optical channels (either free-space, fibre optics or on-chip waveguides), in order to maximize the output rates from the emitters.

Many of the advances in the field have come from coupling these light emitters with dielectric photonic structures, including distributed Bragg reflectors, photonic crystal cavities, and optical fibres among others. However, the footprint of these systems is restrained by the diffraction limit of light, which corresponds to mode confinements of roughly half the operation wavelength. In this context, the sub-field of plasmonics, which deals with the study of light-matter interactions at metal-dielectric interfaces,[6] represents an interesting venue to provide novel insights and solutions to these efforts.

Surface plasmons have received wide interest in the photonics community due to their ability to provide strong confinements of energy and consequentially, enhanced light-matter interactions for media surrounding the metallic surfaces.[7,8] The latter for example, has allowed successful plasmon based commercial applications such as biomolecule sensing and surface enhanced Raman spectroscopy.[9] In addition, advances in on-chip nanostructuring of metals and nanopositioning techniques, have enabled the deterministic assembly of individual nanoscale light sources together with functional plasmonic structures.[10] These hybrid photonic-plasmonic devices operating with down to single emission sources have become of paramount importance in the rising field of quantum plasmonics,[11] as well as in classical integrated photonic circuits.

For example, in the field of quantum plasmonics, these hybrid systems can provide fundamental insights into strong light-matter interactions[12–14] and quantum many-body physics.[15–18] Furthermore, they are also envisioned to facilitate a variety of applications in quantum information technologies,[19] such as on-chip generation and routing of single photons,[20–23] single-photon transistors,[24] or plasmonic waveguide based quantum interferometers[25] among others.

On the other hand, for classical on-chip optical communication and sensing applications, the ideal platforms should integrate all key components within the same chip, including the light source, transmission lines, modulators and detectors. However, the current photonic chip technologies rely mainly on off-chip light sources.[26]

The common hybrid photonic-plasmonic device platforms currently pursued are the integration of plasmonic nanoantennas and two-dimensional plasmonic waveguides. The former aims at enhancing the excitation and emission dynamics of the emitters as well as controlling the directionality of their emission[27], while the latter can couple and route the emission via subwavelength modes across the surface of a chip.[28]

Initial efforts in the field were limited at first to randomly positioned and coupled systems.[20,29] Nevertheless, these works established the foundations and triggered future investigations by demonstrating the quantum nature of the coupled plasmons, which together with exciting theoretical proposals, [15,12,30] ignited the drive towards deterministically coupled hybrid photonic-plasmonic systems using nanoscale light sources.[10]

In general, these hybrid systems exploit the strongly localized electromagnetic modes of the plasmonic structures, and in turn, achieving efficient coupling relies on the accurate positioning between the emitters and the plasmonic structures, given the competition between the different available decay channels (radiative and non-radiative).

High precision lithography, scanning probe techniques and dynamic trapping approaches have become key enabling technologies for the assembly of such hybrid devices. These have facilitated various demonstrations of individual nanoscale light source coupling to plasmonic architectures, many of which were developed during the course of this thesis.

Further progress to reproducibly achieve efficient coupling from a nanoscale light source to a plasmonic circuit will allow researchers to combine these platforms with other novel plasmonic components, such as plasmonic modulators[31–33] and surface plasmon detectors,[34,35] so that hopefully one day, we can witness a fully integrated photonic-plasmonic circuitry operating with single on-chip nanoscale light sources.

This thesis explores the integration of various nanoscale light sources with two plasmonic systems in particular, namely gold nanoantennas and V-groove (VG) plasmonic waveguides, by exploiting deterministic positioning techniques to assemble the hybrid systems. Confocal and wide-field fluorescence microscopy techniques enabled us to study the emission dynamics and to reveal the emission coupling in the assembled devices.

The results presented in this thesis contribute to the list of potential hybrid photonic-plasmonic platforms applicable in future integrated photonic chip technologies. Our devices based on the VG plasmonic waveguides, which are a first of their kind, pave the way for the further development of more complex heterogeneous photonic circuitry.

The outline of the chapters hereafter is the following:

In **Chapter 2**, the relevant solid-state QEs and plasmonic structures covered in this thesis are introduced. Particularly, we focus on semiconductor quantum dots (QDs), both colloidal and self-assembled, defect centres in diamond, and semiconductor nanowire (NW) lasers. The sub-field of plasmonics will be introduced with an emphasis on plasmonic nanoantennas and two-dimensional waveguides. The chapter also covers the positioning methods that enable the study of such coupled systems.

In **Chapter 3**, the excitation enhancement of colloidal semiconductor QDs provided by single disc and dimer gap nanoantennas is studied. Plasmonic antennas excited at resonance create enhanced local electromagnetic fields, which are probed by implementing a positioning protocol based on a two-step electron beam lithography process combined with chemistry based self-assembly protocol. We studied the excitation dynamics of the coupled systems by means of confocal microscopy and lifetime measurements, which allowed us to extract the excitation enhancement independently of the luminescent enhancement.

Chapter 4 presents the first realization in the field of the coupling of individual QEs to VG plasmonic waveguides. To do so, we turned our attention to Nitrogen Vacancy (NV) centres in nanodiamond particles, one of the most prominent and extensively studied quantum emitters in current research. The surrounding diamond matrix embedding these promising defect centres allowed us to access the spatially confined channel plasmon modes supported by the VG channels, which offer large coupling efficiencies even at relatively large distances away from the metallic surfaces. By combining electron beam lithography with an electrostatic self-assembly approach, nanodiamond patterns were placed near the VG channels, and a subsequent scanning probe nanomanipulation step using an atomic force microscope, allowed us to position individual nanodiamonds containing a single emitter inside the channels. The emission coupling of the NV centres to the VG-supported propagating channel plasmon modes is revealed by means of wide-field fluorescence microscopy.

In **Chapter 5**, we work with recently developed self-assembled QDs embedded within semiconductor nanowire (NW) structures. Micro and nanopositioning techniques were combined to position individual NWs containing different densities of the self-assembled emitters into the bottom of wafer-scale compatible VG waveguides. The hybrid QD-NW VG devices were studied in a low-temperature cryostat by means of fluorescence microscopy. Coupling of the QD ensembles to the propagating channel plasmon modes is observed, even down to discriminating between single emitter coupling in the low emitter density NWs.

In **Chapter 6**, we investigate the integration of core-shell-cap GasAs/AlGaAs/GaAs NWs, which have lasing capabilities, together with wafer-scale compatible VG channel waveguides, to demonstrate a plasmonic-waveguide integrated NW laser platform. We exploit the good mode overlap between the hybrid nanowire-VG configuration and the sub-wavelength confined channel plasmon modes supported by the waveguides to enable lasing from a hybrid mode. By means of theory simulations and wide-field fluorescence microscopy, the efficient transfer of energy from the nanoscale laser to the confined propagating modes is revealed. Furthermore, enabled by our measuring approach we also observed direct proof of the surface plasmon generation from NW lasers on top of metallic films, a feature that so far had been elusive in previous works involving NW plasmon lasing.

Finally, in **Chapter 7,** we summarize the conclusions of this thesis and provide an outlook for future work in this field.

Chapter 2 Building blocks of hybrid photonic-plasmonic devices

Over the last couple of decades, photonic components and circuits based upon surface plasmon polaritons, that enable the concentration of light beyond the diffraction limit, have been proposed and extensively studied to enable the scalability and performance requirements of future communications, computation and sensing applications. In particular, the integration of plasmonic devices together with nanoscale light sources can become a key enabling technology in future integrated photonic systems. In this chapter, we introduce the building blocks utilized throughout this thesis for the development of novel hybrid photonic-plasmonic devices operating with precisely positioned nanoscale light sources. Specifically, this chapter describes the plasmonic structures, nanoscale light sources and positioning techniques that enable the hybrid devices presented thereafter.

2.1 Introduction

Hybrid systems combining nanoscale light sources and plasmonic structures are currently subject of increasing interest. These platforms can potentially provide integrated photonic circuits with subwavelength confined electromagnetic modes. Furthermore, in free-space and fibre optics applications, such systems can enable unprecedented control of the emission dynamics of the light sources, for example providing fast and efficient photon streams for data communication technologies. Over the past decade, different groups have demonstrated on-chip coupling of single nanoscale light sources with plasmonic architectures.[20,29,36–42] The most relevant material platforms to this thesis include semiconductor quantum dots and nitrogen vacancy centres coupled to metallic nanowires and nanoantennas, and semiconducting nanowire emitters coupled to metallic films and waveguides. It is worth mentioning that other platforms are being explored in the field (e.g., with single molecules and rare earth emitters),[3] however, we do not intend to cover them here.

In general, regardless of the emitter of choice, one of the main challenges in the field has been to efficiently couple the nanoscale light sources to the localized plasmon modes. The latter relies greatly in the ability to deterministically position the emitters within the regions of enhanced local density of states provided by the plasmonic elements. To achieve this, researchers have transitioned from early demonstrations that relied in randomly assembled devices, to the implementation of state-of-the-art nanopositioning techniques that allow assembling the individual emitters with the plasmonic structures.

In this chapter, we introduce the building blocks that enable the work presented throughout this thesis. First, a brief overview on the sub-field of plasmonics is provided, focusing on two-dimensional plasmonic waveguides and plasmonic nanoantennas. We then provide background on the nanoscale light sources considered in this thesis, including different types of semiconductor quantum dots, the nitrogen vacancy centre in diamond and semiconductor nanowire lasers. Finally, the state-of-the-art nanopositioning techniques utilized to assemble our hybrid devices are described.

2.2 Plasmonics

The notion behind the term ‘plasmon’ comes from the description of the optical properties of metals using the Drude-Sommerfeld model, also known as the *plasma model*, which considers a gas of free electrons (electrons in the conduction band of metals) moving over a fixed background of positive ions.[6] These electrons can oscillate in response to an applied electromagnetic field, with a dielectric function describing the free electron gas given by:

$$\varepsilon(\omega) = \varepsilon_{\infty} - \frac{\omega_p^2}{\omega^2 + i\gamma\omega} \quad (1.1)$$

where ε_∞ is a fitting parameter (usually $1 \leq \varepsilon_\infty \leq 10$), ω is the angular frequency of the electromagnetic field, γ is the collision frequency related to the damping of the electrons, and ω_p is the so called plasma frequency of the free electron gas. The quanta of these charge oscillations are referred as plasmons, in specific volume or bulk plasmons. In most metals, the plasma frequency is in the ultraviolet regime, and due to the longitudinal nature of the excitation, they do not couple to transverse electromagnetic waves (light). Instead, the plasma frequency of metals is typically determined via electron-loss spectroscopy experiments.[43]

The picture changes when considering either metal-dielectric interfaces or metal structures with nanoscale confinements, which support surface plasmon polaritons and localized surface plasmon polaritons respectively. The term polariton arises from the fact that these are coupled excitations between the surface charge oscillations and the electromagnetic waves, which is why, for conceptual reasons one often refers to the surface plasmons as photons trapped at a metal/dielectric interface. These two types of plasmons have distinct properties that are interesting for many novel applications. In this thesis, we explore two types of metallic structures that support such excitations to study their interaction with nanoscale light sources: plasmonic waveguides and metallic nanoantennas.

2.2.1 Surface plasmons polaritons

The coupling between electromagnetic fields and the oscillations of the free electron gas density at the interface between a metal and a dielectric, give rise to surface plasmon polaritons (SPPs). These bound surface waves can propagate along the surface plane and are evanescently confined into both the metal and the dielectric (Figure 2-1a). These SPPs are said to exhibit a transverse magnetic (TM) polarization, since the surface modes only exist for the electric field pointing in the z-axis. The dispersion relation describing the propagating SPP wave-vector k_{SPP} (Figure 2-1b) is given by:

$$k_{SPP} = k_0 \sqrt{\frac{\varepsilon_d \varepsilon_m}{\varepsilon_d + \varepsilon_m}} \tag{1. 2}$$

where $k_0 = \frac{\omega}{c} = \frac{2\pi}{\lambda}$ is the wave vector associated to the free-space light of wavelength λ, and ε_d and ε_m are the frequency-dependent permittivities of the dielectric and metal materials respectively. The condition for the SSPs to exist at a given interface is that the permittivities must have opposite signs, which is the case in noble metals at optical frequencies.[44]

Note that the dispersion relation implies an increase in momentum ($\hbar k$), which leads to a momentum mismatch between light and SPPs of the same frequency, meaning that for an ideal homogeneous interface, a free-space photon cannot excite a SPP. Nevertheless, it is possible to bridge the momentum mismatch and launch SPPs with free-space light using a

variety of techniques such as evanescent coupling using a prism (Otto and Kretschmann configurations),[45,46] grating coupling,[47] or near-field excitation. The latter approach can be achieved either by illuminating scattering particles,[48] using external near-field scanning probes,[49] or as explored in this thesis, by externally exciting nanoscale emitters that can transfer their energy to the propagative plasmon modes.

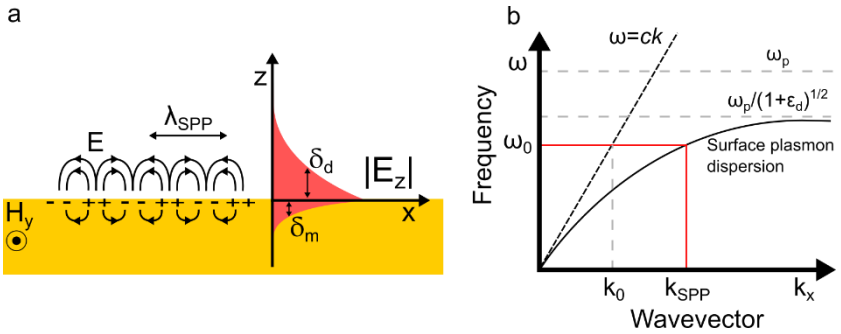

Figure 2-1. Surface plasmon polaritons. a) Schematic illustration of the surface charge oscillations supported at a metal-dielectric interface. b) Dispersion relation of the free-space photon (black dashed line) and the bound SPPs (black solid line). For a given frequency, there is a momentum mismatch between the SPP and free-space photon.

Once an SPP is launched, due to absorption into the metal, the SPPs are attenuated as they travel, with a propagation length constant given by the complex surface plasmon wave vector ($k_{SPP} = k'_{SPP} + ik''_{SPP}$) as follows:

$$L_{SPP} = \frac{1}{2k''_{SPP}} = \frac{c}{\omega}\left(\frac{\varepsilon'_m+\varepsilon_d}{\varepsilon'_m\varepsilon_d}\right)^{3/2}\frac{(\varepsilon'_m)^2}{\varepsilon''_m} \quad (1.3)$$

where ε'_m and ε''_m are the real and imaginary parts of the dielectric function of the metal.

Although SPPs on a metal film are confined within the vertical direction (out-of-plane), they can freely disperse within the plane, analogue to waves on a water surface. Clearly, this is not an efficient way to direct all the localized energy into a precise location on a sample surface, which calls for the need to further confine the field in a second dimension.

Two Dimensional Surface plasmon waveguides

The confinement of SPPs in two-dimensions (2D) is fundamental for constructing plasmonic circuitry,[50,51] and over the last decades a library of surface plasmon waveguides have been proposed and realized, each with its distinct SPP-type guided modes.[28] Some of the most common types of 2D plasmon waveguides are illustrated in Figure 2-2, including thin-film stripe waveguides (2D confinement of metal films), dielectric-loaded waveguides (dielectric films structures onto metal films), gap waveguides (dielectric gap in a planar film), cylindrical nanowire waveguides, wedge waveguides (triangular metallic protrusions) and channel waveguides (grooves inside in a metal film). In this thesis, we focused our work on a special type of V-shaped channel waveguides, more generally known as V-groove (VG) waveguides.

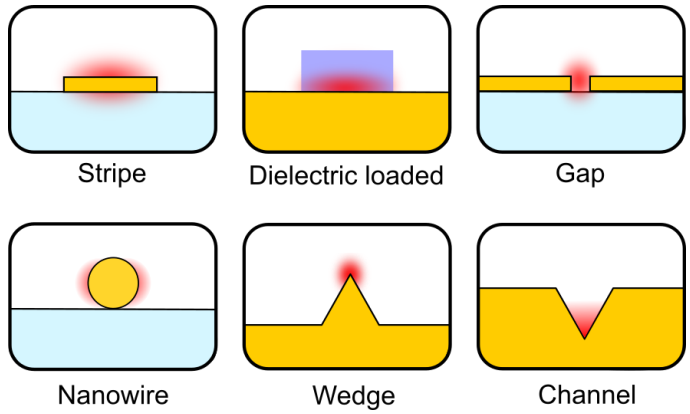

Figure 2-2 Common two-dimensional plasmonic waveguides. Top row: metallic stripe waveguides, dielectric loaded waveguides and gap waveguides. Bottom row: nanowire waveguides, wedge waveguides and channel waveguides. The red shaded areas represent the field localization of the associated supported modes.

V-GROOVE PLASMONIC WAVEGUIDES

The VG plasmon waveguides fall into the category of metal-insulator-metal configurations, where typically two metal surfaces are separated by a small (sub-micron) dielectric gap.[52] When the gap is sufficiently small, the SPPs associated with the two metal surfaces may interact and lead to hybridized modes typically referred as gap surface plasmons.[53] In the case of the VGs, two angled metal surfaces are configured to form a V-shaped channel. The VGs can support gap plasmons traveling in the vertical direction (normal to the sample surface) or modes that can propagate along the VG axis.

The particular case of propagating surface plasmons in tapered metallic grooves are the so-called channel plasmon polaritons (CPPs). Figure 2-3a shows a typical CPP mode simulated via the finite-element method for a gold VG in air at a wavelength of 1550 nm,[54] where the first two panels show the electric field components in the *x* and *z*-axis respectively, and the third panel shows the magnitude of the normalized electric field component $|E|$. The CPP mode is confined towards the bottom of the groove. The black arrows represent the electric field lines in the *xy*-plane, demonstrating that the CPPs are transverse electric (TE) polarized with respect to the sample plane. Typically, the field confinement increases and the propagation length decreases with decreasing opening angle of the VG, however other parameters such as the bottom apex geometry and the permittivity of the material inside the groove, also determine the performance of the waveguides.

In terms of fabricating such structures, the two most exploited methods include the implementation of a focused ion beam (FIB) to mill triangular shaped channels into a metallic layer,[55] and exploiting the anisotropic etching of silicon wafer to generate V-shaped channels.[56] The latter has proven to be very versatile as it supports different processes after

the etching step, for example directly depositing a metal, structuring gratings into the channel, or oxidizing the silicon planes prior to the metal deposition.

These VGs offer different potential applications depending on whether the channel or the gap plasmons are exploited. Some of these include their use in nanophotonic circuitry, where for example resonators,[55] interferometers, adiabatic focusing[57] and resonant networks[58] have been demonstrated with the use of the CPPs. On the other hand, demonstrations of enhanced extraordinary optical transmission[59] and resonant absorption[60] rely more on the gap plasmons that can propagate vertically through the V-profile. Furthermore, theoretical works predict that these structures provide an interesting platform to realize entanglement between individual quantum emitters placed along the same VG.[15,30] Figure 2-3b-d presents some examples of fabricated VGs together with some implementations in plasmonic circuit configurations.[55,58] For more details on these and other aspects of the VGs, the reader can refer to a well detailed review.[54]

Prior to this thesis, these VGs had only been studied by coupling light from external sources. In our case, we explore the implementation of VGs to efficiently couple the emission from single quantum emitters (Chapters 4 & 5), and from semiconductor nanowire lasers (Chapter 6).

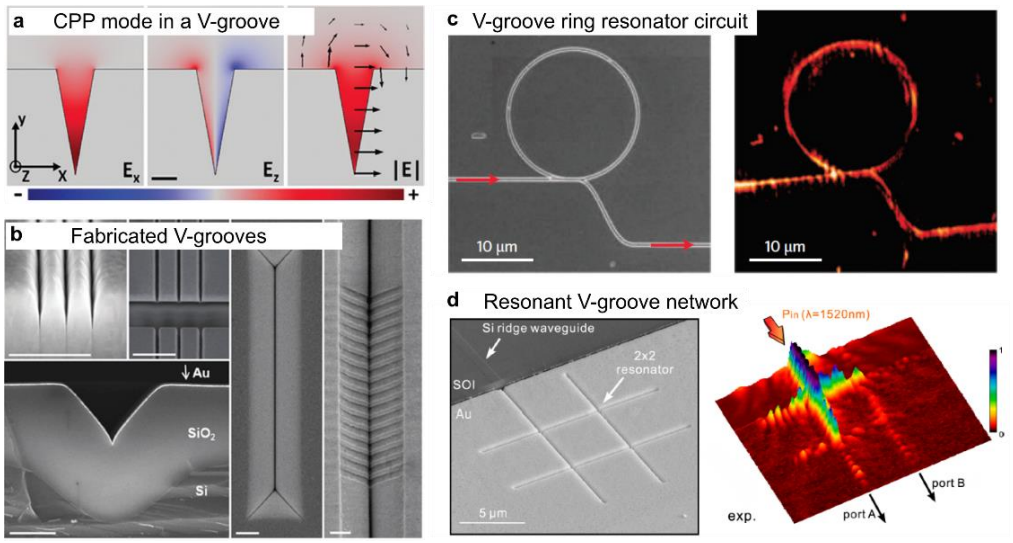

Figure 2-3. V-groove waveguides. a) Simulations of the supported CPP mode by a metallic VG structure in air at λ= 1.55 µm. (From ref. [54]). b) Scanning electron microscope (SEM) images of some fabricated VGs by means of focused ion beam and Si etching techniques (From [54] and references therein). c-d) SEM and near-field images of a VG ring resonator circuit and a resonant VG network (From refs. 55 and 58 respectively).

2.2.2 Localized surface plasmon polaritons

In contrast to SPPs, localized surface plasmons (LSPs) are non-propagating excitations of the free electrons of metallic nanostructures, coupled to the electromagnetic (EM) field of photons. A restoring force acting on the confined oscillating conductive electrons gives rise to a resonance condition, with EM fields amplified both inside and in the near-field of the particle, known as a localized plasmon resonance. In noble metal nanoparticles (e.g., from gold and silver), this resonance lies within the visible region of the electromagnetic spectrum and leads to an enhancement in the scattering and absorption properties of the particles. Furthermore, the resonance depends on the particle dimensions and refractive index of the local environment, making it attractive for sensing applications, as any change in the near-field of the particle will lead to a shift in the resonance wavelength.[61]

PLASMONIC NANOANTENNAS

An important feature of metal nanoparticles supporting LSPs is their ability to couple to free-space radiation, in other words, they can convert freely propagating optical photons (i.e., far field) into localized energy (i.e., near field), and vice versa. The resemblance to the function of microwave and radiowave antennas led to coining such nanoparticles as optical or plasmonic (nano)-antennas, and have been subject to extensive research over the last decades.[27] Progress in the research of nanoantennas has been greatly enabled greatly by the advances and widespread availability of high-resolution nanofabrication and characterization techniques, as well as commercial simulation software that help design and understand the properties of these structures.

Plasmonic nanoantennas are generally metallic structures with nanoscale features that can be fabricated into a variety of shapes and materials (typically gold, silver or aluminium), depending on the desired functionality and working wavelength range. Some of the most common configurations studied in the field are schematically represented in Figure 2-4, which shows single element antennas, dimer (gap) elements, multiple elements for directional functionality, hole antennas following the Babinet principle, and concentric grating based elements such as the bull's eye antennas. These configurations represent cavities for optical photons operating at a broad resonance wavelength when compared to photonic cavities, due to the losses associated with the involved metals.

The nanoantennas are designed to provide a region of intense EM field localization, also known as hotspots, where the light-matter interactions are enhanced. The EM field enhancement is associated with an increase in the local density of states felt by an emitter, which allows tailoring the emission dynamics (i.e., excitation and emission rates as well as directionality of the emission) by the presence of the nanoantenna. The latter becomes highly relevant for example if one wants to couple light to/from a quantum emitter in applications such as quantum communications and computation, where efficient and maximal photon extraction is desired.

In Chapter 3, we investigate the emission dynamics of semiconductor colloidal quantum dots placed in the hotspot of disc and disc dimer gap gold antennas.

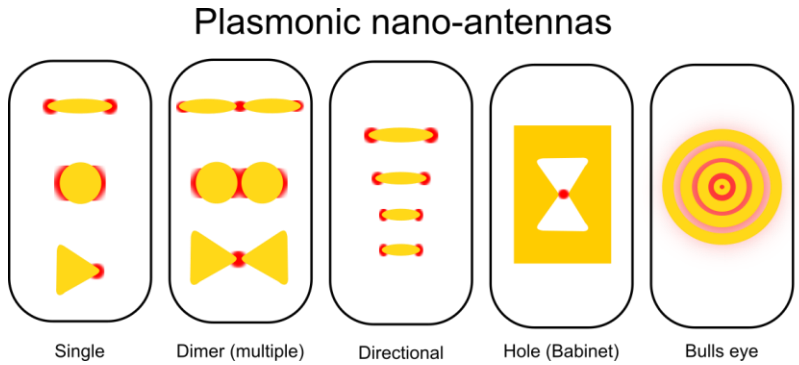

Figure 2-4. Common plasmonic nanoantennas geometries studied in the field. From left to right: single antenna elements, dimer gap antennas, directional antennas, hole antennas following the Babinet principle, and concentric gratings also known as bull´s eye antennas.

2.3 Nanoscale light sources

Currently, there is a myriad of nanoscale light sources available for the emission coupling to on-chip photonic or plasmonic structures, all with their distinct properties and operation wavelengths that become relevant depending on the desired application. The list includes single atoms and ions, single molecules, defect centres in diamond, and different types of semiconductor based emitters such as light emitting diodes and lasers. Some of these emitters are interesting for quantum information applications due to their ability to emit single photons or entangled photon pairs. These are typically referred as quantum emitters due to their non-Poissonian emission characteristics.[62] On the other hand, small lasers (nanolasers) also have a lot of potential in integrated photonic platforms due to their intense and coherent emission despite their small footprint.[4]

In this section, we only intend to introduce the emitters relevant to this thesis, namely the semiconductor quantum dots, both colloidal and self-assembled, nitrogen defect centres in diamond, and semiconductor nanowire lasers.

2.3.1 Semiconductor quantum dots

Semiconductor materials are characterized for exhibiting a band-gap in their energy spectrum. The spatial confinement of the motion of electrons, holes or excitons (electron-hole pair excitations) in such materials leads to a discretized energy spectrum in what are known as semiconductor quantum dots (QDs).[63] These QDs are often referred to as 'artificial atoms' because their emission process is a result of discrete, atomic-like energy levels. Unlike atoms and molecules that can only emit a single photon upon relaxation from

the excited state, QDs can support multiple excitons. Consequently, if two electron-hole pairs (bi-exciton) can radiatively recombine, the simultaneous emission of two photons from a QD is then possible. The quantum confinement in semiconductor QDs can be due to electrostatic potentials (e.g., in two-dimensional electron gases), or it can arise from the physical confinement of a semiconductor material, as is the case of small semiconductor nanoparticles (colloidal QDs) and small islands of material embedded within a solid matrix (self-assembled QDs).

COLLOIDAL QUANTUM DOTS

Colloidal QDs are semiconductor nanocrystals that exhibit absorption and emission properties that, for a given composition, are tuneable according to their size due to the quantum confinement of its charge carriers. These nanocrystals where initially introduced back in the early 1980´s, and over the last three decades there has been tremendous progress in their synthesis, characterization and implementation in fundamental research as well as technological applications.[64,65] In general, these nanocrystals can be synthesized from a variety of II-VI, III-V and IV-VI materials from the periodic table, which depending on the composition but also on the design (i.e., core-shell or core-shell-cap configurations) can span the full visible and near-infrared regions of the spectrum. Figure 2-5a presents some examples of QD solutions of varying size and composition exhibiting photoluminescence (PL) under ultraviolet excitation, while Figure 2-5b shows the PL spectra of QDs with a core-shell design as shown in the inset schematic.[63]

One feature of colloidal QDs is their blinking dynamics (i.e., switching between on-off states), which is attributed to an Auger ionization process initiated by the creation of multiple excitons in the QD. The energy released from the recombination of one electron-hole (e-h) pair may be transferred to another e-h pair, causing an electron (hole) to be ejected to the surface and putting the QD in a ionized state, which is often referred to as a trap or dark state due to its lower quantum yield compared to the neutral state. These blinking dynamics represent a drawback if QDs are to be implemented as a single photon sources on demand, and many efforts are put into improving the stability of their emission dynamics.[66]

Colloidal QDs can be exploited either for their photoluminescence properties, for example in light emitting displays or as fluorescent bio-markers in microscopy, while their ability to generate carriers upon light absorption makes them suitable for novel photodetection applications.

In this thesis, we focus on the possibility of using QDs as individual quantum emitters to explore their interaction with metallic nanoantennas, and study how these plasmonic structures can enhance their excitation and emission dynamics. Specifically CdSe based QDs are utilized, which have shown good single photon emission characteristics at room temperature operation.[67]

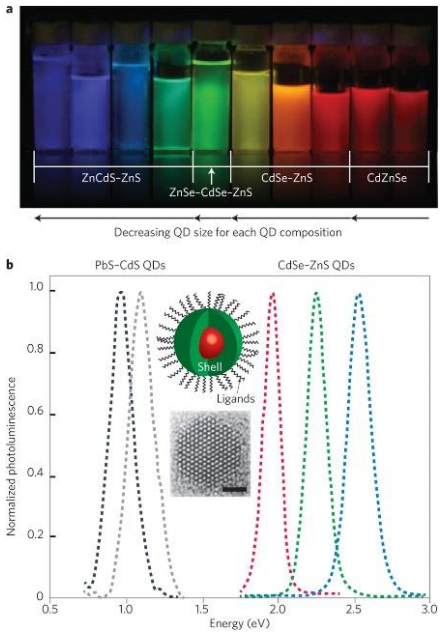

Figure 2-5. Colloidal quantum dots. a) Solutions of QDs of different compositions and sizes showing visible photoluminescence upon excitation with ultraviolet light. b) Emission spectra of QDs spanning the visible and near-infrared regions. The insets show a common core-shell configuration with surface ligands (top) and a transmission electron microscope image of a colloidal QD (bottom). Images adapted from ref 63.

SEMICONDUCTOR QUANTUM DOTS IN NANOWIRES

Nanoscale islands of semiconductor materials, also known as self-assembled QDs, represent an excellent platform for modern photonic applications, such as single-photon sources in quantum communication systems.[68] The most popular type of self-assembled QDs are those grown with the Stranski-Krastanov method, which exploits the strain relaxation in lattice mismatched epitaxial layers to form nanoscale islands, providing quantum confinement of charge carriers.[69] Alternatively, confined portions of semiconductor materials can also be obtained in epitaxially grown filamentary structures, also known as semiconductor nanowires (NWs).

These NWs can embed either multiple or single QDs within a single structure. Figure 2-6 shows some examples of state of the art QD-NW structures. Depending on the growth conditions, the QDs can assemble either at the centre of the NW axis[70–72] (Figure 2-6a) or near the outer edge of the NW apex[73,74] (Figure 2-6b).

The on-axis QDs have been more extensively studied, where single QD-NWs can be fabricated with high yield and bright single photon emission. In case of the off-axis QDs, the control over single QD growth is challenging due to the self-assembly nature of their growth. Nevertheless, it is possible to tune the QD density to obtain NWs with well separated individual QDs. These QDs have excellent optical properties, taking into account that they are just a few nm away from the surface (where usually SK QDs suffer from non-radiative

contributions). Individual QDs are found to be very bright (with count rates in the MHz range), emission linewidths are small (sub-100 μeV), and the photons are highly anti-bunched (2% multiphoton emission even with intense non-resonant excitation).[73,75]

In Chapter 4, we work with the recently developed off-axis type QD-NWs, and explore the coupling of these emitters to the propagating modes supported by VG plasmonic waveguides.

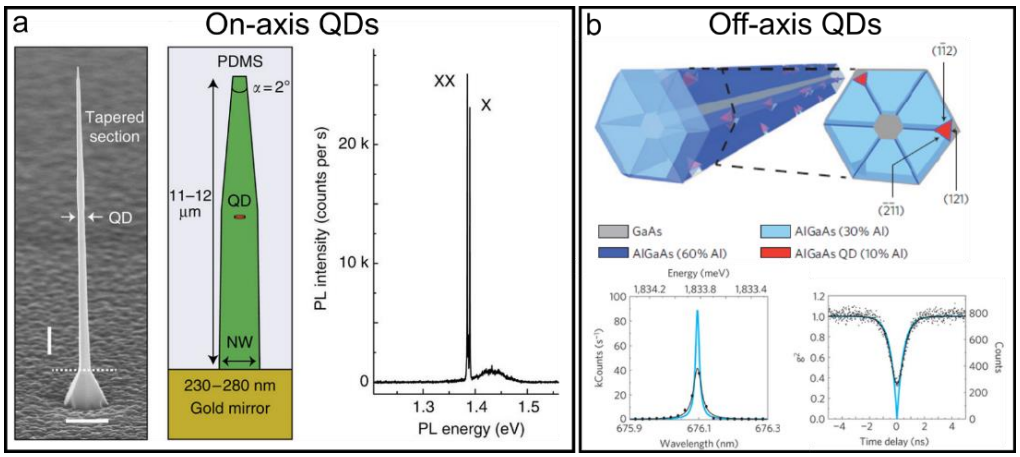

Figure 2-6. Semiconductor QDs in NWs. a) On-axis QDs can be fabricated with high precision on the number of QDs per NW structure. These can be transferred to a metallic mirror substrate to enhance the photon collection. The spectra shows the bright emission from the exciton and bi-exciton lines. b) Schematic of the off-axis QDs, they self-assemble as AlGaAs islands near the outer edge of the NW apex, and occur in a statistical fashion. For NWs with low QD density it is possible to identify individual QDs, which exhibit high brightness and good single photon emission (bottom). Images adapted from refs. 72,73 respectively.

2.3.2 Nitrogen vacancy centre in diamond

Defect centres in diamond, also known as colour centres due to their luminescent properties, arise from the absence or substitution of carbon atoms in the diamond lattice that leads to the creation of additional energy levels inside the diamond´s large band gap (E_g=5.5 eV). There are over 500 types of known defect centres in diamond, from which perhaps a handful have shown promising single photon emission properties.[76,77]

The NV centre in particular has gathered most of the attention, mainly due to its high brightness and stability as a single photon source, but also, due to the fact that the electrons from the NV centre exhibit a ground state spin-triplet (spin S=1), which can be addressed optically and manipulated with external electric and magnetic fields, making it promising for quantum computation and magnetometry sensing applications. Furthermore, it is the most common colour centre, it is commercially available both in high grade bulk diamond samples and in nanoparticle solutions (nanodiamonds), but can also be artificially implanted with very high precision.[77,78]

In the atomic structure of the NV centre in diamond (Figure 2-7a), two adjacent carbon atoms in the tetrahedral diamond lattice are substituted by a nitrogen atom and a vacant space, hence its name. This configuration forms a C_{3V} symmetry, where the electrons orbit around the vacancy and the four adjacent atoms. The NV centre can exist in two charged states, known as the NV^0 and NV^- states. The latter is referred simply as the NV centre since its spin properties make it more attractive for many applications.

Figure 2-7b shows a simplified electronic level structure for the NV^- state, which for the purposes of this thesis can be seen as a three-level system with a triplet ground state ($^3A_2$), a triplet excited state (^3E) and a metastable state (^1A). Excitation from the ground state to the excited state is typically carried out with green lasers (532 nm). The system can then relax by a broadband photon emission with a zero-phonon line (ZPL) at 637 nm, or through a secondary path involving a non-radiative relaxation via the singlet metastable state.

The emission spectrum of a nanodiamond containing multiple NV centres (likely containing both charged states as seen from the ZPLs), is shown in Figure 2-7c. The time it takes the excited state to relax to the ground state (lifetime) varies on the structure (bulk or nanoparticle) as well as on the proximity and orientation of the defect centre with respect to the diamond surface. In bulk diamond samples, the lifetime is in the order of ~11 ns, while NVs in nanodiamonds typically exhibit longer lifetimes due to the reduction of the radiative emission rate induced by the decrease of the effective refractive index of the medium surrounding the NV centre.[76,79] Figure 2-7d shows the lifetime distribution for single NV centres in nanodiamonds (diameters in the range of 100 nm) deposited onto a glass substrate, from which a lifetime value of τ=24.2 ± 7.2 ns was extracted, in agreement with other reports in the literature working with similar sized diamonds.[80]

Furthermore, as seen in the electronic level structure, the triple ground state levels are separated by a 2.87 GHz transition that can be accessed via microwave radiation. When the NV centre is excited from the m_s=±1 ground state, there is a larger probability that the system will relax via the non-radiative metastable state, causing the luminescence of the NV centre to drop by roughly 20-30% when the applied microwaves are in resonance with the m_s=0 and m_s =±1 transition. This difference in brightness allows to optically read-out the spin state of the system, even at room temperature, which is one of the main reasons of why the NV centre has such a great potential in quantum optics applications. For more details on the electronic structure and other characteristic NV properties (e.g., splitting of the m_s =±1 states via magnetic fields) the reader can refer to reviews in the literature.[76]

In Chapter 3, nanodiamonds containing multiple and single NVs are employed to demonstrate the coupling of their emission to the propagating modes supported by V-groove plasmonic waveguides.

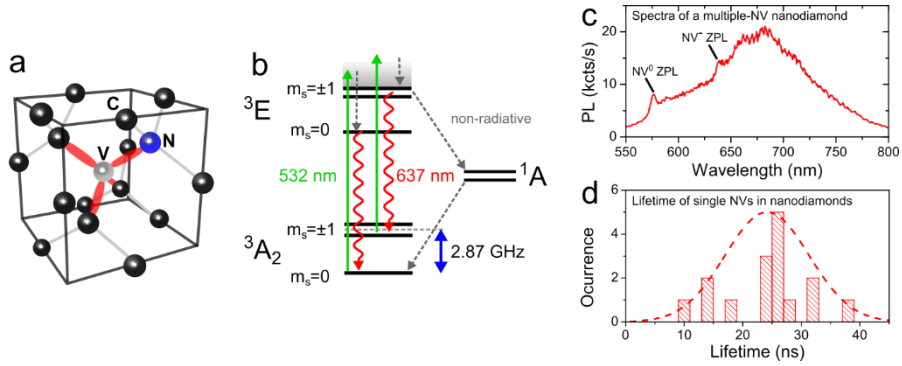

Figure 2-7. Nitrogen vacancy centre in diamond. a) NV centre atomic structure in a diamond carbon lattice. A nitrogen atom and a vacant site substitute two carbon atoms in the lattice. b) Simplified electronic level structure of the NV^- charge state. Populations in the ground state spin triplet can be switched with 2.85 GHz microwaves. With green laser excitation (532 nm), the ground state spin triplet ($^3A_2$) can be promoted into the excited state (^3E). The excited state can decay by emission of a photon. The ZPL of the NV^- state corresponds to a photon wavelength of 637 nm. c) Emission spectra of a nanodiamond with multiple NV centres, the ZPLs corresponding to the neutral and negatively charge states are identified. d) Nanodiamonds with single NVs deposited on a glass substrate show a lifetime distribution of τ=24.2 ± 7.2 ns, in agreement to other works in the literature.

2.3.3 Nanowire lasers

Filamentary semiconductor structures also known as nanowires (NWs) can undergo lasing emission under the right geometrical designs and content of gain medium material. Interest in the application of semiconductor NWs as nanoscale laser sources dates back to 2001, where Huang *et al* reported intense and narrow emission peaks from ZnO nanowires upon optical excitation, attributing their observations to a lasing action in the NWs.[81] However, this conclusion remained debatable, as the presented Power in-Power out (P_{in}-P_{out}) data of the emission peaks was not analysed with enough detail to prove the transition from amplified spontaneous emission (ASE) to a linear regime, characteristic of true laser oscillation. Despite the shortcoming, the publication sparked strong interest into the potential of NWs as nanolaser sources, and several groups reported similar behaviours from the ZnO structures as well as from other materials.[82]

Misconceptions of lasing evidence are not rare, especially in emerging novel nanolaser systems. It is critical to analyse in detail the behaviour of a system to rule out other possible scenarios.[83] Two reports in 2006 and 2008 provided stronger evidence of the lasing action in the NW structures. First, Van Vugt *et al* reported the presence of interference fringes in the collected fluorescence images, which coincided with the onset of strong and narrow emission peaks.[84] The fringes evidenced the coherent character of the emission from such a lasing cavity. However, the authors did not show details on the P_{in}-P_{out} characteristics of the emission, thus limiting the details of the transition through the different regimes. The conclusive evidence of the transition from the ASE into the lasing regime was reported in 2008 by Zimmer *et al*.[85] They presented clear evidence of the transition from two linear regimes (spontaneous and lasing emission respectively) via a superlinear regime (ASE).

Their work marked the benchmark on how to evaluate and properly present the data of such systems, in order to eliminate ambiguity as to whether a system only enters the ASE regime, which is also characterized by a linewidth reduction and a sudden increase in emission (a kink in a linear scale plot of the intensity vs pump), and thus can often lead to misinterpretations.

Over the past decade, there has been increasing interest in the development of NW lasers, with different material platforms covering a broad portion of the electromagnetic spectrum. The reader can refer to recent review articles for details on the different NW laser platforms.[86,87]

In particular, NWs based on GaAs have received increasing interest, supported by its role in current commercial on-chip technologies.[88] The first GaAs based NW lasers were introduced during the course of this thesis, in 2013 by Saxena *et al*[89] and Mayer *et al.*[90]

In the years after, great progress has been made with this material platform, where both pulsed and continuous-wave operation have been demonstrated.[89–96] Lasing action has been realized not only from photonic modes in horizontal[89,90] and vertical cavities,[92] but also from hybrid plasmonic modes in NWs assembled onto metallic substrates[95,96] Furthermore, quantum confined active regions such as self-assembled quantum dots[97] and quantum wells[94] have been introduced to improve the performance of the NW lasers.

In general, most works on NW lasers have focused on the fundamental characterization of these systems, and where the lasing emission has been collected from the free-space scattering at the NW extremities, without major studies as to whether the lasing emission can be exploited for on-chip routing.

In Chapter 6, we address this gap in the field and realize a plasmonic waveguide integrated nanowire laser platform, demonstrating the efficient energy transfer of a NW lasing mode to the propagating subwavelength mode supported by V-groove plasmonic waveguides.

2.4 Nanopositioning techniques

Fully exploiting the capability of coupling nanoscale light sources with on-chip plasmonic structures requires high accuracy control of the relative position between the emitters and the electromagnetic modes supported by the plasmonic architectures. The ability to position a nanoscale light source at an optimum position within the landscape of the local density of states (LDOS) supported by a plasmonic structure is at the moment one of the challenging aspects in current nanophotonics research. Such assembly can enable precise control of the emission dynamics of the light sources (i.e., excitation and emission rate enhancements), tuned directivity in free-space, on-chip waveguiding and quantum bit

entanglement among others, making this task highly relevant for studying such integrated hybrid systems.

Over the years, a diverse toolbox for the deterministic position control of nanoscale objects has become available; including the use of high precision electron beam lithography, surface functionalization directed assembly, scanning probe manipulation and particle trapping techniques.[98,39] These techniques have allowed researchers to reach unprecedented control in the coupling between nanoscale light sources and on-chip photonic and plasmonic structures. Here we briefly introduce the basic concepts behind the positioning techniques exploited in this thesis, while specific details on each particular device assembly are mentioned in the corresponding chapters.

LITHOGRAPHY BASED METHODS

High resolution and precision lithography tools are routinely used to pattern on-chip nanostructures. In general, these systems are also equipped with precision alignment software that allows overlying patterns in multiple step fabrication processes with sub-100 nm alignment precision. This can be exploited for example to pattern plasmonic nanostructures on top of nanoscale emitters previously identified by means of confocal microscopy imaging,[99,100] or to open small holes on top of previously fabricated structures that will serve as localization areas for the emitters.[101] The latter is particularly powerful when combined with surface functionalization protocols as described next.

SURFACE FUNCTIONALIZATION DIRECTED ASSEMBLY

It is possible to exploit the affinity of molecules to specific surfaces in order to functionalize nanostructures for the subsequent specific binding of nanoscale objects (typically also exhibiting certain surface functionalization). The functionalization of surfaces for directed assembly is a field on its own, so we do not intend to cover it in detail; the idea is just to provide the reader with a taste of the principle behind this positioning approach. A common example of directed assembly is the use of self-assembled monolayers (SAMs) that contain thiol groups with high affinity to gold surfaces. The SAM termination opposite to the gold surface can then be activated and modified to accept a variety of chemical species, which can be either other molecules, proteins or anti-bodies to name a few. The emitters to be assembled can in turn exhibit the complementary surface functionalization that will result in the specific binding between the two objects. This method is typically used to coat large areas of gold films for example in bio-sensing applications, however when combined with the high resolution and precision alignment of nanolithography techniques, a few (down to single emitters) can be positioned at the nanostructure of choice.[37]

SCANNING PROBE TECHNIQUES

The most common scanning probe technique relies on the use of an atomic force microscope (AFM) in order to move objects across the surface of a chip or to transfer them

from one substrate to the other.[102] The technique exploits the ability of an AFM system to perform movements both in tapping mode for imaging, and in contact mode to move the particles across a substrate.[102,103,38] In the early years, it required custom-made AFM systems in order to achieve such a dual operation, but nowadays, commercial nano-positioning add-on software is readily available.

An alternative to manipulate objects with nanometer precision is to use sharp probe tips mounted on piezoelectric stages inside a scanning electron microscope.[104] However, this technique has not been widely adopted, with one of the main reasons being that it has the drawback of being invasive to the structures of interest, given that the electron beam exposure can lead to charge effects and carbon residues.

Chapter 3 Colloidal quantum dots coupled to plasmonic antennas

The ability to integrate single quantum emitters with photonic structures allow investigating fundamental aspects of the emission dynamics of such coupled systems. Furthermore, it enables the on-chip realization of novel devices such as single photon sources and detectors. The combination of colloidal quantum dots and metallic nanoantennas represents an interesting platform to realize these novel technologies. Here, we implement a recently developed positioning method to investigate quantum dots assembled with monomer and dimer gap antennas resonant to the excitation wavelength. Detailed analysis of the multiply excited states quantifies the antenna´s influence on the excitation intensity and the luminescence quantum yield separately. We achieved up to a 15-fold enhancement for the dimer gap antenna case. Furthermore, we looked closer into the positioning yield, and discovered a limitation of the positioning approach. Specifically that surface residues after the electron beam exposure are responsible for the non-specific binding of the quantum dots at areas in the substrate other than the gold structures.

3.1 Colloidal quantum dot-plasmonic antenna devices

As introduced in Section 2.3.1, semiconductor nanocrystals, commonly known as colloidal quantum dots (QDs), are very attractive to implement as on-chip single photon sources due to their high brightness and low photo-bleaching properties when compared to fluorescent molecules. Variations of the material composition and particle size allow to broadly tune the emission energy for applications ranging from the visible to the near-infrared regions.[63] To exploit their potential as single photon sources, it is desirable to interface them with nanoscale photonic elements that allow modifying and controlling their emission properties. Resonant plasmonic nanoantennas are particularly promising for this task due to the strong field confinements available at the antenna hotspots,[27] where the QDs can experience enhanced light-matter interactions.

One of the major challenges associated with the integration of quantum emitters with on-chip photonic elements, is the ability to position the quantum emitter at an optimum location within the landscape of the local density of states (LDOS) supported by a given photonic structure. When we started this thesis research, most works relied on the random assembly of QDs onto metallic templates and structures,[105–107] or on the use of scanning probe techniques to mediate the interaction of the metallic structures with individual emitters,[108] similarly to the approaches used for single molecule studies.

Alternatively, the possibility of exploiting chemical binding through functionalized structures allowed to control the distance between the QDs and metallic structures.[109] In this context, in a collaboration between our research group (Prof. Romain Quidant) and the group of Prof. Niek van Hulst (also at ICFO), a double lithography method combining the high resolution and precision of electron beam lithography (EBL), with the chemical binding of functionalized QDs and Au surfaces, was introduced in 2010. The joint collaboration used this technique to demonstrate the unidirectional emission of a QD coupled to a Yagi-Uda antenna.[37] Shortly after, other demonstrations exploited this surface functionalization approach to study the coupling from QDs to other plasmonic structures, including coupling to multipolar antennas,[110] to propagating nanowire plasmons,[111] and gold nanocones,[112] among others.

In this chapter, we built-up from this work to assemble QD-antenna devices that allowed us to study the excitation enhancement experienced by QDs when coupled to resonant structures. We used an experimental approach that allows discriminating between the excitation enhancement and the photoluminescence (PL) quenching induced by the nanoantenna.[107] Excitation enhancements of up to 15-fold for the dimer gap antenna were achieved, however with a significant reduction in the quantum yield of the coupled system.[113] We also investigated the single emitter positioning reproducibility of this method, and discovered a limitation to that was not identified in previous works.

3.2 Materials and Methods

3.2.1 Colloidal quantum dots

As mentioned in Chapter 2, colloidal QDs can be synthesized from different materials and compositions, which determine the optical properties required for a given application. In our work, both custom-made and commercially available QDs were investigated.

The custom-made nanocrystals were synthesized by Stella Itzhakov in the group of Prof. Dan Oron at the Weizmann Institute of Science in Israel. These QDs consist of a core/shell/shell CdSe/CdS/ZnS design. The quantum dots had quasi-spherical shapes with ~10-15 nm diameters (Figure 3-1), and a peak emission at 660 nm with 30 nm full width at half maximum. The surface of the QDs were later functionalized by Dr. Mark Kreuzer in our group, to exhibit the carboxy-PEG terminations necessary for the attachment to the functionalized gold nanostructures. These custom synthesized QDs bear a high bi-exciton population and thus were suitable to study the excitation enhancement of the emitters provided by resonant gold nanoantennas.

The commercial QDs had a CdSeTe/ZnS configuration and were purchased from Invitrogen (Qdot 800 ITK). They exhibit a polymer coating and a functionalized surface, with a peak emission at ~790 nm. These QDs were implemented to investigate the single emitter-positioning efficacy of the double lithography method.

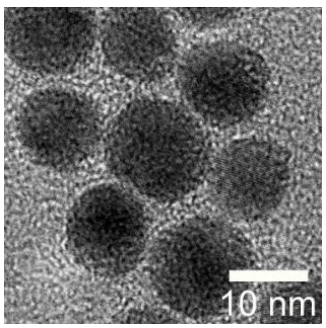

Figure 3-1. Custom-made colloidal quantum dots. Transmission electron microscope image of the core/shell/shell CdSe/CdS/ZnS QDs.

3.2.2 Metallic nanoantenna fabrication

The antenna fabrication scheme is illustrated in Figure 3-2a. Glass coverslips were used as substrates, which were capped with a 10 nm conducting indium tin oxide (ITO) layer deposited by electron beam evaporation. The coated substrates are then baked at 300 ºC during 5 min to obtain the conductive phase of the ITO, with a ~3 kΩ resistance (measured

over ~1 cm length with a two-point probe). The ITO layer prevents charging effects during the electron beam exposure.

For the first lithography step, a PMMA solution (Microchem 950k 4%, diluted 3:1 in tricholorobenzene) was spincoated at 8000 rpm during 1 min, and baked at 175°C for 5 min on a hot plate, yielding a 120 nm thick layer measured with a profilometer. The structures are defined in a EBL system (FEI InspectF50) with 30 keV acceleration voltage. We worked mainly with rod and disc antenna designs in single (monomer) or gap (dimer) configurations. Dense arrays were designed with particle spacing in the range of 500 nm (to yield a strong signal for the extinction spectra), and sparse arrays with 1.5 µm pitch to allow us addressing individual antennas in the confocal fluorescence scans. Alignment marks were also included within a 50 µm write-field, which are necessary for the positioning steps. The exposure dose was typically 450 µC/cm^2. The samples were then developed in a MIBK:IPA (1:3) mixture for 45 sec, followed by immersion in isopropanol (IPA) to stop the develop. The substrates were finally dried in a flow of nitrogen (N_2).

We then deposited a 40 nm gold film by thermal evaporation at a rate of 2 Å/s. Finally, lift-off was carried out in acetone heated at 55 ºC during 1 h, followed by rinsing in IPA before drying with N_2.

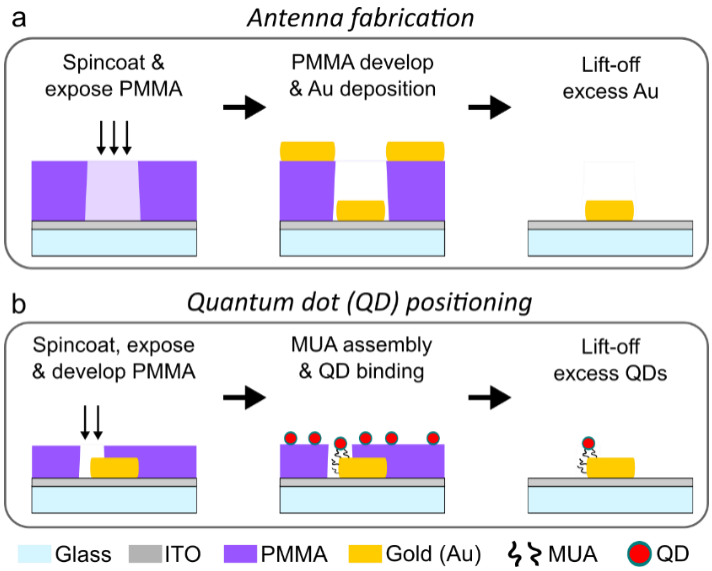

Figure 3-2. Fabrication schemes for the QD-antenna devices. a) Fabrication steps of gold nanoantennas by e-beam lithography (EBL) and metal deposition/lift-off approach. b) EBL and chemical functionalization based positioning of QDs onto the nanoantennas.

3.2.3 Quantum dot positioning protocol

In this chapter, we followed the fabrication method that was previously introduced to position QDs onto Yagi-Uda antennas.[37] The chemical functionalization protocols were developed by Dr. Mark Kreuzer in our research group. The positioning scheme (Figure 3-2b), combines a second EBL step with a surface chemistry protocol designed to promote the binding of the QDs to the Au surfaces. For this, we spin coat again a PMMA layer (~50 nm) on our antenna-patterned substrates, and use a second EBL exposure to define the areas where the QDs can assemble.

A fundamental aspect of this method is the accurate positioning of the emitters. This is made possible by using the alignment marks defined during the antenna fabrication step, which allows us to align small holes with our antennas within a few tens of nanometers. To confirm the accuracy of this method, test samples were fabricated where a 10 nm thick Ti film was evaporated onto the PMMA mask, followed by a lift-off process (instead of the chemical functionalization step).

Figure 3-3a shows SEM images of Au dimer antennas with a 50 nm wide Ti dot aligned to the centre of the gap. Here, we designed the gaps particularly large to allow the visualization of the Ti dot, which as it can be observed, exhibits very good alignment. This technique allows to position the emitters at specific locations even within a small antenna. In Figure 3-3b, we show SEM images of Ti dots displaced laterally in 15 nm steps (designed below the antenna axis for clarity).

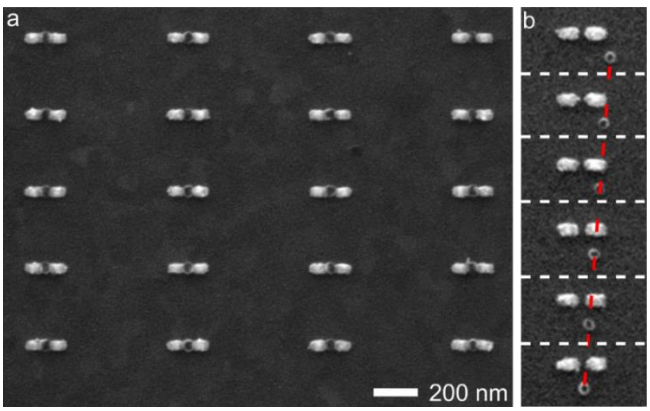

Figure 3-3. E-beam lithography based positioning. a) SEM images of an array of Au gap antennas with a 50 nm wide Ti disc aligned at the centre of the gap. b) SEM images of Ti dots displaced alongside a gap antenna in 15 nm steps.

When assembling the QDs, the exposed holes define the boundaries for the formation of a self-assembled monolayer (SAM) (Figure 3-2b). We immerse our substrates in a 10 mM solution of mercapto-undecanoic acid (MUA) in ethanol and leave incubating overnight at room temperature (RT). These molecules have one end with a thiol group (-SH) that offers

selective binding to the Au surface and on the opposite end, a carboxylic group (-COOH) that offers a free binding site for a complementary amine group. Both the custom-made and commercial QDs are functionalized with amine-polyethilene glycol (amine-PEG), which, after activation with Ethyl-3-(3-dimethylaminipropynol)-carbodiimide (EDC) and N-hydroxysuccinimide (NHS), can form a covalent bond to the carboxylic group of the MUA molecules. In the case of the home-made QDs, we added an incubation step of the MUA coated substrate with a 1% solution of bovine serum albumin (BSA) in phosphate buffer, 7.5 pH for 1 h at RT. The additional BSA protein layer was included to compensate for the lack of polymer coating as compared to the commercial QDs, in order to minimize non-radiative coupling between the QDs and the Au surfaces. Finally, the sample was immersed in acetone to lift-off the PMMA layer and excess QDs, leaving only those attached to our structures within the exposed areas.

3.2.4 Optical characterization

Extinction spectroscopy was implemented to characterize the plasmonic nanoantennas. Measuring the resonance wavelength of the fabricated structures allowed to select the relevant ones for the second lithography and binding steps. The final assembled QD-antennas devices were characterized by means of confocal photoluminescence microscopy imaging and emission lifetime measurements.

EXTINCTION SPECTROSCOPY

The optical setup consists of a standard microscope (Olympus BX41) in a bright field configuration. The illumination is performed from the bottom side of the sample with a 100 W halogen lamp, having a linear polarizer and a bright field condenser (0.1 NA) before the sample. The transmitted light was collected with a bright field objective (10x, 0.25 NA), and passed through a beam-splitter into a CCD camera for alignment and to a spectrometer (Andor SR300, Shamrock) via an optical fibre (200 μm diameter) for the spectral analysis of the transmission signal.

As described in Chapter 2, the antenna resonance can be tuned by varying the antenna dimensions. For example, by increasing the length (aspect ratio) of a rod antenna, a red-shift of the resonance wavelength is obtained. The coupling of two rods in a dimer gap antenna configuration also red-shifts the resonance, while for a fixed antenna arm length, the resonance red shifts with decreasing gap size. The extinction spectra (Figure 3-4) are shown for the case of rod based monomer (a) and dimer (b) antennas with varying lengths.

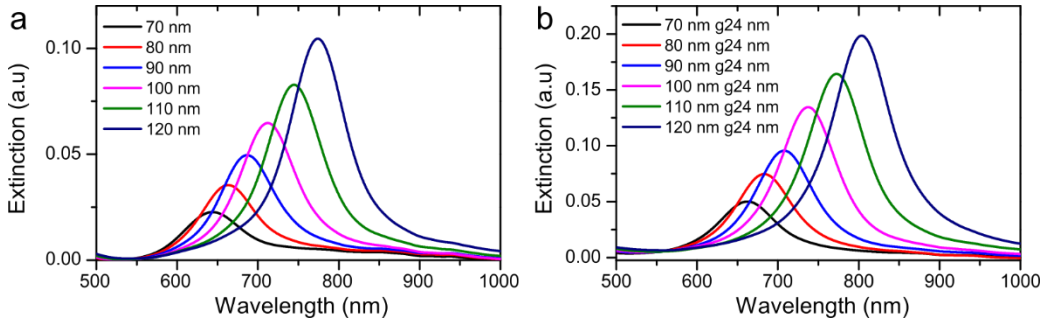

Figure 3-4 Resonant gold nanoantennas. a) Extinction spectra for monomer rod antennas with a width of 50 nm and varying lengths from 70 nm –120 nm. b) Extinction spectra for dimer rod antennas with a width of 50 nm and varying arm length from 70 nm -120 nm, the gap was fixed at 24 nm.

CONFOCAL PHOTOLUMINESCENCE MICROSCOPY

We performed PL measurements on the QDs and QD-antenna devices using home-built confocal microscopes. In general, we used 40x, 1.2 NA water-immersion objectives. The excitation was either continuous-wave (CW) or pulsed laser sources, which were brought into the objective through a dichroic mirror. Wave plates and linear polarizers allowed us to control the polarization of the excitation laser. The QD luminescence was collected through the same objective and sent into different channels depending on the particular measurements. On one channel, the emission was sent through a confocal pinhole (30 µm) and into fast avalanche photodiodes (APDs).

The samples were mounted onto a piezoelectric stage, which allowed to acquire scanned images of the emission intensity from the APD readout. We also used time-correlated single photon counting modules (PicoHarp 300, PicoQuant), either to analyse the transient emission dynamics thru lifetime measurements, or to perform second-order autocorrelation (g^2) measurements when splitting the signal with a 50:50 beam-splitter (BS) in a Hanbury-Brown-Twiss (HBT) configuration. Alternatively, with a flip mirror and an additional lens, we could obtain radiation patterns of the QD and the coupled devices by measuring the PL intensity distribution on the back focal plane (Fourier plane or momentum space) of the high numerical aperture objective. Since different types of QDs were studied in two setups (at different laboratories), the specifics will be detailed in the corresponding sections.

3.3 Excitation Enhancement of a Quantum Dot

Colloidal QDs can exhibit interesting properties such as sequential resonant photon absorption and the existence of multiply excited states.[114,115] The transient PL dynamics of QDs contain at least two contributions, respectively from the singly and doubly (and higher) excited states. An important feature is that the ratio of doubly to singly excited state PL

amplitudes quantifies the local excitation intensity independently on the emission process.[107] In this section, custom synthesized QDs were assembled with disc monomer and dimer gap antennas designed to resonate with the excitation wavelength, in order to quantify the local excitation intensity enhancement provided by the antennas.

A schematic illustration of the studied system is presented in Figure 3-5a, showing a QD attached to a Au dimer antenna via chemical functionalization layers. We focused our analysis on monomers with 90 nm discs, and dimers with same disc size and gaps of 14 nm and 30 nm. Figure 3-5b shows SEM images of one of the dimer gap antennas, while the extinction measurements for these samples are presented in Figure 3-5c. The spectra were taken before the QD deposition, which typically red-shifts the resonance 10-20 nm due to the presence of a high index particle at the antenna hotspot. The green line corresponds to the excitation laser wavelength, while the red shaded area represents the QDs´ emission band. The antennas are closely resonant to both the excitation wavelength and the spectral range of luminescence detection.

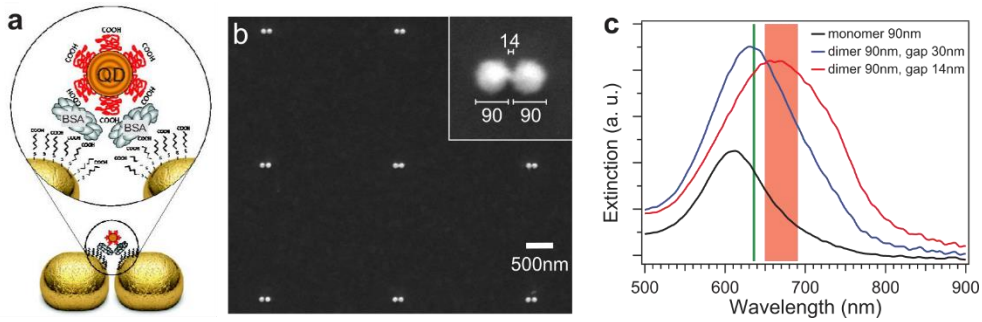

Figure 3-5. QD-antenna system. a) Schematic illustration of the investigated QD-dimer antenna system. b) SEM image of the fabricated dimer gap antennas. The antennas are 90 nm disc dimers separated by a 14 nm gap, and arranged in a 2 μm pitch array. c) Extinction spectra representative of the studied antennas. Monomer of 90 nm diameter (black), and 90 nm disc dimers with gaps of 30 nm (blue) and 14 nm (red). The positions of the excitation wavelength and collection emission window, are depicted by the green line and the red shaded frame respectively.

3.3.1 Photoluminescence characterization

The assembled devices were characterized with a confocal PL setup by Dr. Jeròme Wenger, at the Fresnel Institute in Marseille, France. For the excitation, a pulsed laser diode operating at 636 nm (50 ps pulse duration at 40 MHz) was used, and the emission was filtered over the 650-690 nm range of the QD emission. Figure 3-6a shows confocal PL images corresponding to the 14 nm gap dimer antennas excited with a polarization parallel (left) and transversal (right) to the dimer long axis.

In general, we found out 80% of the antennas showed QD PL, from which 50% exhibited excitation polarization sensitive emission (antennas circled in red). For those antennas, the

PL ratio between the parallel and transversal excitation was higher than 10. Another signature of the near-field coupling between the dimer antenna and the QD was found in the radiation patterns. The images in Figure 3-6b show the radiation patterns (back focal plane images) for a QD on ITO (left), QD-monomer (centre) and QD-dimer (right) cases. Two distinct circles are seen in the polar angle. The outer one corresponds to the maximum collection angle of the 1.2 NA objective (64º), while the inner circle corresponds to the critical angle for the glass-air interface (NA=1 or 41.1º), where a dipole close to a glass interface is expected to emit with a sharp maximum.

The first two patterns (isolated QD and QD-monomer) are isotropic in the azimuthal angle, as direct consequence of the QD degenerate transition dipole moment. In contrast, when the QD is coupled to the dimer gap antenna, the radiation pattern changes dramatically and transforms to that of a linear dipole horizontally aligned respective to the interface. Hence, the antenna mode fully determines the QD radiation pattern, which evidences the QD-antenna coupling, as observed previously by Curto *et al*.[37]

For QDs lying on the bare ITO surface, we observed a reduced exciton lifetime compared to QDs on glass from 9.5 ns to 2 ns. Furthermore, the blinking dynamics are strongly suppressed in the QD-on-ITO case (see the blue time trace in Figure 3-6c). These features relate to the energy transfer from the QDs to the conductive ITO layer, as previously reported.[116] Interestingly, the blinking dynamics are partly retrieved for the case of the QDs coupled to the antennas, as can be seen in the red time trace in Figure 3-6c, which is also indicative that the QDs are coupled to the antennas.

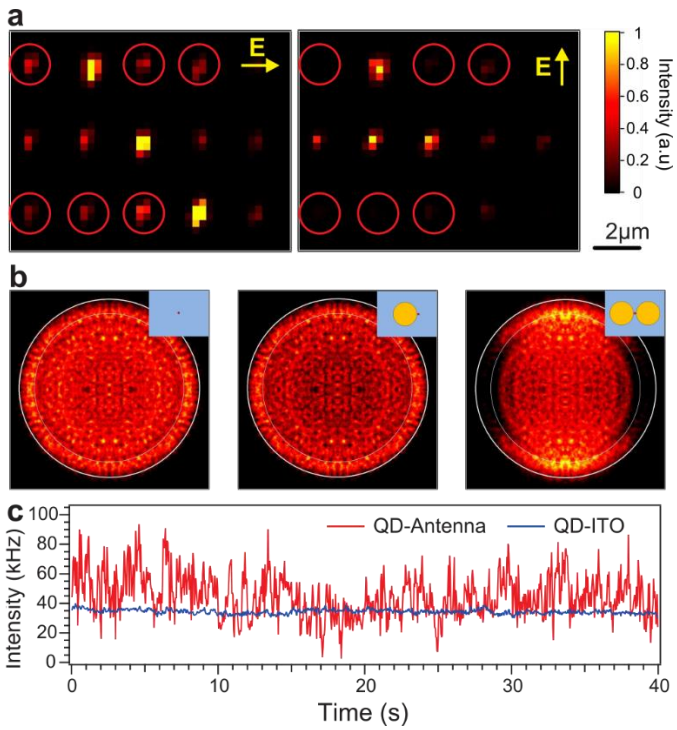

Figure 3-6. Optical characterization of QD-antennas. a) Confocal PL images for an excitation polarization parallel (left) and transversal (right) to the dimer long axis. The gap size is 14 nm. The red circles indicate the selected antennas for the PL studies. b) Radiation patterns (back focal plane image of the 1.2 NA objective) from a QD on ITO (left), a QD coupled to a single gold disc (centre), and another QD coupled to a dimer gap antenna (right). c) Emission time traces for a QD on ITO (blue) and QD coupled to a dimer antenna (red) with an average excitation power of 10 μW.

EXCITON AND BI-EXCITON DYNAMICS

Semiconductor QDs can sustain multiply excited states due to sequential resonant photon absorption provided by their strong quantum confinement of free charge carriers.[114] Below PL saturation, the exciton state (X) mostly results from the absorption of a single photon while the bi-exciton state (BX) is created after the sequential absorption of two photons (schematic in Figure 3-7a). Thus, following a pulsed excitation, the X and BX relative populations scale linearly and quadratically (respectively) with the excitation intensity. The X state radiative lifetime is in the order of a few nanoseconds, while the BX lifetime is dominated by Auger recombination and ranges between ten and a few hundreds of picoseconds (Figure 3-7a). The latter, allows us to distinguish between the X and BX populations by monitoring the QD's transient emission dynamics.[115] The lifetime trace $s(t)$ can be decomposed as a sum of two exponentials:

$$s(t) = a_X \exp(-t/\tau_X) + a_{BX}\exp(-t/\tau_{BX}) \qquad (3.1)$$

where a_X and a_{BX} are the amplitudes of characteristic decay times τ_X and τ_{BX} respectively. These amplitudes can be expressed as a function of the radiative decay rate k_i^{rad} for the i-th multi-exciton state and the average number N_{abs} of absorbed excitation photons per QD per pulse[107,115]:

$$a_X \propto k_X^{rad} N_{abs} \quad (3.2)$$

$$a_{BX} \propto k_X^{rad} (r-1) {N_{abs}}^2 \quad (3.3)$$

here, $r = k_{BX}^{rad}/k_X^{rad}$ is the degeneracy factor of the BX state, which typically amounts to a constant value r≈2-3 fixed by the nature of the QD.[117]

From equations (3.2) and (3.3) we note that both a_X and a_{BX} are linearly proportional to the radiative rate k_X^{rad}, meaning that both do sense the same emission rate enhancement from plasmonic antennas. Secondly, a_X bears a linear dependence with N_{abs} (i.e. local excitation intensity), while a_{BX} has a quadratic dependence.

Figure 3-7b-d presents experimental decay traces and the corresponding bi-exponential fits according to Equation (3.1). These decay traces are normalized to better reveal the modifications of the decay dynamics and the increased relative weight of the fast BX transient component with increasing excitation power. For the QD-on-ITO, the exciton lifetime amounts to τ_X=2.0 ns, while for the QDs coupled to the monomer and dimer antennas, we find τ_X=0.18 ns after deconvolution from the instrument response function. This corresponds to a lifetime reduction or excitonic decay rate enhancement of 11.1 when the QDs are coupled to the resonant antennas.

For all samples tested, a bi-exciton lifetime of τ_{BX}=0.12 ns was extracted, limited by the instrument response function. Such a short lifetime confirms the Auger recombination route strongly affects the BX to X decay. The excitonic and biexcitonic amplitudes a_X and a_{BX} are displayed in the right panel of Figure 3-7b–d. As expected from Equations (3.2) and (3.3), a_X grows linearly with the excitation intensity, while a_{BX} grows quadratically. The evolution of $a_{BX}$with the excitation power confirms the fast transient component in the decay trace corresponds to the biexcitonic process BX.

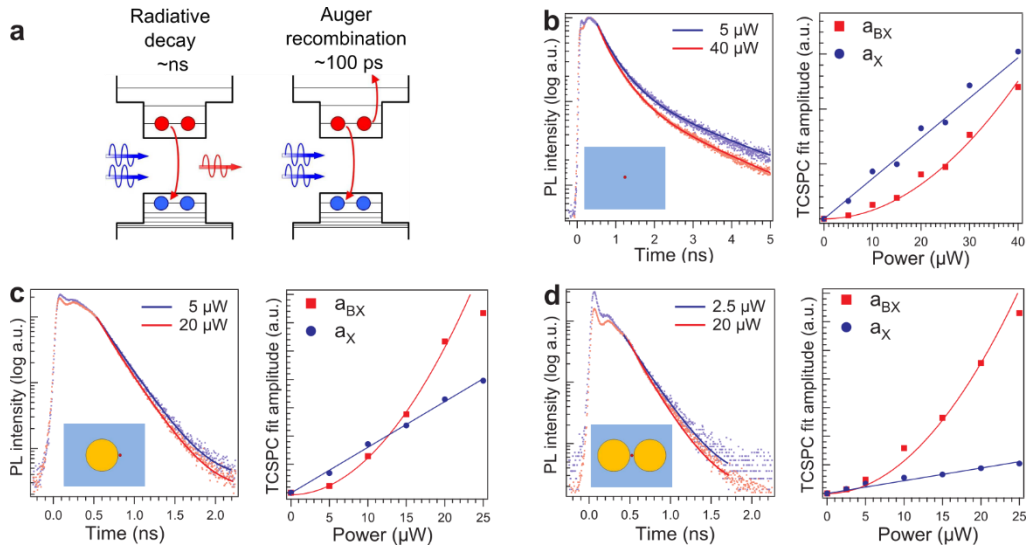

Figure 3-7 Dynamics of the QD exciton and biexciton states. a) Scheme of the decay routes for the biexciton state (BX). b-d) Fluorescence lifetime decay curves and bi-exponential fit amplitudes a_X (blue) and a_{BX} (red) for the QD-on-ITO (b), QD-monomer antenna (c) and QD-dimer antenna with 14 nm gap (d). The light grey traces show the instrument response function. Note the different scale for the excitation power in (b) compared with (c,d).

When computing the ratio a_{BX}/a_X, the emission rate contribution cancels out, and only a term proportional to the local excitation intensity remains. As r is a constant, a_{BX}/a_X is a direct probe of the local excitation intensity. An increase in this ratio on a nanoantenna as compared to a flat interface is a direct demonstration of an increased local excitation intensity, independently of the number of emitters involved and the emission enhancement.

From the data set in Figure 3-7b-d, we computed the ratio a_{BX}/a_X, which follows a linear trend with increasing excitation power (Figure 3-8a). For all excitation powers, the a_{BX}/a_X ratio on plasmonic antennas exceeds the one extracted for the ITO reference. As demonstrated by Equations (3.2) and (3.3), this effect is directly related to the excitation intensity amplification induced by the antenna. To quantify the excitation intensity enhancement, we take the ratio of the slopes in Figure 3-8a, which provides a better estimate with a typical relative uncertainty of 10% for the excitation enhancement factors of the different selected antennas.

The orange bars in Figure 3-8b summarize the main results. The excitation enhancement factor starts at 5.1 for a single disc antenna. For the dimer antennas, as the gap is reduced, the electromagnetic coupling between the gold particles increased.[118] Our observations confirm this trend by an increase in the excitation enhancement from 13.1 to 15.9 when the gap is reduced from 30 nm to 14 nm. Let us stress that these enhancement factors of the excitation intensity sensed by the QDs are independent of the number of emitters involved in the luminescence signal and on the emission properties.

The experimental results also stand in good agreement with numerical simulations based on the finite-difference time-domain (FDTD) method (yellow bars in Figure 3-8b). The only exception concerns the case with largest enhancement (dimer with 14 nm gap excited with parallel polarization), for which nanofabrication deficiencies, non-ideal QD positioning and more complex photo-dynamics have a non-negligible influence.

To quantify the luminescence enhancement, the ratio of the average levels of luminescence is computed from the time traces, and assume the detected signal stems from a single QD. We recall that the QDs used in this work are custom synthetized to bear a high BX population. Although this feature is an advantage to determine the a_{BX}/a_X ratio, it also makes it difficult to successfully implement the HBT experiment, as the biexciton emission can blur out the single photon anti-bunching dip that guarantees the presence of a single quantum emitter.

Instead, clues for the single emitter-antenna devices are brought by (i) the blinking dynamics down to the background level (Figure 3-6c), and (ii) the luminescence intensity level of the selected antennas as compared to other antennas, where most likely more than one QD is present (compare the intensity levels in Figure 3-6a for the circled and un-circled antennas).

For the reference on the ITO substrate, we focus on an area with very low QD coverage density, where each bright spot is diffraction-limited and the intensity of the bright spots follows a Poisson-like distribution. Selecting the spots with minimum intensities promotes the cases where most likely a single QD is present. Figure 3-8c summarizes the enhancement factors found for the PL intensity. While we find a value of 2.7 for the monomer antenna, the luminescence is only enhanced by a factor of 1.3 for a dimer antenna with 14 nm gap and parallel excitation, despite that this configuration lead to a 15.9 excitation intensity enhancement. The situation is even worse for the dimer with perpendicular polarization orientation, where the luminescence factors drops to 0.25 of ITO reference.

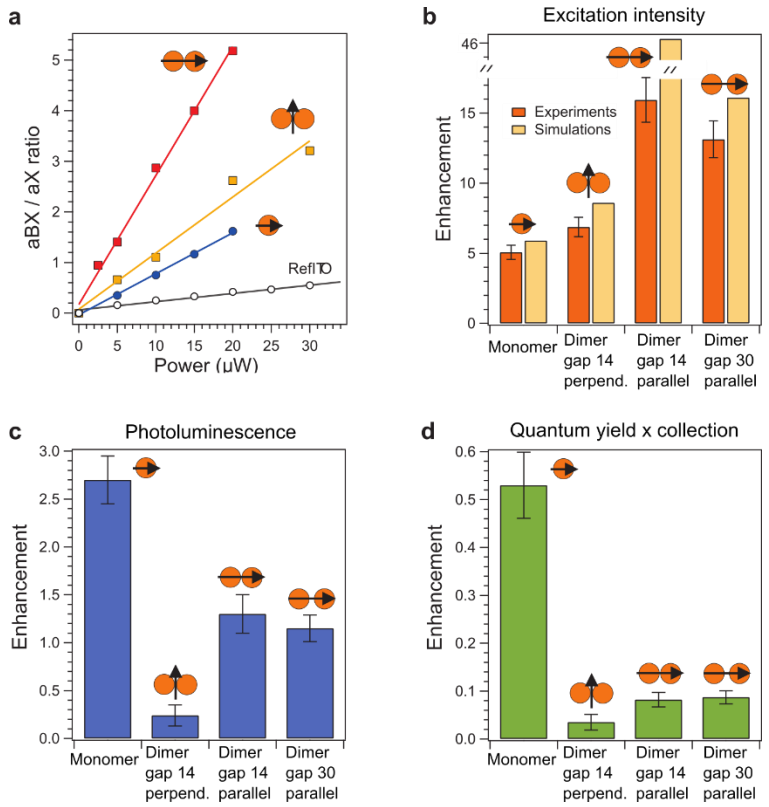

Figure 3-8. Summary of the QD-hybrid device emission properties. a) Ratio of bi-excitonic/excitonic amplitudes as a function of excitation power for a QD-on-ITO (black), a QD-monomer (blue), and a QD-dimer gap antenna with transversal (orange) and parallel (red) excitation polarization. b) Excitation enhancement deduced from the data slopes in (a). c) Integrated PL enhancement. d) Quantum yield and collection efficiency deduced from the data in (b) and (c).

We remind that for all the different cases of this study, the exciton decay rate increased by a factor 11.1 as compared to the ITO reference. The fact that the luminescence enhancement is smaller than the decay rate and excitation intensity enhancements is an indication of quenching (i.e. the non-radiative energy decays take the lead over the radiative routes).

In the excitation regime below PL saturation, the luminescence enhancement is proportional to the gains in collection efficiency, quantum yield and excitation intensity. Thus, from the measurements of the excitation and luminescence enhancement factors (Figure 3-8b,c), we compute the enhancement factor for the QD quantum yield multiplied by the collection efficiency. The results are displayed in Figure 3-8d. For all configurations, values below unity are obtained, which further evidences luminescence quenching.

Our observations support the fact that the quenching losses also increase as the gap size is reduced:[67] antennas with gaps of 14 or 30 nm are found to provide almost the same quantum yield enhancement, although the excitation enhancement was found to be significantly higher for the 14 nm gap case. A remarkable feature of our study is that excitation intensity enhancement can be recorded despite this quenching phenomenon, and that near-field intensity information can be extracted from emission even in the presence of strong non-radiative losses.

3.4 Revealing the quantum dot positioning

As mentioned in the previous section, due to the large BX population of these custom synthesized QDs, it was not possible to uncover the single emitter characteristics using on the standard HBT experiment. Instead, in order to evaluate the ability of this method to provide reproducible single emitter devices, we used the commercially available QDs (section 3.2.1), which in general allow for successful HBT measurements. Previous studies have shown clear anti-bunching dips characteristic of single photon emission, including QD-antenna systems assembled with the current positioning method.[37,110]

In our confocal setup, a 632.8 nm He-Ne CW laser was used as our excitation source, and the emission was filtered in the 700-850 nm range by means of a dichroic mirror and additional filters. First, as a reference, QDs were dispersed on a glass substrate and were observed to have good single photon properties. Figure 3-9a shows a fluorescence time trace of one of these QDs, where the blinking dynamics can be well appreciated in the inset with shorter time span (acquisition time was of 5 ms). The feature observed in the time trace (time window between 750 s and 950 s), could be associated with the QD transitioning into a "grey" state of lower quantum efficiency. By splitting the emission signal into two APDs, second-order auto-correlation measurements could be performed. Figure 3-9b demonstrates the nearly perfect anti-bunching (g^2~0), proving that indeed we were measuring a single QD. By performing an exponential fit of the dip, a lifetime of ~67 ns is deduced, which is common for isolated QDs on a dielectric substrate.

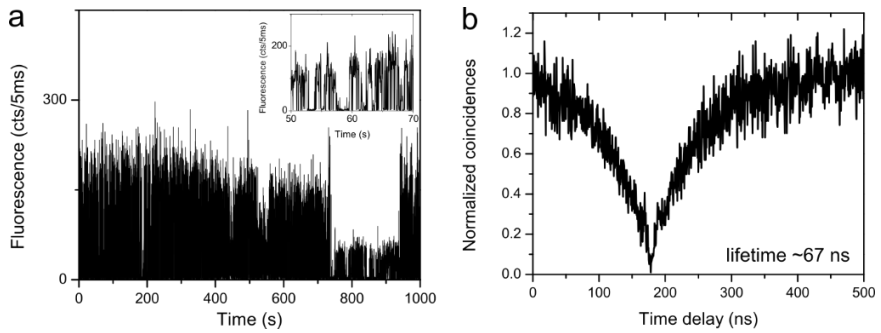

Figure 3-9. Single photon characteristics of a QD. a) Fluorescence time trace of a QD on a glass substrate. The blinking dynamics can be well appreciated in the inset. b) Auto-correlation measurement of the emitted photons showing a nearly perfect anti-bunching dip. The fitted lifetime was 67 ns.

Next, we prepared monomer and dimer gold nanoantennas with varying antenna arm lengths (the extinction spectra in Figure 3-4 correspond to these devices). For the second lithography step, the focus was on those antennas with resonances matching the emission wavelength of the QDs, and exposed 50 nm holes aligned to the hotspots of the antennas as described in section 3.2.3. Figure 3-10a,b presents the confocal PL scans of 10x10 arrays of monomer antennas with a length of 110 nm, and dimer antennas with gaps of 24 nm and arm length of 110 nm, respectively. The two top rows remained unexposed during the second lithography step, which allowed distinguishing between the background Au auto-luminescence and the presence of QDs at the antennas. The circled antennas produced reasonable coincidence counts to identify a dip at zero time delay during the HBT experiment. Figure 3-10c-d shows examples of antennas hosting a single emitter ($g^2<0.5$) and a few emitters ($0.5<g^2<1$), plotted in orange and magenta respectively.

To estimate the number of emitters present at the antennas, the height value of the anti-bunching dip at zero time delay was extracted. The histograms associated with these two arrays are presented in Figure 3-10e-f, which show that although single QDs can be positioned with this method, the occurrence of 2-3 QDs is more likely. From the anti-bunching curves, we can also notice the dips are much narrower than for a single QD at the glass substrate. These coupled QDs exhibit consistently lifetime values in the order of 2 ns, evidencing an order of magnitude enhancement in the decay rate of the QDs.

Our observations on the QD emitter occurrence are in agreement with those reported by Curto *et al.*[110] However, it is difficult to provide precise single emitter positioning yield from the arrays, since many antenna devices could not be fully assessed due to photobleaching of the QDs during continuous excitation (i.e., cases where single emitter type blinking was observed, but the emission faded before we could reliably record an autocorrelation measurement). This problem could be overcome, for example, by using QDs with reduced blinking dynamics and higher emission stability over continuous excitation periods.[66]

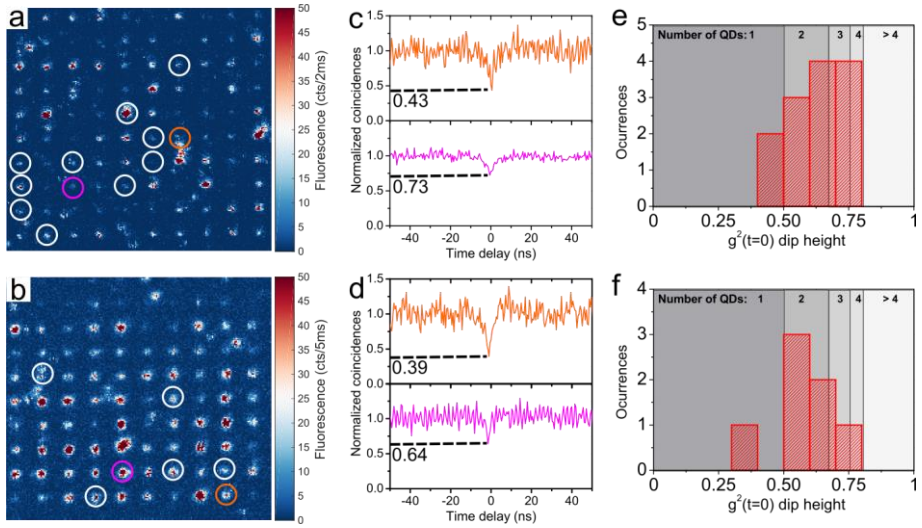

Figure 3-10. Few QDs coupled to dimer antennas. a-b) Fluorescence confocal images of a monomer and dimer array respectively, with QDs positioned with the EBL method. The circled areas correspond to those antennas with dips in the auto-correlation measurements. c-d) Examples of anti-bunching curves for the antennas exhibiting a single emitter (orange) and few emitters (magenta). e-f) Histograms of the extracted height value at zero time delays. The shaded areas represent the expected number of QDs from a simplified model that assumes equal emitters contributing to the photon counts.

It is worth mentioning that this method is far from perfect in the sense that often, the lift-off process following the QD incubation can lead to a number of residual QDs in areas outside the antenna positions. Figure 3-11a shows a clear example of an array where certain areas around the antennas showed significant emission contributions. We investigated these samples under the SEM to get an idea on the nature of these extended fluorescent areas.

It was indeed possible to image the individual QDs under the SEM, probably enabled by the polymer coating, which makes them large enough to visualize under the electron microscope. Figure 3-11b-e shows SEM images corresponding to the coloured frames in the confocal image. Figure 3-11b clearly shows a large number of QDs in this substrate area, hence it is straightforward to understand the measured broader fluorescence in the area below the antenna. However, the antennas shown in Figure 3-11c-e also presented a large number of QDs, which was hard to know from the confocal scans since all these QDs are within the diffraction limited confocal spot.

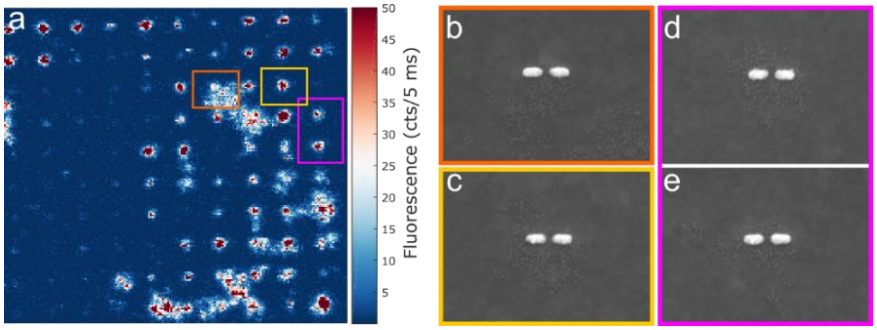

Figure 3-11. Residual QDs after lift-off. a) Fluorescence confocal image of an array of antennas with QD emission. Due to problems with the lift-off process, fluorescence emission was also observed stemming from between the antennas (e.g. the area inside the orange frame). b-e) SEM images of the areas delimited in (a). For b) we expected to observe such residues of QDs. However, for the areas shown in c-e) the confocal image exhibited a single bright spot, for those spots we also observed QDs spread in the vicinity of the antenna outside the intended areas.

Being able to distinguish the presence of the QDs by SEM imaging, we had a closer look at other areas in the sample and found out a surprising result: the positioning method does not yield specific binding of the QDs only the gold areas, as initially considered.[37] From areas such as those presented in Figure 3-11, that conclusion is not possible, since the QDs are randomly dispersed around the antenna regions (likely from a bad lift-off step). However, on areas that had a cleaner lift-off, we consistently observed QDs within the complete exposed area (i.e. both on the Au and substrate areas). This is clearly observed for example, when imaging the areas of our alignment marks (Figure 3-12a), which during the lithography are consequently exposed with a 1.2 µm square window by the EBL align procedure (red dashed line). The QDs are dispersed uniformly within this window, while the area of the substrate outside this region is free from QDs.

The exposed antennas were also examined. To have a reference of the exposed area, the sample was imaged before the QD incubation and lift-off. Figure 3-12b shows the SEM image of a dimer gap antenna with a 50 nm hole centred at the gap. Although there was a small misalignment from the symmetry axis of the antenna, the Au and substrate surfaces were both available to the MUA layer and QDs. Figure 3-12c presents two cases where we could identify a single QD exactly at the centre of the gap antenna, showing that it is indeed possible to obtain such single emitter devices with this method. However, the majority of the antennas provided a different picture, as it can be seen in Figure 3-12d showing five examples. The top panels are the raw SEM images, while the middle panel are contrast enhanced to help the reader localize the QDs, which are represented as red dots in the bottom panel. This examination showed us that the QDs could be found either very close to the gold surface but also at the substrate surface within the area delimited by the 50 nm hole.

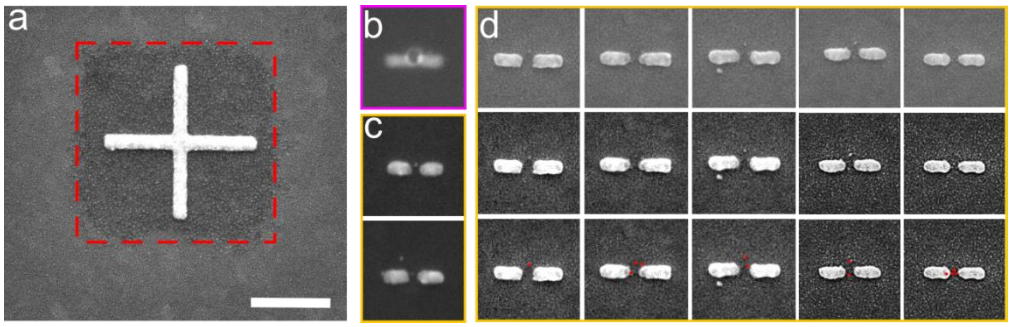

Figure 3-12. Non-specific binding of QDs. a) SEM image of the exposed area of an alignment cross evidencing the non-specific binding of QDs to the non-gold areas of the substrate. b) SEM image of a 50 nm hole aligned with a gap antenna after the development step. c) SEM images of dimer antenna examples with only a single QD noticeable at the gap. d) SEM images of dimer antennas with QDs present anywhere within the lithography hole (no specific binding to gold). Scale bar in (a) is 500 nm.

It was recently suggested by Rabouw *et al*, that the presence of QD residues with this method was due to the diffusion of QDs through the PMMA layer during the incubation.[119] However, we can confirm and argue that this is not the case, since for a well performed lift-off step, QDs are not found in areas outside the exposed regions (Figure 3-12a). Instead, PMMA residues or surface modification of the substrate during the EBL exposure could be promoting the binding of either the self-assembled molecules or the QDs to the exposed regions,[120] independently of whether the Au surface is available.

To test this argument, we performed the chemical functionalization steps on two samples without Au structures. Figure 3-13a shows SEM images of a sample that was subject to the same functionalization protocol after development of an EBL exposure, and imaged after the lift-off step. As observed both on the cross structure design (left) and the rectangular areas (right), there are QDs in the exposed regions, while the rest of the substrate is clear. In a second sample, we eliminated the step of the self-assembled MUA layer and only incubated the exposed sample to the QD solution (Figure 3-13b). The SEM images in this case showed the absence of QDs in the exposed areas, which interestingly in both cases could be identified with the SEM (brighter areas), suggesting that indeed there is a superficial layer of residues within the exposed regions.

We did not investigate in detail the composition of these residues, however, previous studies suggest that these are likely thin polymer residues left after e-beam exposure. It has been reported that residues as thin as a few angstroms can be found even in overexposed areas that have been cleaned with the standard development and lift-off processes.[120] We think such residues are promoting the assembly of the MUA molecules regardless of the Au surfaces. A common solution to remove residual resist is to perform oxygen plasma treatment. However, with our positioning method, it could compromise and enlarge the hole size where we want to located the QDs. In this sense, further development of such chemical

based positioning methods should take into account the presence of this layer, in order to provide clean surfaces for the subsequent chemistry binding protocols.

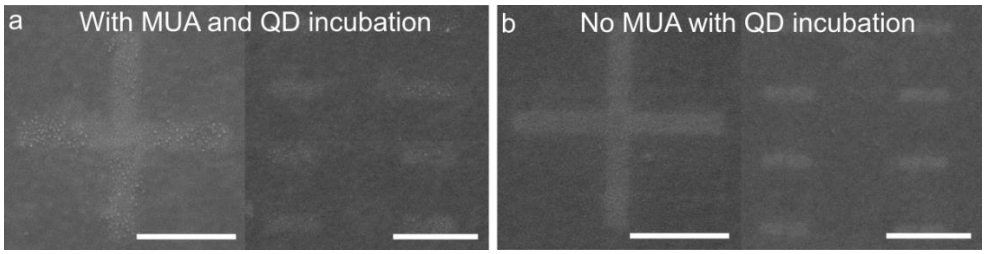

Figure 3-13. Non-specific binding of QDs. a) SEM images of exposed areas after incubation with the self-assembled MUA layer and QDs. b) SEM images of exposed areas after incubation only with QDs (i.e. no MUA layer). Scale bars are 500 nm. The QDs, here recognized as small white particles, are only noticeable in the MUA plus QD incubation case.

3.5 Conclusions and Outlook

The possibility to couple a few, or even down to single QDs, with resonant plasmonic antennas, allowed us to experimentally investigate the excitation enhancement experienced by the quantum emitters when coupled to disc monomer and dimer gap antennas resonant to the excitation wavelength. Analysis of the transient emission dynamics was performed by studying the lifetime decay of the QD-antenna devices as a function of excitation power. We found out up to a 15-fold excitation enhancement for the case of a dimer antenna with a gap of 14 nm, however with a considerable reduction in the quantum yield due to non-radiative losses. This measurement approach provides new routes to experimentally investigate the physics of optical antennas, and optimize the excitation and emission processes independently for the future development of bright single-photon sources.

In a later stage, a limitation to the positioning method based on the combination of high precision lithography and chemical functionalization was identified. We found out that residual layers left after the EBL exposure can promote the binding of the self-assembled molecules to both the ITO coated substrate and the Au structures, thus hindering the specificity of the protocol. Despite this, it is still possible to obtain isolated QD-antenna devices due to the small localized areas provided by the PMMA mask, even with single QD-antenna cases as demonstrated by the auto-correlation measurements.

Future work could take advantage of this residual layer, and its specificity to the self-assemble molecules. Since it is not necessary to rely on the MUA affinity to Au, it should be possible to expose small sub-50 nm holes onto general photonic or plasmonic structures to assemble few down to single QDs without the need to develop specific chemistry protocols for the different materials.

Chapter 4 Coupling of Nitrogen-Vacancy centres to channel plasmons

Efficient light-matter interaction lies at the heart of emerging technologies that seek on-chip integration of solid-state quantum photonic systems. Plasmonic waveguides, which guide energy in the form of strongly confined surface plasmon-polariton modes, represent a promising solution to manipulate single photons in coplanar architectures with small footprints. In this chapter, we demonstrate coupling of the emission from Nitrogen Vacancy (NV) centres in nanodiamonds, to the channel plasmon polariton modes supported by V-groove plasmonic waveguides. Theoretical simulations shed light on the requirements of the emitter´s position and orientation for optimum coupling. Experimentally, we first present the coupling from multiple emitters in randomly positioned nanodiamonds, which provide insight into the coupling characteristics in this hybrid system. Subsequently, individual nanodiamonds containing a single NV centre were deterministically positioned inside the VGs, for which emission coupling to the plasmon waveguide modes was observed. Concomitantly with the theory predictions, we demonstrate experimentally that 42% of a single NV centre emission efficiently couples into the V-groove supported modes.

4.1 Integration of Nitrogen Vacancy centres with plasmonic structures

Over the past decade, the integration of Nitrogen Vacancy (NV) centres with plasmonic structures has been motivated by their remarkable characteristics (brightness and room temperature stability), which make them very promising solid-state single photon sources,[76] while the presence of a triplet spin state is extremely appealing for solid-state quantum computing schemes.[121,122] Furthermore, their proximity to the diamond surface, either in nanoparticles or in bulk (shallow NVs),[78] makes them suitable for the interaction with the localized electromagnetic fields provided by structures supporting surface plasmon polariton modes.

Fully exploiting the capability of NV-plasmon coupling requires high-accuracy control of the relative position between the emitter and the electromagnetic (EM) modes supported by the plasmonic structures. A deterministic assembly can enable, among others, the precise control of the emission dynamics of the NV centres (excitation/emission rate enhancement), on-chip routing of the NV´s emission, and quantum bit entanglement.[123] These features make this task highly relevant for applications in integrated solid state quantum devices such as single photon sources or quantum networks, both for free-space and on-chip platforms.[50]

In recent years, different coupled systems using NV centres have been demonstrated. In 2009, Schietinger *et al* demonstrated the controlled coupling between nanodiamonds (NDs) containing single NV centres and spherical gold nanoparticles, by positioning them with an AFM cantilever.[102] The same year, Kolesov *et al* demonstrated the wave-particle duality of single surface plasmons launched by a single NV centre coupled to a silver nanowire (NW).[29] However, the latter work relied on the random assembly of the nanoparticles to enable the coupling. Shortly after, both Huck *et al* and Schell *et al* implemented the AFM nanomanipulation technique to deterministically assemble single NV-NDs with colloidal silver NWs, demonstrating a better controlled coupling to the guided modes of the NWs.[103,38] Kumar *et al* then exploited this platform to realize more complex structures, showing the coupling of the NVs to a gap NW configuration[124] and also demonstrating a plasmonic Y-splitter.[22]

Despite these achievements, the use of metallic colloidal NWs poses a limitation into those plasmonic circuitry designs that can meet scalability requirements. In this context, top–down lithography-based fabrication techniques could in principle overcome this issue, however the resulting structures usually suffer from larger losses.[125] So far, mainly the coupling to metallic nanoantennas and NWs have been

explored, despite the availability of other plasmonic architectures with appealing performances.

In this chapter, we present the first demonstration of NV centres coupled to a different type of waveguide, namely the V-groove (VG) plasmonic waveguide.[55] An ideal scenario of this platform is schematically illustrated in Figure 4-1, where a single NV in a ND is placed inside a gold VG channel, and upon external optical excitation (e.g., green laser pump), it is able to couple all of its emission into the propagating modes of the VG waveguide. In this case, the coupled energy is eventually scattered-out into free-space modes at the VG end mirrors.

First, we present details on the experimental methods including the assembly and characterization approach. Next, we focus on the theory simulations results on the position and orientation requirements for a dipole emitter inside a VG to achieve optimal coupling to the propagating modes. Experimentally, we first show coupling from multiple NV-NDs assembled in a random fashion. Afterwards, by deterministically assembling the NV-VG devices, coupling from single NV centres to the CPP modes supported by the VG channels is demonstrated, including energy transfer from a single emitter over a 5 μm distance before out-coupling its energy into free-space propagating light by means of tapered nanomirrors.

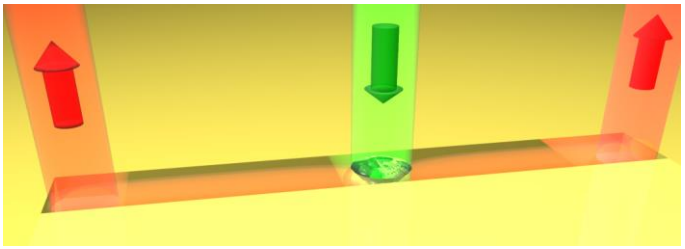

Figure 4-1. NV-VG hybrid device. Schematic illustration of a nanodiamond assembled inside a V-groove gold channel. Upon optical excitation (e.g. green laser), in the ideal scenario, the NV centre couples all of its emission into the VG channel plasmon modes, which in this case propagate along the channel and scatter out to free-space modes at the end mirrors.

4.2 Materials and Methods

4.2.1 Nanodiamonds with Nitrogen Vacancy Centres

A variety of NDs containing defect centres are commercially available, with NDs varying in particle size, surface functionalization and number of defects per particle. For this work, we used different types of NDs. For the experiments concerning the coupling of multiple NV-NDs, the particle solutions labelled as ND-15NV with 40 nm particles, were purchased from Adamas Nanotechnologies. For the work on

individual NV centres, the NDs were purchased from Microdiamant (MSY 0–0.2 µm), and were post-treated to clean and functionalize the NDs with carboxylic groups. This post treatment was carried out by Jana Say in the group of Prof. Louise J. Brown at the Macquarie University in Australia.

4.2.2 V-groove waveguides

The waveguides used in this chapter are the focused ion beam (FIB) based VGs (Section 2.2.1), fabricated by Dr. Tobias Holmgaard at Denmark Technology University, and characterized by Dr. Ilya Radko in the group of Prof. Sergey Bozhevolnyi at the University of Southern Denmark. Specifically, an FIB was used to carve a 2 µm thick gold film deposited on a Si substrate. The structures are ~315 nm wide and ~510 nm deep, have an opening angle of ~24º and a length of 10 µm (Figure 4-2a). The VGs are terminated with ~650 nm long width-constant tapers, forming triangular-shaped nano-mirrors that enable efficient in and out-coupling of light (Figure 4-2b). The V-shape profile of these waveguides is appreciated in the transversal cut generated by means of a FIB milling procedure (Figure 4-2c).

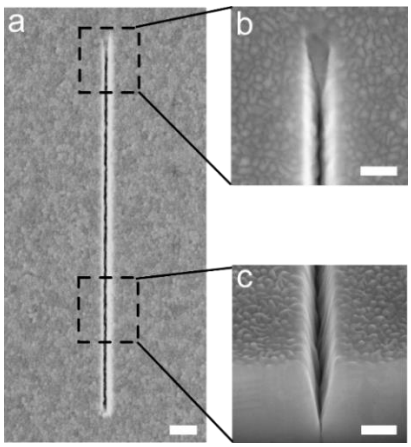

Figure 4-2. V-groove waveguides fabricated with the FIB technique. a) SEM image of a 10 µm long VG. b) Zoomed-in image at a tapered nanomirror. c) Transversal cut showing the V-shape profile. Scale bars are 1 µm for (a) and 300 nm for (b) and (c).

4.2.3 Dual positioning approach

To position a single ND inside a VG, two recently developed nano-positioning techniques for quantum emitters were combined, namely the use of electron beam lithography (EBL) based assembly,[37] and the nano-manipulation of individual particles with an atomic force microscope (AFM) tip,[102,126] as introduced in Section

2.4. The first step is to create a mask by means of e-beam lithography (EBL). We start by spin coating a 120-nm-thick layer of poly(methyl methacrylate) (Microchem, 950 k 4 wt% diluted 3:1 with trichloromethane), also known as PMMA, and bake it at 90 ºC for 15 min on a hot plate. The baking temperature was set lower than the typical 175 ºC used for this type of resist in order to avoid deformation of the VG structure due to the Au annealing.

We then patterned an array of 200-nm holes by EBL. The pattern was positioned in close proximity to the VG by using a set of alignment marks that were milled during the FIB process. The sample was then developed in a 1:3 solution of Methyl isobutyl ketone (MIBK) and isopropanol (IPA) for 45 s. Next, we placed a drop of solution containing a positively charged polyelectrolyte (poly) diallyldimethylammonium (Sigma Aldrich, MW 200,000–3,500,000, 2 wt% in Milli-Q water, Millipore), also known as PDDA, onto the structures to perform an electrostatic assembly.[126] After 5min of incubation, the sample was rinsed with deionized water to remove excess of polyelectrolyte and blow dried in a N_2 stream. We then placed a drop of a ND solution (particle radii in the range of 40–80 nm) and let it incubate for 30 min. To avoid an excess of particles during the lift-off we first removed the solution drop with a pipette and rinsed the sample in IPA. Finally, a lift-off of the PMMA, in acetone at 55 ºC during 30min, followed by rinsing in IPA and blow-drying in a N_2 stream left us with the VG surrounded by the designed pattern of NDs.

Next, the samples were measured by means of confocal fluorescence imaging in order to identify the location of the NDs containing single NV centres. Finally, in the second positioning step, we implemented an AFM in tapping mode for visualization and in contact mode to move the selected NDs across the Au film and into the VG.

For the first experiments on the coupling of the NV centres to the CPP modes supported by the VGs, we relied on the basic random positioning of NDs containing multiple NV centres. Later, for the case of NDs with single NV centres, we implemented this two-step deterministic positioning method, using the EBL and AFM techniques. As seen next, this approach was fundamental to assure the quantum nature of our assembled device.

4.2.4 Experimental setup

To optically characterize the NVs and the hybrid devices, we implemented a homemade PL optical microscope. The substrates with NDs and VGs were attached facing down on a glass coverslip, and mounted on a sample holder on a 3-axis piezoelectric stage. For the excitation, either a 532 nm continuous wave (CW) laser (Ventus) or a 532 nm pulsed laser (LDH-FH, Picoquant) were used according to the

specific characterization. A dichroic mirror is used to reflect the excitation beam into our microscope objective (Olympus 60x, 1.25 NA). The emission was collected through the same objective and the dichroic mirror filters out the excitation light. Three different channels were available to analyse the emission of our samples.

On one channel, the light is sent through a confocal pinhole from which we then collected light into two avalanche photo diodes (APDs) by means of a 50:50 beam-splitter. This channel allowed us to acquire fluorescence images and perform auto-correlation measurements (Picoharp 300, Picoquant). In a second channel, the emission was directed to an EMCCD camera (Hamamatsu) for wide-field imaging of the fluorescence contributions. In the third channel, the emission was collected into a single-mode fibre connected to another APD for lifetime measurements. By steering a mirror, we could selectively collect the emission into the fibre from different areas within our field of view, allowing us to independently analyse the signal directly out-coupled to free-space by the NVs and the one scattered out from the VG ends. The Picoharp system also allowed us to perform fluorescence lifetime measurements of the NV centres when using the pulsed laser source. In all the experiments, the excitation polarization was adjusted by combining a linear polarizer and a half-waveplate, while the collection polarization was filtered with a linear polarizer.

4.3 Theory simulations

The theory simulations presented in this chapter were carried out by Carlos Gonzales-Ballestero in the group of Prof. Francisco J. García-Vidal at the Universidad Autónoma de Madrid (UAM) in Spain. The simulation results provide valuable insights into the operation of such hybrid emitter-VG devices.

The characterization of the hybrid system comprised of a VG and a single quantum emitter (here modelled as a dipole emitter) was carried out in two steps. The first step consisted of a 2D simulation to determine the CPP mode profile supported by an infinitely long VG.[127,128] The EM field distributions were calculated numerically with the Finite Element Method, using the COMSOL multi-physics tool. The structure of the VG considered in the numerical simulations has the following main geometric properties: an aperture angle of 24º at the bottom, with a 15 nm radius rounded bottom, a depth of 510 nm, and a width of 315 nm, in close resemblance to the geometry observed in the SEM images (Figure 4-2). The surrounding dielectric material is assumed to be air ($\varepsilon=1$), whereas the gold is described by an experimentally fitted Drude-Lorentz formula.[129] By solving a standard 2D eigenvalue problem, we were able to obtain both the modal fields and the complex propagation constant κ. The simulations were carried out for three wavelengths within the

emission spectrum of an NV centre, namely 650 nm, 690 nm and 750 nm. In Figure 4-3, we present the results of the total electric field profile of the supported CPP mode for the 650 nm wavelength.

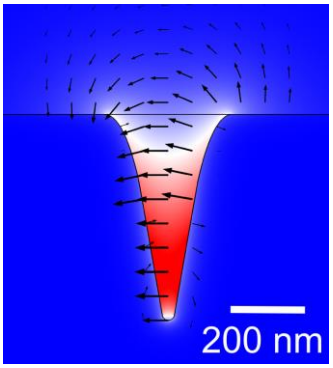

Figure 4-3. CPP mode supported by the VGs. Total electric field profile of the VG-supported CPP mode for 650 nm wavelength.

These simulations confirm that such VG enables sub-diffraction confinement of the EM energy. The electric field lines (black arrows with length proportional to the logarithm of the field intensity at each point) inside the VG show the supported mode is transverse electrically (TE) polarized. The latter will become relevant when considering the orientation of the dipole emitters. From the complex propagation constant κ, the propagation length at each wavelength was determined. We obtained values of 3.4 µm, 4.7 µm and 6.6 µm for the wavelengths of 650 nm, 690 nm and 750 nm respectively. When weighted against the contribution of the NV spectrum at each wavelength we obtained an average weighted value of 4.56 µm.

In a second step, the 3D problem was tackled to determine the optimum parameters for the position of a single QE inside the VG. By implementing a standard procedure for a bare dipole emitter in absence of the diamond host, the Purcell enhancement factor and coupling efficiency to the CPP mode (β-factor) were computed as a function of the position within the symmetry axis of the VG. This was carried out for three orthogonal dipole orientations at the three aforementioned operation wavelengths, and these values were weighted against the NV spectrum to obtain a rough average of the broadband performance of our system (Figure 4-4a).

In the most favourable orientation, namely transversal to the VG axis (*x*-axis in the inset schematic), the β-factor rises up to almost 65%, so the maximum QE-CPP mode coupling is achieved at distances between 200 nm and 300 nm from the VG bottom (black open circles). In this region, the decay rate increases by a factor of 5 as compared to the vacuum decay rate (magenta filled circles). When the QE

approaches the bottom of the VG, although the Purcell enhancement reaches higher values, the coupling is less efficient, as the decay is dominated by ohmic losses.[130,131]

The position range imposed by this VG design makes it challenging to couple certain QEs studied in the field, such as fluorescent molecules and colloidal quantum dots, since intrinsically they can be just within a few nanometers relative to the surface. In this regard, the NV centres in NDs are suitable candidates to fulfil the conditions required for an efficient coupling to the CPP modes supported by these waveguides, as the diamond host acts as a spacer between the NV centre and the metallic surfaces. Assuming the emitter is centred inside a given ND, we could access the region of large β-factor by choosing the proper particle size. Note that this shell spacing also alleviates the typical non-radiative contributions in the QE decay dynamics that arise when these are brought close to the metallic surfaces, which usually results in fluorescence quenching.[130,131]

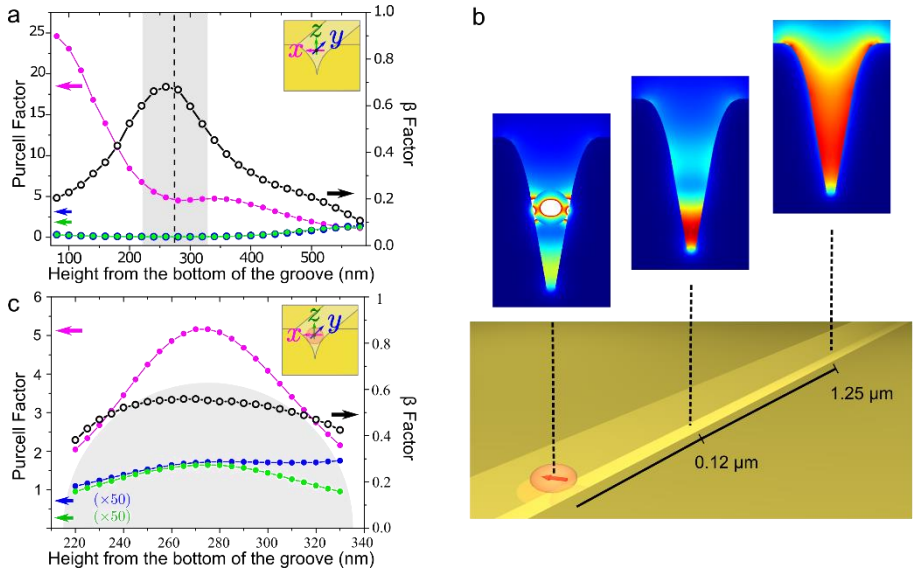

Figure 4-4 Simulations of the single QE-CPP mode coupling. (a) Characterization of the coupling between a bare dipolar emitter and the VG-supported CPP mode as a function of vertical position within the channel. The Purcell factors for the three orthogonal dipole orientations are colour coded as the inset coordinates, while the β-factor is presented only for the dipole aligned with the *x*-axis (black open circles). The β-factor is found to be close to zero for *y* and *z* orientations (data not shown). b) Normalized electric field maps for three different transversal cuts of the VG. The electric field profile resembles that of the VG-supported CPP mode already at 1.25 μm away from the QE (dipole oriented along the *x*-axis). The colour scale has been adjusted in each panel to for a better view. c) Same quantities as in (a), when the dipolar source is located inside a 60-nm-radius diamond ND sphere lying inside the VG. The β-factor is only reduced to 0.56 in this realistic scenario.

To further analyse this hybrid configuration, we considered a 60-nm-radius ND placed inside the VG, lying within the optimum β-factor region depicted by the shaded area, to study the effect of the ND shell on the QE-CPP coupling. The evolution of the field profile along the VG for the QE radiating inside the ND particle (Figure 4-4b) demonstrates that indeed, a QE embedded in such a ND shell can efficiently couple to the guided CPP modes, as the field profile far away from the QE (third panel at 1.25 μm) resembles that of the CPP mode.

To calculate the β-factor, a different method is required as the translational symmetry of the bare VG is broken after the introduction of the ND sphere. The computation scheme is based on the overlap of the transversal fields emitted by the QE and the CPP mode of the empty VG.[127] The influence of both the source orientation and its vertical position within the ND on the Purcell and β-factors was studied for a fixed position of the ND (Figure 4-4c). The presence of the ND shell (represented as the shaded dome) does not affect considerably the results obtained in the case of a bare dipolar source. Indeed, both the Purcell enhancement and the coupling efficiency remain drastically reduced for unfavourable dipole orientations (*y* and *z*-axis). Remarkably, when the QE is oriented along the transversal axis, the coupling of the QE placed at the centre of the ND sphere (dashed line in Figure 4-4a) is almost as efficient as the bare dipole case, since the β-factor is only reduced to 56% (black open circles), while keeping a moderate Purcell factor of 5.2 (magenta filled circles).

These realistic simulations of a QE embedded into a diamond nanosphere, and coupled to the VG-supported CPP mode, unambiguously demonstrate that such hybrid system is promising for quantum plasmonic realizations, as the ND shell does not wear off the efficient QE-CPP coupling and can still maintain a moderate enhancement of the emitter´s decay rate.

4.4 Coupling of multiple NV centres to the channel plasmons

At first, as a proof of concept for the coupling of NV centres to the CPPs supported by the VGs, we recurred to a random positioning approach by simply drop-casting a solution of NDs onto our VG substrates (Figure 4-5a). Considering that statistically some NDs can enter inside the VGs, we could test the coupling of the embedded NV centres by exciting an ND at its position, and looking at the out-scattered light at the VG end mirrors, as illustrated in Figure 4-5b (showing only the guided emission). Figure 4-5c presents a fluorescence map of one of our samples (i.e., excitation and collection from the same positions) where the dashed frame capsules the position of

one VG. We can observe that the NDs are dispersed across the substrate, having some of them lying in line with the VG.

To determine whether the NV centres in these NDs are coupled to the VG modes, we recorded wide-field fluorescence images with the EMCCD camera for a collection polarization transversal and parallel to the VG long axis (Figure 4-5 d&e respectively). These images exhibit a striking difference for the light out-coupled from the VG ends (the dashed scale bar represents the VG length of 10 µm), where only the transversal collection yields a considerable signal at both VG ends. The latter evidences the CPP coupling in our system (recall the TE polarization of this mode from Figure 4-3). We also note some additional out-scattering spots along the VG, which could be associated to either defects or other NDs present along the VG. Nevertheless, their effect is not pronounced, given that a strong fraction of the energy is able to reach both ends of the VG.

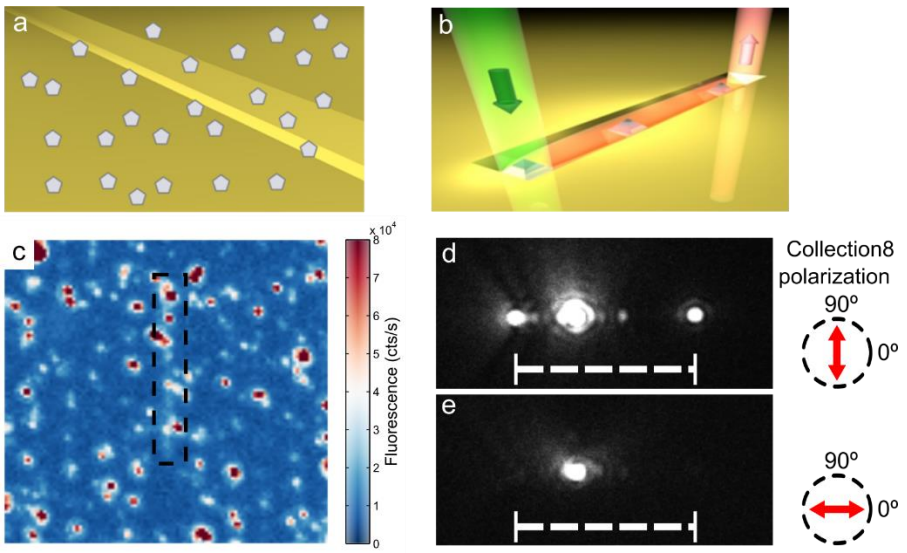

Figure 4-5 Multiple NV-VG devices by random assembly. a) Schematic of the randomnly positioned NDs on a VG chip. b) Schematic illustration of the experiment, showing a VG with several NDs inside the channel. When optically exciting a ND with NVs inside, the emission can couple to the CPP modes, propagate and finally scatter out at the VG end mirror. c) Confocal fluorescence image showing the randomly dispersed NDs surrounding a VG waveguide (dashed frame) d-e) EMCCD images of the hybrid devices upon excitation of one ND. The collection polarization is transversal and parallel to the VG long axis respectively.

PROPAGATION LENGTH OF THE VGS

To extract an approximate value of the VG´s mode propagation length, EMCCD images were recorded while exciting different NDs in nominally equivalent VG structures (Figure 4-6a). The images are unsaturated at the VG end contributions. From these images, we extracted the ratio of intensities between the two out-coupling spots and the relative distance from the nanomirrors to the central excitation spot. In this approach, we assume that the intensity of the CPPs propagating along the VG is described by the following exponential function:

$$I = I_o e^{-\alpha x} \tag{4.1}$$

where I is the measured emission intensity at the nanomirror position, I_o is the emission coupled into the CPP mode by the emitters (in one direction), $\alpha = 1/L_{\mathrm{pl}}$, with L_{pl} the propagation length of the CPP mode supported by the VG, and x is the distance between the nanomirror and the ND. We assume symmetric coupling to both forward and backward directions, the losses to be uniform along the waveguide, and the out-coupling efficiency of both nanomirrors to be equivalent. From this equation, a simple expression is derived to relate the intensities and relative distances as follows:

$$x_{\mathrm{l}} - x_{\mathrm{r}} = L_{\mathrm{pl}} \ln\left(\frac{I_{\mathrm{r}}}{I_{\mathrm{l}}}\right) \tag{4.2}$$

with the subscripts referring to the intensities and distances for the left and right out-coupling spots with respect to the central confocal spot. The results are plotted in Figure 4-6b, and the fit to Eq. 4.2 leads to a propagation length value of 4.65 um ± 0.48 μm. This value is in good agreement with the simulations of the intrinsic propagation length, where we extracted a weighted value of 4.56 μm.

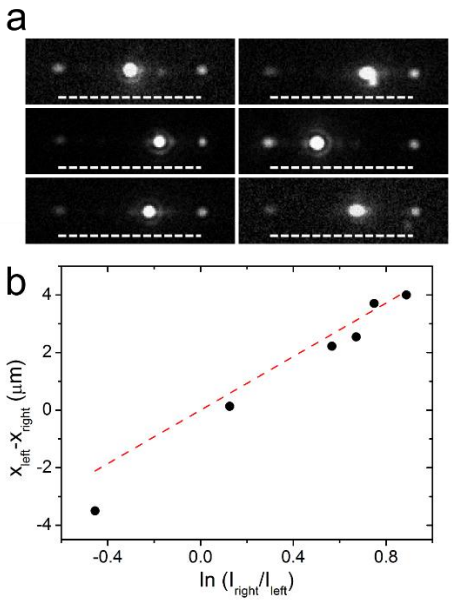

Figure 4-6 Propagation length estimation. a) Wide-field fluorescence EMCCD images from NDs containing multiple NV centres coupled to the CPPs supported by the VGs. The dashed scale bar is 10 µm. b) Experimental data extracted from a), with the red dashed curve being a linear fit to equation (2). We obtain a propagation length value of 4.65 um ± 0.48 µm.

DISTINCTION BETWEEN THE COUPLED AND UN-COUPLED NVS

By measuring the fluorescence lifetime from the different out-coupling spots in our VGs (i.e., directly from the ND and from the VG ends), we observed differences in the extracted lifetime values. Figure 4-7 presents two examples from NDs within the same device. The wide-field images for the transversal polarization in Figure 4-7a&b show the emission directly into free-space, as well as the CPP-coupled emission out-scattered at the VG ends (the SEM images serve a guide to the eye). The lifetime measurements for the signal collected from the excitation position (black) and from one VG end (magenta) are presented in Figure 4-7c&d. In both cases, shorter (faster) lifetimes were extracted for the case of the guided emission, with a reduction factor of 0.7 and 0.66 respectively. Next, we provide arguments to explain the observation of different lifetimes despite the fact we are exciting the same particle.

As we learned from the theory simulations, only the NV centres that are at the right positions within the VG, and oriented along the transversal axis of the channel, will efficiently couple a fraction of their emission into the waveguide modes, thus experiencing an enhancement in the decay rate (faster fluorescence lifetime). For the case of multiple NV-NDs, we can assume that there will be a distribution of positions and dipole orientations within the particle, meaning that some NVs will couple better than others when placed inside a VG. This basic picture can help us understand our

findings, where, in our case, the emission collected directly from the particle (confocal collection) will have stronger contributions from the un-coupled NVs, while the emission collected from the VG ends will have contributions mainly from the coupled NVs. In this context, it is reasonable that the emission collected from the VG ends exhibits shorter lifetime values, since this signal corresponds to emitters that experience an additional decay channel to its total decay rate.

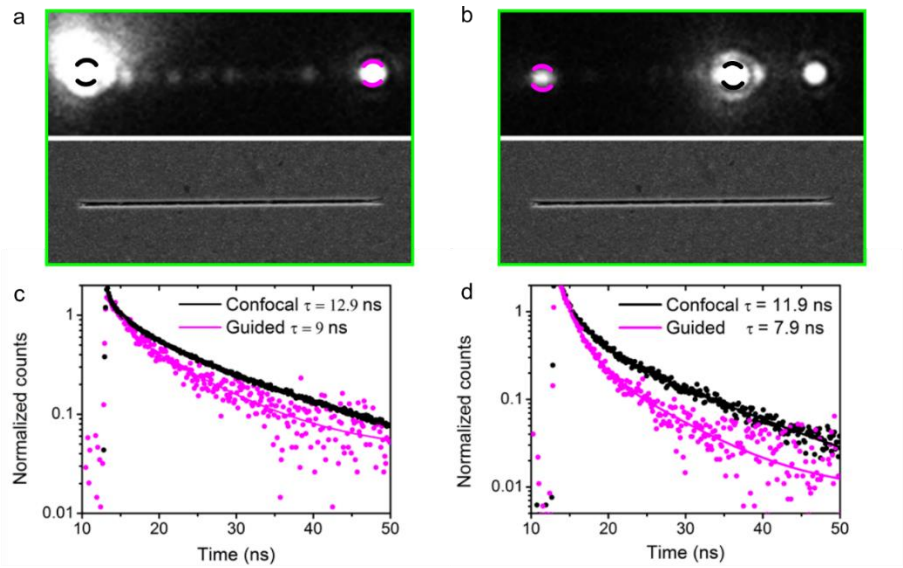

Figure 4-7. Lifetime measurements of multiple NV-NDs inside the VGs. a-b) EMCCD images (top) for the transversal polarization collection for two NDs inside a VG device, where the SEM images (bottom) help to associate the relative positions of the out-coupled spots. c-d) Lifetime measurements for the two devices, when the signal is collected from the excitation point (black traces) and from the VG end circled in the EMCCD images (magenta traces).

A more rigorous model would have to account for all the multiple NV lifetime contributions, however that would complicate the analysis of the lifetime curves, and here we assume that the measured decay rates correspond to an average of either the coupled or un-coupled NVs depending on the collection position.

4.5 Coupling of a single NV centre to the channel plasmons

To assemble and study a single NV-VG device, we can no longer rely on the random assembly, since in ND solutions there is a large probability of finding none or multiple NVs, with only a small fraction of the particles actually embedding a single NV centre. In this regard, we exploited the dual positioning approach to first locate an ND embedding a single NV with bright and stable emission, and then

assemble a hybrid quantum plasmonic device in a truly deterministic fashion via the AFM manipulation technique.

First, ND arrays were positioned in the vicinity of our VGs by implementing the EBL lithography and electrostatic self-assembly steps described in Section 4.2.3. Figure 4-8 shows confocal fluorescence microscopy images of four VG devices with the surrounding ND arrays on one side of the waveguides (here labelled as D1-D4). The VG profile is easily spotted due to the enhanced Au auto-fluorescence. As seen later, these contributions can be suppressed when exciting the structures with light polarized parallel to the VG long axis.

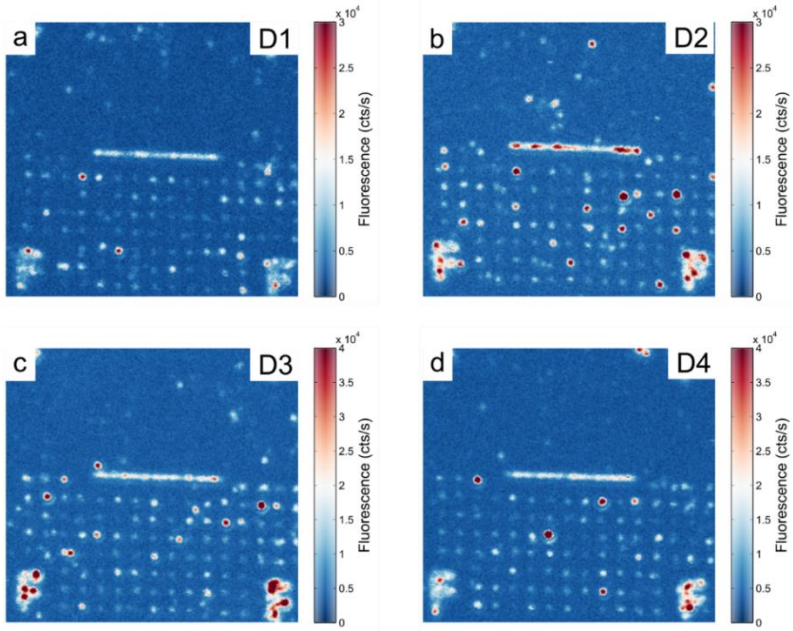

Figure 4-8. Arrays of NDs patterned in the vicinity of the VGs. a-d) Confocal fluorescence scans of four VG devices with surrounding ND arrays positioned by previously masking the substrate with an EBL hole mask. As scale reference, the spacing between NDs is 1.5 µm.

IDENTIFYING THE SINGLE NV CENTRES

We implemented a Hanbury-Brown-Twiss (HBT) detection scheme[132] to identify the fluorescent NDs hosting a single NV centre. It is important to underline that this strategy guarantees the quantum nature of the plasmonic device, since the CPPs are launched one by one by this single emitter source. Figure 4-9 shows the anti-bunching measurements from five of the NDs surrounding device D1 in Figure 4-8a. With the exception of the ND-3, these NDs exhibited dips in the coincidence measurements characteristic of a single emitter ($g^2(t=0)<0.5$).

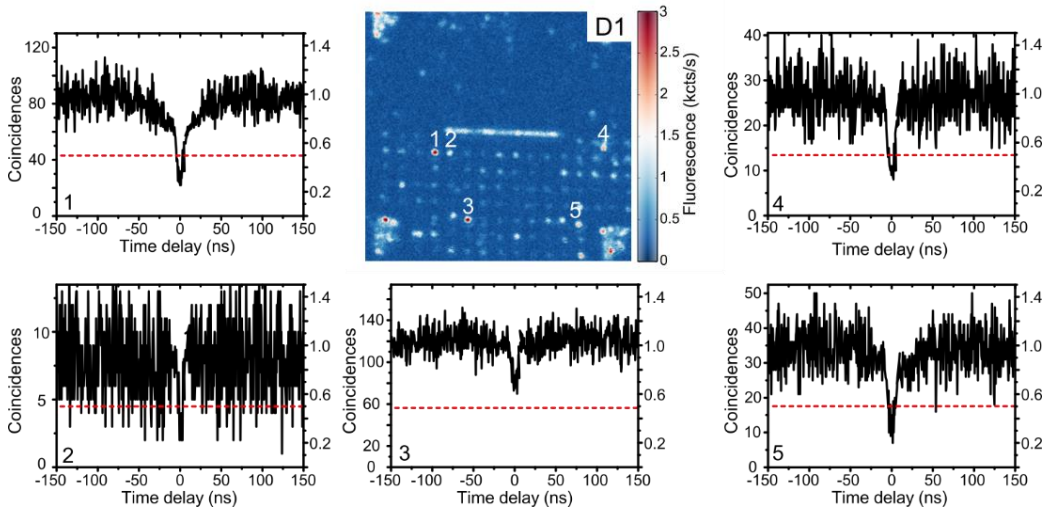

Figure 4-9 Identifying NDs with single NV centres. A selection of autocorrelation measurements from five nanodiamonds near our device D1. Antibunching dips below 0.5 at t=0 confirm the single emitter characteristic (NDs labelled 1, 2, 4 & 5).

DETERMINISTIC ASSEMBLY OF THE NANODIAMOND

In the second step, we used an AFM in tapping mode for visualization, and in contact mode[102,126] to move selected NDs across the Au film and finally into the VG. Figure 4-10a shows an AFM image of device D1 prior to the movements, where the red circle corresponds to our ND selection (labelled ND-1 in Figure 4-9). First, the ND is relocated to a position alongside the VG and we double-check in the confocal setup whether the right movement was made (Figure 4-10b). As it can be observed, the bright spot is missing from the array (dashed circle) and is now alongside the VG (solid circle). We measured the fluorescence lifetime of the NV, before and after this initial movement, and obtained values of 23.9 ns and 25.9 ns respectively. The acquisition of similar lifetime values demonstrates the stability of emission properties of the chosen NV centre after translation of the particle across the Au surface, suggesting the emitter is well centred inside the nanoparticle. If the NV centre would be closer to the surface, it will likely exhibit pronounced changes in the lifetime values due to variations in the distance between the emitter and the metallic surface.

Finally, the AFM movements were repeated to bring the ND inside the VG. The confocal image of the final device configuration is presented in Figure 4-10c, where thanks to the parallel polarization in excitation, we could supress the VG auto-fluorescence and confirm the presence of the NV centre inside the VG. The AFM inset image clearly shows the ND is within the VG´s transversal axis. Additionally, a

lifetime reduction to 10.6 ns was observed, most likely due to the additional decay channel provided by the CPP mode supported by the VG.

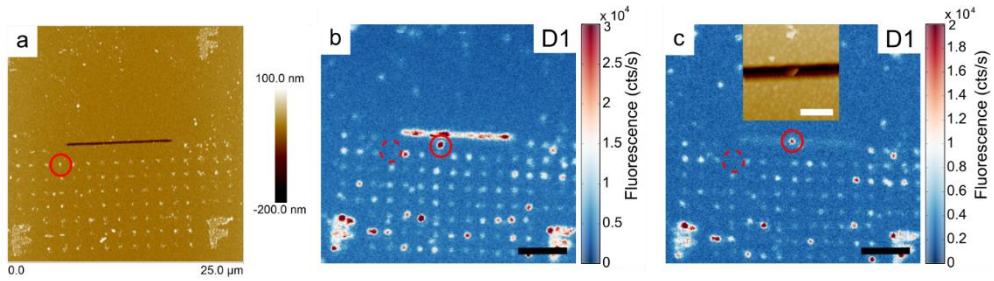

Figure 4-10. Deterministic assembly into the VG. (a)-(c) Confocal images showing the sequence of steps in AFM mediated positioning of a ND containing a single NV centre. (d) AFM image of device D1 at the same stage as (a). (e) AFM image of the ND inside the VG. (f) Lifetime measurements of the NV centre at each stage, showing a lifetime reduction only when inside the VG.

PURCELL FACTORS

To estimate an experimental Purcell factor, we did not rely on the measurement performed with the same emitter on the Au film, since the latter can support surface plasmon polaritons that can contribute to the measured lifetime. Instead, the value measured inside the VG was compared to the average of the lifetime distribution measured on single NV centres from the same solution deposited on a glass substrate (Section 2.3.2, τ=24.2 ± 7.2 ns). From this, we obtained an experimental Purcell factor of 2.3 ± 0.7. The distribution on glass is consistent with other reports on similar sized NDs. The longer lifetime as compared to a NV centre in bulk diamond (~11.6 ns) is typically attributed to the reduction in the radiative emission rate caused by the variation in effective refractive index of the surrounding medium for emitters embedded in nanoparticles smaller than the emission wavelength.[76,133]

To compare the experimental Purcell factor to theoretical simulations, we calculated the lifetime distribution associated with an isolated ND when considering an ensemble of particle sizes (40 nm-80 nm radii). This distribution was used to normalize the Purcell factors presented in Figure 4-4c. For the 60-nm-radius ND with the NV centre aligned to the transversal axis of the VG, we obtain a modest Purcell factor of 3.0 ± 0.6, while for the other orthogonal orientations we get a negligible value. This result is consistent with our experimental value.

CPP COUPLING EVIDENCE FROM THE HYBRID SINGLE NV-VG DEVICE

To unambiguously demonstrate the ability of this quantum plasmonic device to couple the NV centre emission to the CPP mode supported by the VG, we imaged our device with the EMCCD camera while exciting the NV centre, and observed

coupling of its emission to the waveguide modes. As a guide to the eye, Figure 4-11a shows an image under wide-field illumination to appreciate the contour of the VG due to the enhanced auto-fluorescence of the structure with respect to the plain Au film.[134] The polarization dependence of the out-coupled spots at the VG ends seen while exciting the NV, was evidenced by the wide-field collection fluorescence images for four combinations of excitation and collection polarizations (i.e., combining polarizations parallel and transversal to VG axis as labelled in Figure 4-11b-e). Figure 4-11f shows line cuts along the VG to help visualizing the different contributions in the EMCCD images.

First, we note stronger signals from the confocal spots when the excitation is transversal to the VG long axis (Figure 4-11b-c), which was expected from our confocal scans (Figure 4-10), and can be attributed to the enhanced Au auto-fluorescence arising from either the rough Au edges or from the gap and wedge plasmons supported by the VG. On the other hand, we observe out-coupling spots at the VG ends only for the transversal polarization in collection (Figure 4-11b-c). Additional outcoupling spots along the VGs are also appreciated only for the transversal polarization, which we associate to defects along the VG that can scatter out a fraction of the emission traveling along the VG (as observed already in the previous section with the multiple NVs). These observations demonstrate the coupling of the single NV centre emission to the CPP mode, clearly elucidating the TE polarized nature of the propagating CPP mode.

On the line-cuts associated to Figure 4-11b-c, the two out-coupling spots at the ends of the VG do not exhibit significant differences, suggesting the Au auto-fluorescence, which is higher for the confocal spot under transversal excitation, does not couple significantly to the CPP modes responsible for the emission observed at the VG ends. The main reason why the Au auto-fluorescence is not able to couple to the CPP mode is that its fluorescence is generated at the surface of the VG walls, and thus not fulfilling the position requirements for efficient coupling as shown in Figure 4-4.

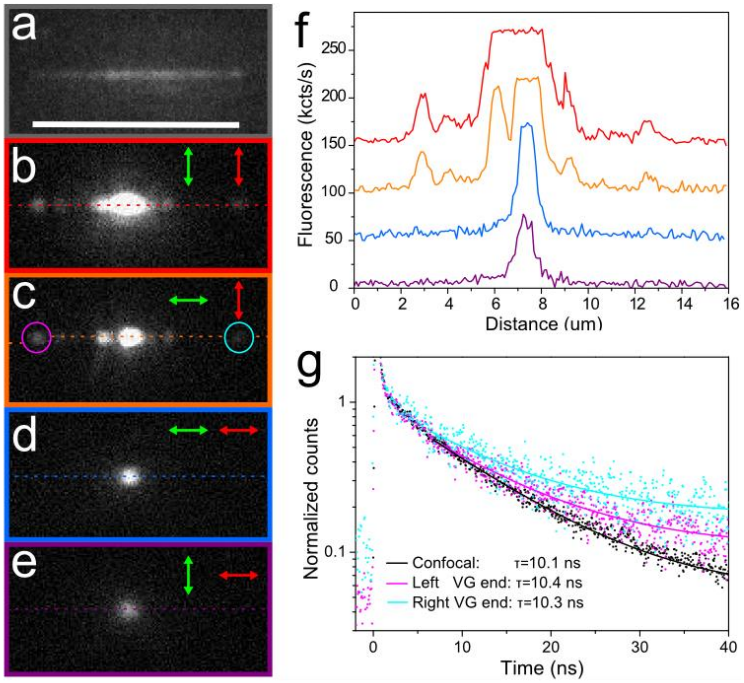

Figure 4-11. Emission coupling from a single NV centre to CPPs in a VG. a)-e) Wide field collection fluorescence microscopy images of an assembled NV-VG device. (a) Upon wide-field illumination, the VG contour is appreciated due to the enhanced Au auto-fluorescence at the VG location. b-c) Collection polarization (red arrow) set transversal to the VG axis evidences the guided emission out-coupled from the VG ends. The excitation polarization (green arrow) was set transversal (b) and parallel (c) to the VG axis, respectively. d-e) Collection polarization set parallel to the VG axis. Only emission coming directly from the excited NV centre is observed for both parallel (d) and transversal (e) excitation polarizations. f) Fluorescence intensity along the dashed line in (b)-(e) (same colour code as the frames). g) Lifetime measurements for the polarization configuration of (c) at three collection locations. Direct collection (black) and emission out-coupled from the left (magenta) and right (cyan) VG ends. Independent lifetime values confirm that the guided emission corresponds to that of the single NV centre coupling to CPPs.

We also performed lifetime measurements under pulsed excitation at three different collection positions while fixing the excitation point at the NV centre for the case of parallel excitation and transversal collection (Figure 4-11c). From the confocal spot (black dots) and from the left and right VG extremities (magenta and cyan dots, respectively) we extract consistent values for the emitter´s lifetime (τ~10.3 ns). These measurements confirm that the emission collected from the VG ends correspond to a fraction of the emission from the single NV centre. Note that the lifetime is associated to the total decay rate of an emitter, and thus for a single emitter it is expected to be independent of the collection channel (in contrast to the observations made with the multiple NV centres).

The coupling efficiency (β-factor) of the hybrid system is defined as the ratio between the decay rate into the CPP mode and the total decay rate of the QE. It is not

possible to measure separately the lifetimes associated to the different decay rates of a QE. Instead, we can estimate the experimental β-factor by computing the ratio between the intensities of the out-coupling spots associated with CPP coupled emission (VG ends and other spots along the VG), and the sum of all the out-coupling spots, including the confocal spot. To do so, we analysed the intensity counts from non-saturated images taken in absence of a polarizer in the collection channel. Accounting for the propagation losses (Figure 4-6), we obtained a β-factor of 0.42 ± 0.03. This value is in good agreement with the expected value of 0.56 extracted from the simulations. The small deviation from the optimum value is reasonable considering that the position and/or orientation of the NV centre are not necessarily ideal in the experiment.

4.6 Conclusions and Outlook

We have demonstrated a platform to integrate single quantum emitters with plasmonic waveguides compatible with lithography designed circuits. Our system consists of NV centres in diamond nanoparticles, integrated into VG plasmonic waveguide channels. Theoretical simulations have shed light on the importance of controlling the position and dipole orientation of a QE inside such a plasmonic waveguide. In contrast to using metallic nanowires, where the optimal distance between a QE and the metallic surface for efficient coupling is in the order of 10 nm,[20,38,135] these VG waveguides appear favourable to QEs located at distances in the order of 50 nm away from the metallic surfaces. This opens the possibility to enhance the Purcell factor far away from the metallic surfaces while minimizing the non-radiative decay rate contributions. We find that a single emitter embedded inside a 60 nm radii ND can couple up to 56% of its emission into the CPP modes supported by a VG waveguide, with a modest Purcell factor of 5.2.

Experimentally, devices with NDs embedding multiple and single NV centres were studied. The former, by randomly positioning the particles, and the latter, by employing deterministic positioning methods to bring a single particle inside the channels. In both cases, we observed coupling of the emitters to the CPPs supported by the VGs, revealed by the polarization dependent analysis of the out-coupled contributions along the VGs. From the multiple NV coupling, we could extract an experimental propagation length of our VGs of 4.65 μm ± 0.48 μm, in close agreement to the simulated value of 4.56 μm. The VG configuration also allowed us to differentiate between the total decay rates of the coupled and uncoupled emitters by means of lifetime measurements from the different out-coupling signals.

From the single NV study, we determined a β -factor of 0.42 ± 0.03 and a Purcell factor of 2.3 ± 0.7 for our hybrid system. The accordance between the experimental

results and the simulated values for the ideal NV orientation, suggests that the ND positioned inside the VG hosts a NV centre aligned not far from the transversal axis of the VG.

Our hybrid system stands well among previously demonstrated platforms of single QEs coupled to plasmonic waveguides. For example, they are comparable to those reported by Akimov *et al* for the coupling of a single QD to a silver colloidal nanowire (β-factor of 0.6 and a Purcell factor of 2.5).[20] Very recently, during the course of this thesis, Kress *et al* reported remarkable values for a single QD printed at the tip of a silver wedge plasmon waveguide (β -factor of 0.7 and a Purcell factors in the order of 20-fold).[42]

In the future, similar hybrid systems can be assembled and characterized thanks to the combined methods presented here. To improve the efficiency of the device, near-infrared single photon sources such as silicon vacancy centres in ND could be used.[136] One should also aim to improve the coupling efficiency by controlling the NV dipole orientation with respect to the CPP mode field lines (transversal to the VG axis), for example by implementing optical trapping techniques that allow for particle orientation control.[98] Additionally, VGs can specifically be designed (and fabricated) to contain smoothly connected sections with different VG profiles, in order to enhance the NV-CPP coupling at a very narrow VG section with extremely tight mode confinement,[57] while preserving large CPP propagation lengths at wider VG sections.[53]

Other potential steps to follow might be to develop an integrated quantum plasmonic function based on this hybrid system. For instance, an on-chip optical transistor or a Mach-Zender plasmonic waveguide interferometer could be realized with such on-chip single photon source. Assembling multiple single emitters within the same device can also be pursued, in order to study the potential plasmon mediated interactions between particles.[15]

Chapter 5 Quantum dots in nanowires coupled to plasmonic waveguide modes

Self-assembled quantum dots (QDs) represent a powerful platform to realize novel quantum information applications, both in free-space and on-chip technologies. In particular, semiconductor nanowires (NWs) embedding such quantum emitters are among the most promising platforms for on-chip technologies, given the versatility of integrating different elements within a single NW heterostructure. Interfacing these structures within a photonic circuit is of paramount importance in order to achieve on-chip applications. In this chapter, we utilize recently developed semiconductor NWs that embed QDs near the edge of the nanowires. By using micro and nano-manipulation techniques, individual NWs with varying QD densities were assembled at the bottom of V-groove plasmonic waveguides. We then demonstrate coupling of the emission from the emitters to the channel plasmon polaritons supported by our plasmon waveguides, down to the single emitter case.

5.1 On-chip integration of QD-NWs for photonic applications

As introduced in Chapter 2, different types of self-assembled quantum dots (QDs) can be grown by epitaxial deposition methods, with the Stranski-Krastanow method being the most popular to grow QDs in planar substrates. This type of QDs have been extensively studied and have led to the demonstration of single photon sources as well as laser devices.[69] However, due to the high refractive index mismatch between the embedding matrix and the surrounding medium, the photon extraction is highly inefficient. The latter can be improved by engineering the QD environment, for example incorporating distributed Bragg reflectors[137] or embedding the emitter within post-processed microcavities[138] and photonic nanopilars.[139]

Over the last decade, the bottom-up integration of self-assembled QDs in one-dimensional nanowires (NWs) has offered a solution for the photon extraction efficiency thanks to the improved performance of the QDs and the waveguiding properties of the NWs.[72,140] Furthermore, the NW geometry can be designed to achieve highly efficient photon extraction by engineering the tapers at the NW tips, and also by integrating them with back-end reflective mirrors.[72] Several groups have shown that individual QDs in NWs can operate as highly efficient and bright single photon sources,[72] or to provide strongly entangled photon pairs, making them very promising for quantum communications applications.

So far, the best collection efficiencies from QD-NWs have been achieved from the vertical standing structures. On the other hand, having the NWs in a horizontal configuration enables facile integration of electrical contacts,[141] making them very promising for on-chip applications. To fully exploit this potential, one needs to integrate the NWs with elements that can efficiently extract and route the QD emission within the surface of a chip, for example with on-chip waveguides.[142]

In the previous chapter, we showed that VG plasmonic waveguides represent a good platform to couple the emission from a single quantum emitter to on-chip propagating modes.[143] In this context, here we explore the coupling of QD-NWs to the propagating channel plasmon polariton (CPP) modes supported by VG plasmonic waveguides. To achieve this, NWs embedding a new type of self-assembled QDs are combined with Si-etched based VG plasmonic waveguides. To assemble the hybrid devices, we used micro and nano-manipulations techniques to precisely position the NWs inside the VG channels. We show results for NWs embedding high and low QD densities, demonstrating coupling of the emission down to a single QD.

The hybrid photonic platform is schematically illustrated in Figure 5-1, were ideally one excites an individual QD in such hybrid system by means of a focused laser beam, and the emitted single quanta can couple to the propagating modes of the

VG channel. In this scenario, the guided plasmons can scatter out to free-space modes at the VG end mirrors.

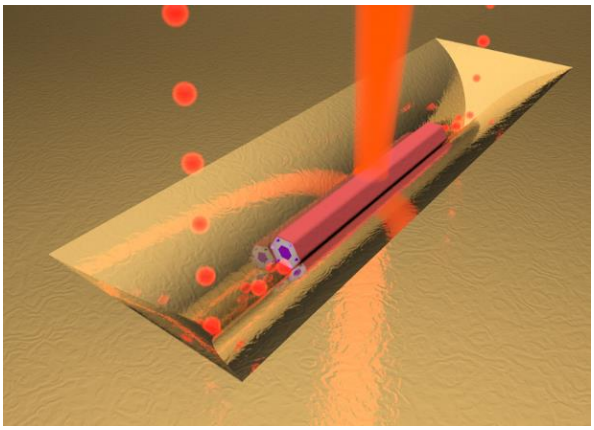

Figure 5-1. QDNW-VG platform. Schematic illustration of a NW with self-assembled QDs integrated inside a V-groove plasmonic waveguide. Upon excitation with a focused laser, a QD embedded inside a NW, can couple its emission to the VG-supported plasmon modes. The single quanta can propagate along the waveguide and in this case, scatter out to free-space at the VG end mirrors.

5.2 Materials and Methods

5.2.1 QDs self-assembled at the apex of NWs

The NWs implemented in this chapter were fabricated by Gözde Tütüncüoglu in the group of Prof. Anna Fontcuberta i Morral at the EPFL in Switzerland. The NW growth was carried out in a high mobility grade molecular beam epitaxy machine (MBE, DCA P600). The GaAs core of the NWs was obtained by the Ga-assisted method on (111) silicon wafers. After the core reached a length of 10 µm, the Ga flux was interrupted and the As_4 flux increased, resulting in the axial growth stop. The substrate temperature was then decreased in order to grow a high quality epitaxial $Al_xGa_{1-x}As$ shell (33% Al content ratio). The structure was terminated with a GaAs capping layer of 5 nm to prevent oxidation of the inner layers. The QD islands typically form near the edge of the apex of the AlGaAs layer, while the thickness of this shell determines the size (emission energy) and density of the QDs.[73,75,144] In this chapter, we carried out experiments with NWs having high and low QD densities.

5.2.2 Si-etched based V-groove plasmonic waveguides

The VG structures used in this chapter were developed by Cameron L.C. Smith at the Technical University of Denmark (DTU).[56] First, a silicon substrate with a 200

nm SiO_2 layer is patterned by both UV-lithography and reactive ion etching to define the perimeter of the VG structures (initial width of 3.5 μm and varying lengths). The VG and termination mirrors are formed by anisotropic wet etching of the exposed silicon in a potassium hydroxide (KOH) bath at 80 °C. The KOH etch yields smooth ⟨111⟩ VG sidewalls and termination mirrors with a 55° fixed inclination from the surface plane. The remaining SiO_2 is removed by etching in a hydrofluoric (HF) acid bath. Tailoring the V-shape geometry is performed by thermal wet oxidation of the silicon VGs at 1150 °C for 9 h, resulting in a 2320 nm thick SiO_2 layer at flat sections of the substrate. The VG widths are approximately 3.2 μm after the thermal oxidation step. A 70 nm Au film is then deposited by electron beam evaporation with an initial 5 nm layer of chromium to promote adhesion of the Au to the SiO_2 surface. The Au layer is chosen sufficiently thick to eliminate the interaction of air−interface plasmons with the SiO_2 layer, and also to minimize aggregation. Here, we use 2.5 μm wide VGs with varying lengths.

5.2.3 Transfer and positioning of single NWs

We transferred the NWs from the as-grown substrate to the VG chip by using a dry-transfer technique. The technique involves swiping the tip of a cleanroom tissue (Berkshire) over the NW sample, which breaks the NWs from their original substrate and causes some to attach to the tissue. The tissue is then swiped across the sample containing the VG structures causing a number of NWs to detach from the tissue and spread across the surface lying down in a horizontal position.

The optical microscope image in Figure 5-2a shows a VG array area with transferred NWs. For the coarse movements across the substrate and towards the edge of the VGs, we used a pulled optical fibre tip mounted on a micromanipulator stage attached to an optical microscope. By using a long working distance objective (Olympus LMPLFLM50x), the NW movements could be monitored in real-time (Figure 5-2b-i). The high aspect ratio of these NWs makes them easy to bend and brake apart upon manipulation (Figure 5-2c-d shows the bending of a NW and subsequent breakage). Once the NW fragments have lengths roughly below 10 μm, they are rigid enough to move without further breaking (Figure 5-2d-i). During the micromanipulation step, we only place the NWs until the border edge of the VGs (see Figure 5-2j corresponding to the device shown in Figure 5-2i).

To move the NWs towards the bottom of the channels we implemented the AFM nanomanipulation technique. One drawback encountered with this technique was that occasionally, NWs were lost due to their attachment to the AFM tip during the fine positioning at the VG bottom (this was the case with the device shown in Figure 5-2j). Instead, we show here an SEM image of another device where we successfully placed

the NW at the bottom of the VG. The SEM images in Figure 5-2k-l clearly show that the NW is well centred across the symmetry axis of the VG, demonstrating the accurate positioning of our approach.

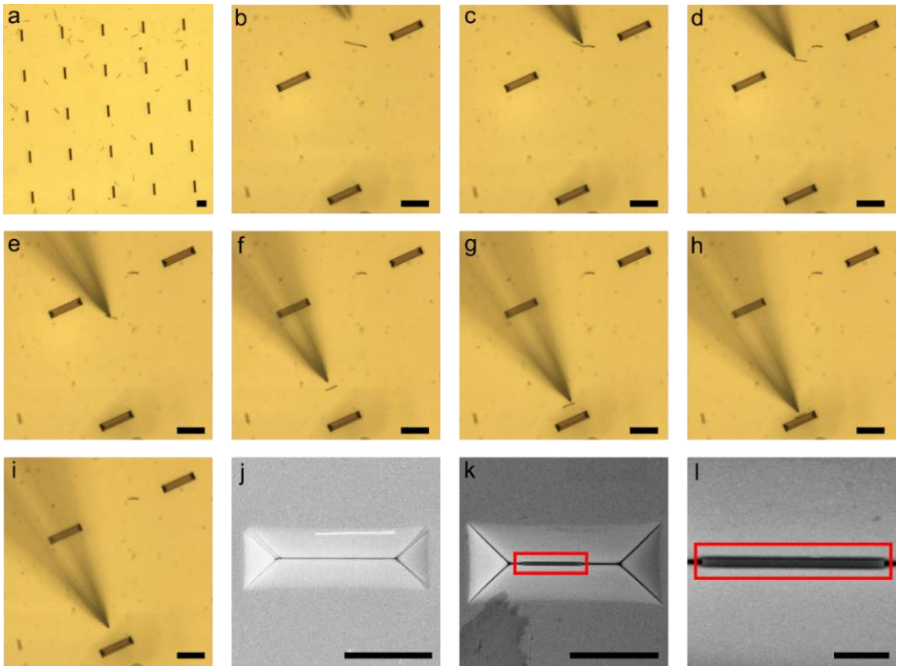

Figure 5-2 Assembly of QD-NWs into VG waveguides. a) Optical microscope image of a VG array with randomly dispersed NWs. b-i) Micromanipulation sequence of a single NW across the surface of a chip. In c-d) we witness the bending and braking apart of a NW. In e-i) the NW segment is rigid enough to bring it alongside the VG. j) SEM image of the NW placed at the border edge of a 15 µm long VG. k) SEM image of an assembled 7.8 µm long NW inside a 10 µm VG. l) Zoomed in SEM image showing the excellent symmetric alignment of this hybrid NW-VG device. All the scale bars represent 5 µm.

5.2.4 Experimental Setup

To optically characterize our hybrid devices, we implemented a homemade photoluminescence optical microscope. A continuous wave (CW) He-Ne laser at 633 nm was used for the optical excitation. The substrates were mounted on a 3-axis piezoelectric stage inside a helium cryostat kept at 12 K during the experiments. A linear polarizer and a quarter-wave plate in the excitation channel allowed us to excite the QDs with circularly polarized light. In some cases, we introduced a cylindrical lens to fully excite the NWs at once. The emission was collected through the same objective. A 650 nm long-pass filter blocked the excitation contributions, and a linear polarizer allowed us to perform polarization dependent collection analysis. The emission was then split into two channels using a 50:50 beam splitter. On one channel

the emission was focused into a CCD camera (Hamamatsu), providing us with a wide-field view of the emission at the sample plane. On the second channel, the emission was focused into a single-mode optical fibre which was coupled either to a pair of avalanche photodiodes (APDs) for lifetime and correlation measurements, or to a spectrometer for spectral analysis. By steering a mirror in the detection channel, we could selectively collect the emission into the fibre from different areas within our field of view, allowing us to independently collect the emission from different points along the NW-VG device.

5.3 Coupling of the NW self-assembled QDs to the VG supported modes

The low temperature experiments presented in this chapter were performed together with Luca Francaviglia at the laboratory of Prof. Anna Fontcuberta i Morral at the EPFL in Lausanne, Switzerland.

5.3.1 Nanowires with high density of self-assembled quantum dots

First, we investigated NWs with a high density of QDs (i.e., a 100 nm thick AlGaAs shell). Figure 5-3 shows the results for a NW-VG device when exciting the full 7.8 μm long NW segment inside a 20 μm long VG. We recorded wide-field fluorescence images with the CCD camera for a collection polarization parallel (left) and transversal (right) to the VG long axis (Figure 5-3a). An SEM image of the device taken after the experiments is also shown to help associate the out-scattered contributions to the relative position along the device. We observed emission not only from the full NW body, but also from the two VG ends, with a stronger signal for the transversal collection, evidencing the coupling of the emitters to the CPPs supported by the VG.

By steering a mirror in the detection channel, we performed position selective spectroscopy of the QDs emission contributions along the hybrid device. Here, we show the spectra for a polarization parallel (black) and transversal (red) to the VG long axis, collected from the upper VG and NW ends (Figure 5-3b&c respectively), the central section of the NW (Figure 5-3d), and from the lower NW and VG ends (Figure 5-3e&f respectively).

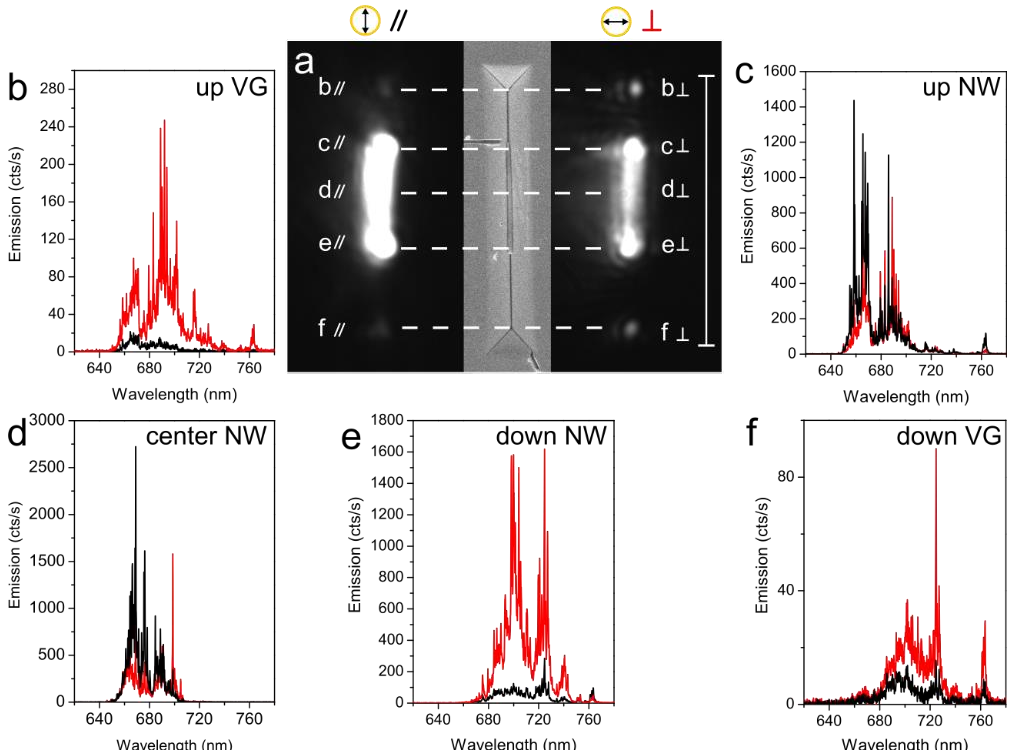

Figure 5-3 Coupling of multiple QDs in a NW-VG device excited with an elliptical spot. a) CCD images for two orthogonal polarizations (parallel and transversal to VG long axis), with the corresponding SEM image of the device. The NW segment is 7.8 µm long while the VG waveguide is 20 µm long. b-f) Photoluminescence spectra for the transversal (red) and parallel (black) polarizations with respect to the VG long axis, collected from different positions along the device.

From the spectra collected at the VG ends (Figure 5-3b&f), we observe that the contributions for the transversal polarization collection (red) are stronger than for the parallel polarization (black), consistent with the CCD images. This is direct evidence that indeed, multiple QDs within the NW are able to couple part of their emission into the CPP modes supported by the VG. Note that there is no particular preference in polarization for the emission collected from three points along the NW (Figure 5-3c-e).

We also noticed that the spectral contributions of the QDs located at the lower NW end (Figure 5-3e), were red-shifted compared to those from the upper NW end (Figure 5-3c). This can be associated with the presence of larger QDs (lower emission energies) in the lower part of the NWs. This is reasonable given that the NW is thicker at the lower end (SEM image in Figure 5-3a). This is a signature that the AlGaAs shell grew thicker on that end, which favours the aggregation of larger QD islands.[75]

CONFOCAL EXCITATION OF THE QDS

Next, we removed the cylindrical lens and performed confocal measurements (i.e., excitation and collection from the same position on the NW). Figure 5-4a presents SEM images of our device, with the inset image offering a detailed view of the NW. The positioning is excellent within the VG symmetry axis, and the result of small tapering in thickness can be appreciated (i.e., larger diameter at the lower NW end). We acquired CCD images for both transversal and parallel polarizations (Figure 5-4b) at the five positions roughly corresponding to those labelled in the SEM image (the 20 μm scale bar is representative of the VG length). Again, the CPP coupling is revealed by the out-scattered signals from the two VG ends, which are brighter for the transversal polarization.

The emission spectra collected from each of the five excitation points is presented in Figure 5-4c&d, for the parallel (black) and transversal (red) polarizations respectively. Here, we confirm the previous observations that the thicker NW segments exhibit QDs with lower emission energies (the blue dashed line depicts the wavelength shift).

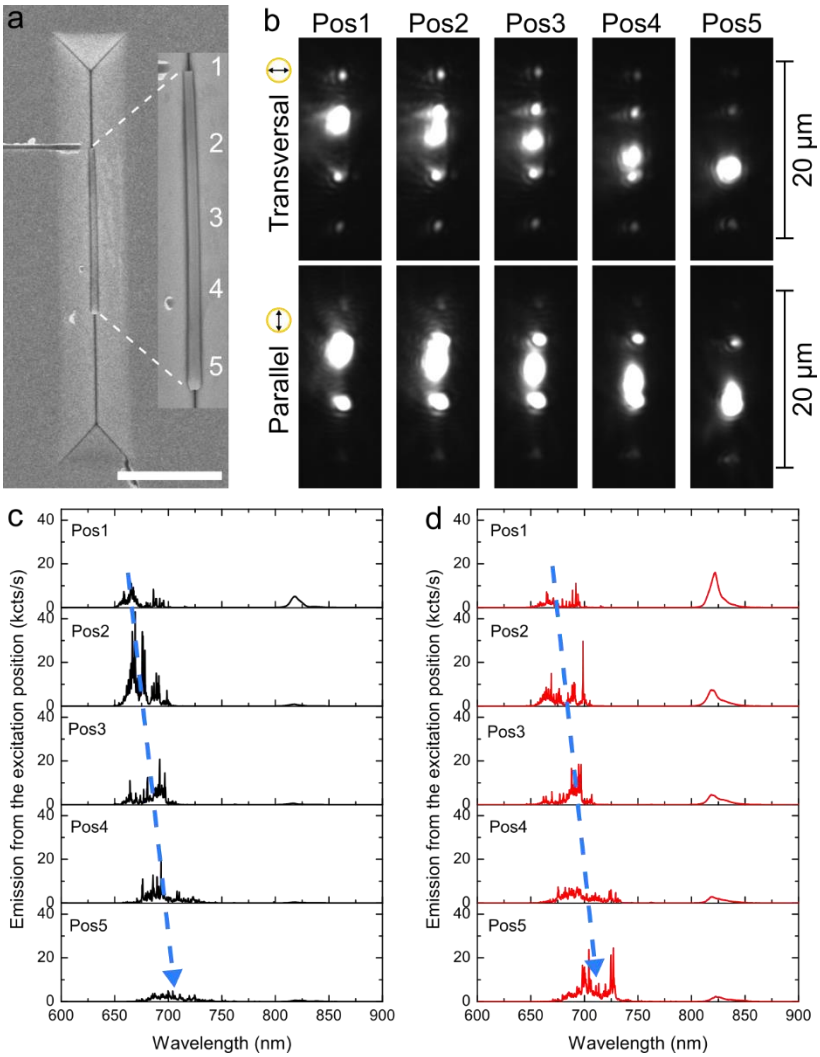

Figure 5-4 Confocal measurements of the QDs along the NW. a) SEM images of the hybrid QDNW-VG device. The NW is 7.8 µm long and 290 ± 25 nm in diameter, while the VG is 20 µm long. Scale bar is 5 µm. The zoomed inset shows the excellent positioning within the VG. b) CCD images of the emission intensity from the hybrid devices upon confocal excitation at five positions corresponding to those labelled in (a). The top and bottom images correspond to the collection polarization transversal and parallel to the VG long axis respectively. c-d) Emission spectra collected from the excitation positions for the parallel and transversal polarization collection respectively. The spectra evidences the QD energy shift due to tapering of the AlGaAs shell within the NW.

COUPLING OF FEW QDS TO THE VG MODES

Under the excitation conditions in Figure 5-3 & Figure 5-4, many QDs are likely excited, making it difficult to isolate the contributions from individual emitters. To minimize the number of QDs excited by the focused spot, the excitation power was

lowered while the excitation spot was moved towards the upper NW end (i.e., only a few QDs overlapping with the excitation spot). Figure 5-5 shows the emission spectra at two positions near the upper NW end for the transversal polarization collection. The red spectra correspond to the coupled emission contribution collected from the upper VG end, while the black spectra correspond to the emission collected directly from the excitation point. The insets are the corresponding CCD images.

As can be observed in the spectra, under these excitation conditions, single emission peaks become visible. Interestingly, at both positions we can distinguish that some of the QD lines (marked by black arrows) present in the confocal collection (black traces) are either missing or exhibit lower relative intensities in the guided contributions (red traces). As described earlier, these QDs can grow at either of the six apex of the NWs, and potentially have arbitrary dipole orientations. This implies that not all QDs will couple into the CPP modes, which is exactly what the data in Figure 5-5 suggests. Note also that as we got closer to the VG end (Figure 5-5b), the relative intensities of the QD emissions evidenced which emitters are likely positioned closer to the NW end. The most representative example is the QD with emission at ~689 nm, which clearly increased its relative intensity compared to the other QDs when moving from (a) to (b).

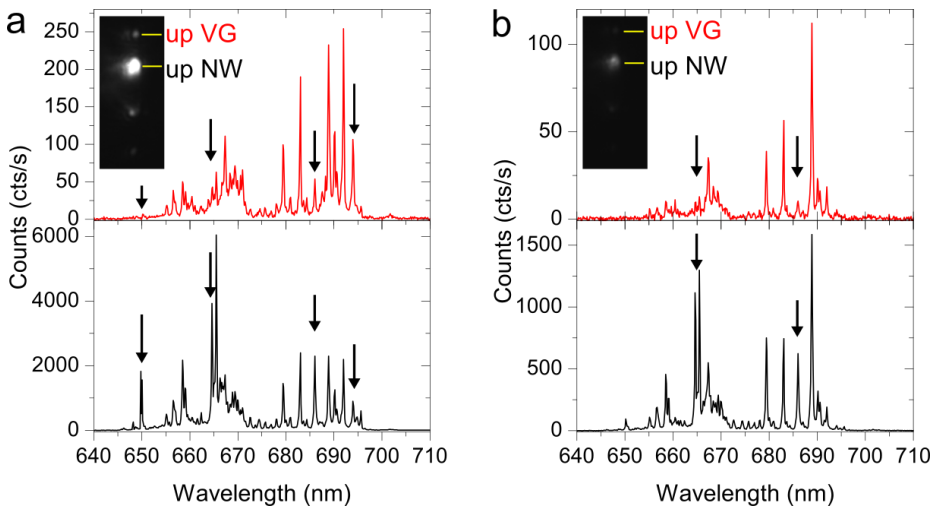

Figure 5-5. Coupling of a few QDs to the CPPs. a-b) Emission spectra of the QDNW-VG device while the excitation was placed at two positions near the NW upper end (approaching the end from **a** to **b**), both for the coupled emission collected at the upper VG end (red spectra) and the emission collected from the excitation position (black spectra). The insets are the corresponding CCD images at each of the excitation positions.

5.3.2 Nanowires with low density of self-assembled quantum dots

In this section, we investigate NWs with a thinner AlGaAs shell, with the goal of isolating the contribution and coupling of single QDs to the VG waveguide modes. In particular, we assembled NWs with a shell thickness of 50 nm, which from a previous characterization exhibited a QD density four times lower than the NWs with a 100 nm thick AlGaAs shell.[75]

DEVICE I: COUPLING FROM A QD CLUSTER TO THE VG MODES

For a first device, the NW segment (200 nm ±5 nm in diameter and 3.6 µm long) was placed inside a 15 µm long VG. The schematic in Figure 5-6a illustrates the emission channels of this hybrid configuration. For a NW placed inside the VG channel, a fraction of the emission launches propagating plasmon modes that out-scatter at the VG ends, while the un-coupled emission radiates from the NW into the free-space modes.

While exciting the NW at one of the QD positions, CCD images were acquired for a collection polarization parallel and transversal to the VG long axis (Figure 5-6b&c respectively). These images comprise only the contributions from the QD emission, since a short-pass filter blocked the emission from the GaAs core. We only note weak signals at the VG end mirrors, as opposed to the clear spots in the previous sections, which is likely related to the few QDs contributing to the collected images.

Without the filter, we could record the spectral contributions from both the NW core and the QD emissions (Figure 5-6d&e respectively). The black traces correspond to the polarization parallel to the VG axis, while the red and orange traces to the transversal polarization. The GaAs core emission shows a clear anisotropy for the parallel polarization, and exhibits Fabry-Perot like oscillations. For the QD emission, the polarization preference is not as clear, since there are different behaviours for the few QDs lines emitting within a 10 nm window. Despite this, only the QD line at ~661 nm exhibited reasonable coupling from looking at the emission at the VG end, so we decided to look closer into this emitter.

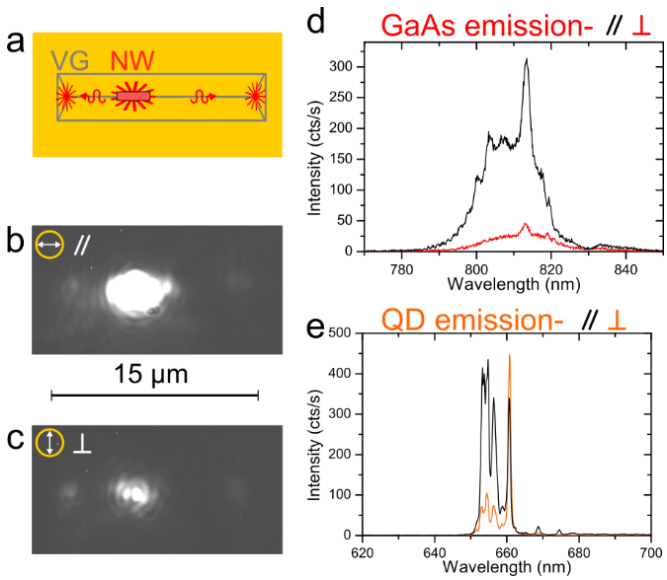

Figure 5-6. Low QD density NW inside a VG waveguide. a) Schematic of the assembled device and its operation. Light can directly couple to free-space modes or alternatively couple to the plasmon modes of the VG and propagate until scattered out at the VG end mirrors. b-c) CCD images of the QDNW-VG device for a collection polarization parallel and transversal to the VG long axis respectively. d) Emission spectra for the GaAs core emission for the parallel (black) and transversal (red) polarization collection. e) Emission spectra of the few QDs at this position, for the parallel (black) and transversal (orange) polarization collection.

POLARIZATION DEPENDENCE OF THE EMISSION

An azimuthal polarization analysis of both the GaAs and the QD emissions was carried out. The spectra at both VG ends and from the excitation position was recorded for the full polarization angle range, using 10º steps in the linear polarizer. We integrated the emission peaks for the broad GaAs spectra and the QD line at ~661 nm, and present them in Figure 5-7 as normalized polar plots. The results for the GaAs core emission are summarized in Figure 5-7a, which shows that although the emission is polarized mainly parallel to the NW long axis, at the VG ends, the polar plots tend to align towards the transversal axis. The observation of the parallel emission from the NW position is consistent with a previous study on very similar NWs,[73] however, at the VG ends, a stronger transversal polarization dependence is expected in accordance to the CPP mode characteristics.

For the QD emitting at ~661 nm, the polar plots are presented in Figure 5-7b. In contrast to the GaAs emission, the QD exhibits a polarization that is roughly at a 30º angle with respect to the transversal axis of the NW. Nevertheless, at the VG ends we also observed the out-scattered emission to be closely polarized towards the transversal axis. The small angle deviations observed in both cases could be related

to the fact that this particular NW was not perfectly positioned within the symmetry axis of the VG, as can be observed in the corresponding SEM image (Figure 5-7c).

A pure CPP mode localized at the bottom of the VG will have electric field lines pointing mainly in the transversal direction (Section2.2.1). However, if the off-axis QDs can launch plasmons deviating from the CPPs confined at the very bottom of the VG, the electric field lines of the propagating plasmon will not point strictly transversal to the sample plane. This implies that when the plasmon reaches the end of the VG, the measured polarization of the out-scattered signal can exhibit a stronger contribution for the direction orthogonal to the branched channel. The black arrows in Figure 5-7c illustrate the apparent scattered out polarizations that plasmons traveling on one of the side walls will have once it arrives to the branched channel at the end of the VG, which in this case would agree with the small angle deviations observed mainly in Figure 5-7a.

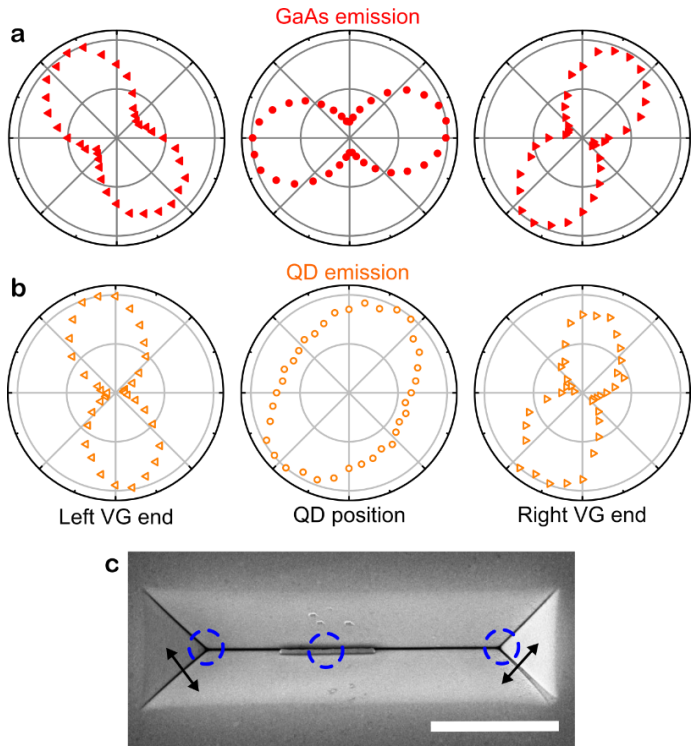

Figure 5-7 Azimuthal polarization emission in a QDNW-VG device. a-b) Polar plots of the GaAs core emission and the 661 nm QD line. From left to right: left VG end collection, from the excitation point and from the right VG end. The GaAs emission at the NW is polarized parallel to the NW long axis, while the QD is roughly 30º from the transversal axis. In both cases, at the VG ends, the polarization tends to align transversal to the VG long axis. c) SEM image of the hybrid device showing the 3.6 µm long NW with a diameter of 200 nm ± 5 nm, inside a 15 µm long VG. The blue circles indicate the collection positions, while the black arrows illustrate the apparent polarization that a plasmon will exhibit when reaching the VG end in case that it´s not fully confined at the bottom of the VG. Scale bar is 5 µm.

DEVICE II: BRIGHT QD COUPLING TO THE VG MODES

Here, we present the results of a second hybrid NW-VG device. The NW segment had a diameter of 210 nm ±10 nm and 4 μm in length, and was also positioned inside a 15 μm long VG (Figure 5-8a). Unfortunately, as seen in the SEM image, this NW was also not perfectly placed at the centre of the VG. Nevertheless, we still observed coupling of QD emission to the waveguide propagating modes.

The collected CCD images for the parallel and transversal polarization are shown in Figure 5-8b&c respectively. As with the previous device, the images are saturated to recognize the contributions at the VG ends. A small difference can be noted in the contribution from the left VG end, with a brighter spot for the transversal polarization. On the other hand, since the NW is closer to the right VG end, at that position it is difficult to evaluate the relative strength of the different contributions.

In turn, we rely more confidently on the spectral analysis to quantify the polarization contributions from the QD emission. In Figure 5-8d we present the spectra collected from the VG ends and the confocal position, when exciting a QD with emission at ~671 nm. The black traces correspond to the parallel polarization collection while the orange traces correspond to the transversal polarization. The transversal polarization clearly dominates the signal at the left VG end, while at the QD position and the right VG end the parallel polarization has stronger contributions.

To evaluate the polarization dependence in detail, Figure 5-8e shows the polar plot for these three collection positions (left VG, excitation position and right VG). This particular QD exhibits a polarization that is oriented towards the NW long axis, quite different from the previous device. Nevertheless, this is not surprising given that these QDs have been shown to have variable dipole orientations.[73] We note that at the right VG end, the polarization of the out-scattered light is aligned towards the parallel axis and is not strongly anisotropic. We think that the proximity of the NW to the VG end could be playing a role, and a mixture of free-space scattering with the guided contributions is observed. On the other hand, the left VG end is distanced enough from the NW (~6.2 μm), meaning the guided contributions dominate the signal scattered out at the VG end over the diverging free-space emission from the NW (i.e., clear transversal polarization of the polar plot).

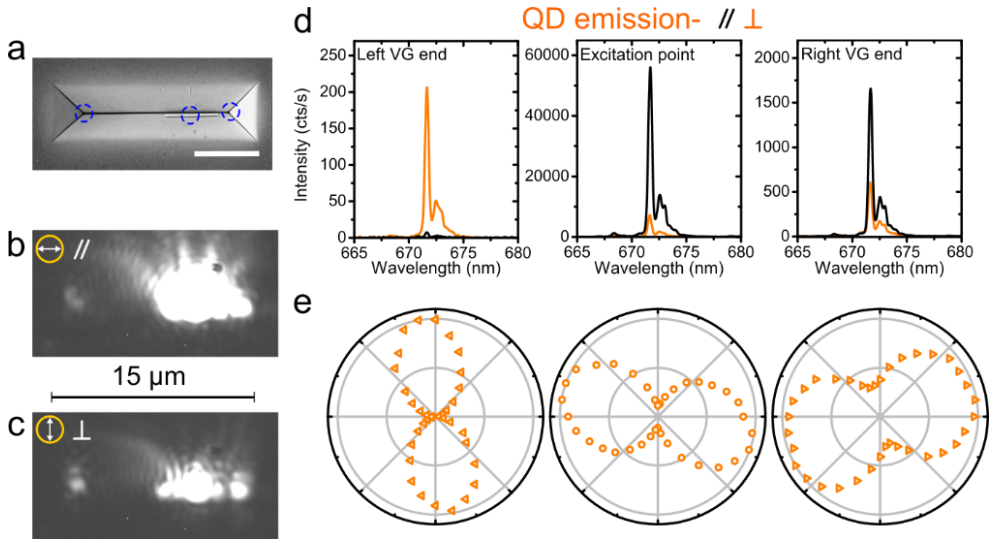

Figure 5-8. Optical characterization of a second QDNW-VG device. a) SEM image of the assembled device, showing a 4 µm long NW with 210 nm ± 10 nm diameter, inside a 15 µm long VG. Scale bar is 5 µm. b-c) CCD images of the device upon optical excitation for the parallel and transversal collection respectively. d) Emission spectra of the QD embedded in the NW collected from the left VG end, the excitation position and the right VG end. The black traces correspond to the parallel polarization collection, while the orange traces to the transversal polarization. e) Azimuthal polarization plots of the emission at the three collection positions.

Evidence of Single QD emission

The QD in this NW was particularly brighter than the ones measured in the previous device, meaning that the signal was sufficiently strong to carry out auto-correlation measurements. To do so, we filtered the emission signal with a diffraction grating in order to send only the emission at ~671 nm into a Hanbury-Brown and Twiss (HBT) setup. In Figure 5-9, we plot the autocorrelation coincidences for the emission at ~671 nm collected from the excitation position. A clear anti-bunching dip characteristic of a single quantum emitter ($g^2(t=0)<0.5$) is observed. We tried the measurement with the signal collected from the VG ends, however the count rates were too low at the two APDs in the HBT setup to get a good measurement within reasonable signal to noise ratio and acquisition time. Nevertheless, since we did obtain the same spectral features at both VG ends as we did on the confocal collection point, there is no reason why the signal coupled to the VG modes should not exhibit single photon properties.

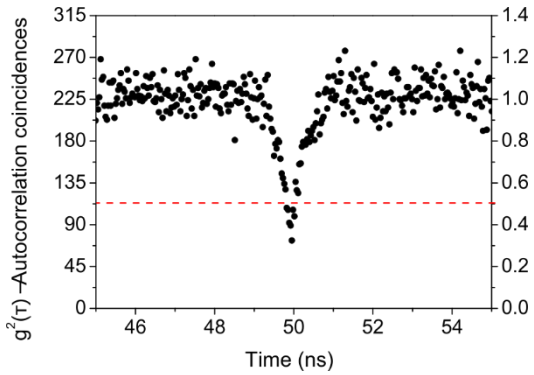

Figure 5-9. Single photon emission from the QDNW-VG device. Autocorrelation coincidences for the QD emitting at 671 nm. The measurement clearly shows a dip below the 0.5 level, characteristic of a single quantum emitter.

5.4 Conclusions and Outlook

In conclusion, we presented a hybrid photonic platform comprised of semiconductor NWs with embedded QDs, integrated inside VG plasmonic waveguide channels. To assemble such a hybrid device, we used micro and nano-manipulation techniques to deterministically position single NW segments at the bottom of VG channels. We assembled devices with NWs embedding high and low QD densities. Wide-field photoluminescence imaging and azimuthal polarization dependent spectral analysis evidenced the coupling of the QD emission to the propagating modes supported by the VG plasmonic waveguides. For NWs with high QD density, we observed the coupling of a large number of QDs covering a broad spectral range. At low excitation powers and by positioning the excitation spot near one of the VG ends, we could excite only a few QDs and observe different coupling behaviours for individual lines. This observation can be understood from the variability in QD position and dipole orientation within the NWs, which can lead to different coupling efficiencies to the VG modes. Finally, we demonstrated that indeed we can assemble devices that could be operated at the single QD level by using the low QD density NWs. The single photon emission was confirmed by means of autocorrelation measurements.

The integration of semiconductor NWs embedding single quantum emitters with such VG waveguides represents a promising platform for integrated circuits using single photon sources. One limitation of our current system is that the relative QD position and dipole orientation within the VG mode is not deterministic, given the geometrical characteristics of this type of self-assembled QDs. A possible way to circumvent this issue is to employ NWs with QDs axially centred inside the NW.[72] Those structures can potentially be well suited to match the propagating mode of the

VGs and thus improve the coupling efficiency from the QD to the plasmon modes. Additionally, in contrast to other quantum emitters platforms, the NW heterostructures can be tailor designed to be compatible with electrical injection, opening an interesting avenue for an electrically driven single photon emitter integrated within a compact plasmonic circuit.

Chapter 6 Plasmonic waveguide-integrated nanowire lasers

Next-generation optoelectronic devices and photonic circuitry will have to incorporate on-chip compatible nanolaser sources. Semiconductor nanowire lasers have emerged as strong candidates for integrated systems with applications ranging from ultrasensitive sensors to data communication technologies. Despite significant advances in their fundamental aspects, the integration within scalable photonic circuitry remains challenging. In this chapter, we report on the realization of hybrid photonic devices consisting of nanowire lasers deterministically positioned inside wafer-scale lithographically designed V-groove plasmonic waveguides. We present experimental results of NWs with different core diameters and show evidence of the lasing emission and coupling to the propagating channel plasmon polariton modes supported by the waveguides, enabling on-chip routing of coherent and sub-diffraction confined light with room temperature operation. Furthermore, theoretical considerations indicate that the observed lasing is facilitated by a waveguide hybrid photonic-plasmonic mode. This work represents a major advance towards the realization of application-oriented photonic circuits with integrated nanolaser sources.

6.1 Integrated NW-VG laser platform

An ideal platform of integrated photonic circuits should comprise all of its key components within the same chip, including the light source, transmission lines, modulators, and detectors, while offering a small footprint and low power consumption.[145] On-chip nanolasers represent an ideal solution for the light source integration, potentially circumventing the need of free-space coupling mechanisms,[58] and several candidates have emerged over the last couple of decades.[4] In this context, semiconductor nanowire (NW) lasers have received increasing interest owing to their intrinsic quasi-one-dimensional cavity geometry, the variety of high-quality materials that enables lasing over a wide spectral range, from the near ultra-violet to the near infrared,[87] and the potential to combine epitaxial heterostructures with unique optoelectronic properties.[146]

In the technologically relevant near-infrared region, NW lasers based on Gallium Arsenide (GaAs) have shown great progress, where both pulsed and continuous wave operation have been demonstrated.[89–96] Furthermore, lasing action has been realized not only from photonic modes in horizontal[89,90] and vertical cavities,[92] but also from hybrid plasmonic modes in NWs assembled onto metallic substrates.[95,96] To fully exploit the potential of such a localized and coherent light source, a platform demonstrating the integration of NW lasers with purposefully designed photonic circuitry remains highly desirable.[87]

So far, this task has been missing in studies focused on NW lasers, with only a few works demonstrating energy transfer into colloidal metallic nanowires. However, it is not clear how to pursue complex and predefined circuitry design with such colloidal particles.

In this chapter, to address the need for an application oriented integrated NW laser platform, we demonstrate the integration of individual GaAs NWs with lithographically designed V-groove (VG) plasmonic waveguides.[147] The proposed hybrid NW-VG platform is schematically illustrated in Figure 6.1, which shows a NW positioned at the bottom of a gold VG channel. Upon optical excitation, the NW is capable of lasing and furthermore coupling the emission to the propagating channel plasmon polariton (CPP) modes supported by the VGs, thus providing a coherent and localized source of energy routed across the surface of a chip.

We will first provide the reader with a background on the state-of-the-art of the NW lasers. Then, we will present details of our hybrid NW-VG devices, together with the description of the optical characterization setup. Finally, we will provide evidence of the lasing action in these hybrid systems, and of the emission coupling to the CPP modes supported by the plasmonic VG waveguides.

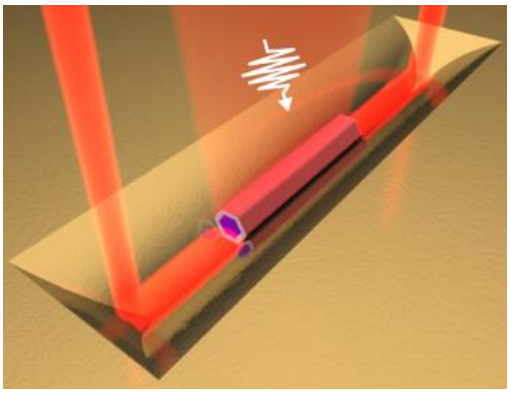

Figure 6-1 Schematic illustration of the hybrid NW-VG device. Upon pulsed excitation above threshold, the NW can couple its lasing emission to the supported modes of the VG, propagate along the waveguide and out-couple at the end mirrors.

6.2 Nanowire lasers: operation principle

The well-accepted operation mechanism of a semiconductor NW laser follows that of a Fabry-Perot (FP) type of laser, where the NW simultaneously provides the gain medium and the cavity resonator (i.e., no external mirrors involved). The cylinder-like shape of the NWs together with the index mismatch between the NW material (e.g., n=3.6 for GaAs) and the surrounding medium (n=1 for air) provide the means for the electromagnetic (EM) confinement, waveguiding of the supported modes, and cavity feedback through the reflection at the NW end facets.

In a standard FP laser, such as the common Ti: Sapphire lasers used in research laboratories, the mode propagation losses are negligible, and the lasing threshold is governed mainly by the reflectivity coefficients of the mirrors, which can be near unity. However, in NW lasers, the lasing condition results from an interplay between the material gain and the two main loss mechanisms (i.e., reflection losses at the NW end facets and the mode propagation losses). In these NW lasers, the mode losses are no longer negligible, especially when hybrid plasmonic modes are involved due to the ohmic losses in the metal. Lasing action is achieved when the round-trip gain of the generated photons inside the NW cavity exceeds the round-trip losses, following the expression:

$$\Gamma g > \alpha_{WG} + \alpha_M = \alpha_{WG} + \frac{1}{2L}\ln\left(\frac{1}{R_1 R_2}\right) \quad (1)$$

where Γ is the mode confinement factor, g is the material gain, α_{WG} the mode propagation loss and α_M represents the mirror losses, in which L is the length of the NW, and $R_1$and R_2 constitute the effective reflection coefficients of the corresponding mode at each end facet.

As mentioned in Chapter 2, even though the first reports claiming lasing from NWs were published in 2001, it wasn´t until 2008 that Zimmer *et al* reported the first clear evidence of the transition from amplified spontaneous emission (ASE) to lasing action in a ZnO NW.[85]

This conclusion can be properly deduced when analysing the power in-power out (P_{in}-P_{out}) relation in a log-log scale, which typically exposes the three distinct emission regimes in a so called "S-shape" plot. The three regimes are comprised by a linear regime at low pump powers (spontaneous emission), followed by a superlinear increase in intensity and linewidth narrowing (ASE regime), and finally a second linear regime which is the lasing regime.

Additionally, in the lasing regime, due to the coherence of the emission, a signature of interference fringes can be generally observed when collecting the emission into a camera. The interference pattern comes from considering two local in-phase sources at each of the NW facets.[84] In our work, we follow these guidelines when claiming lasing action in our hybrid devices.

6.3 Materials and Methods

In this section, we first provide details on the individual constituents of our hybrid devices, namely the semiconductor NWs and the V-groove plasmonic waveguides, followed by details of the assembly approach and the optical characterization setup.

6.3.1 Core-shell-cap GaAs nanowires

The NWs used in this chapter were developed by Gözde Tütüncüoglu in the group of Prof. Anna Fontcuberta i Morral at the École Polytechnique Fédérale de Laussane (EPFL) in Switzerland.

We followed the geometry guidelines described by D. Saxena *et al* and B. Mayer *et al*.[89,90] Both groups determined that the optimal design of a GaAs based NW laser should consist of a so-called core-shell-cap layout, which consists of a GaAs core (minimum diameter around 300 nm), which provides the gain in the system, followed by an AlGaAs shell (of at least 10 nm), that acts as a passivation layer to inhibit surface recombination of the excited states in the GaAs core, and finally, a thin ~5nm GaAs cap layer that protects the Al content from oxidizing. Tuning of the GaAs core diameter provides a compromise between the number of lasing modes supported by the NW, the reflection coefficients of the facets and the gain medium volume available to overcome the losses.

Our core-shell-cap GaAs/AlGaAs/GaAs NWs were grown by a self-catalysed vapour-liquid-solid method (VLS) using Molecular Beam Epitaxy (MBE) on a GaAs (111)B substrate. In this chapter, we present results of three distinct diameters, namely 550 nm, 370 nm and 310 nm in total diameter, hereafter referred as Type I, II and III respectively. The GaAs core diameter was varied, while the AlGaAs shell and the GaAs cap were kept constant at 30 nm and 5 nm thickness respectively. Figure 6-2 shows a birds-eye view of one of the as-grown NW samples.

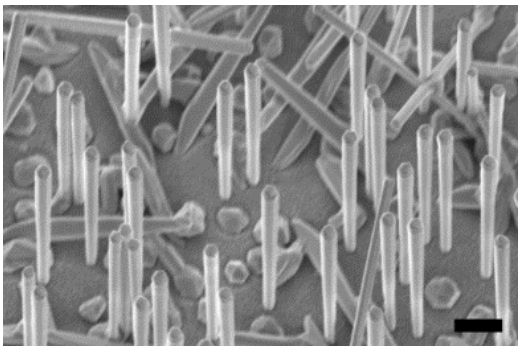

Figure 6-2 GaAs semiconducting NWs. SEM image of as-grown NWs on a GaAs (111)B substrate. Scale bar is 1μm.

6.3.2 VG plasmonic waveguides

The VG structures used in this chapter were developed by Cameron L.C. Smith at the Technical University of Denmark (DTU), and characterized by Ilya Radko in the group of Prof. Sergey I. Bozhevolnyi at the University of Southern Denmark (SDU).[56] For details on the structures, please refer to Section 5.2.

To assess the performance of these VGs, COMSOL simulations were performed to calculate the electric field amplitude distribution of the supported fundamental CPP mode at a wavelength of 870 nm (Figure 6-3), corresponding to the band-edge emission of GaAs at room temperature. The mode is confined at the bottom of the VG, and from the inset image we can appreciate that the electric field lines are pointing mainly in the transversal direction with respect to the VG long axis (i.e., the CPPs are TE polarized with respect to the in-plane surface).

These simulations were performed by Javier Cuerda in the group of Prof. Francisco J. García-Vidal at the Universidad Autónoma de Madrid (UAM).

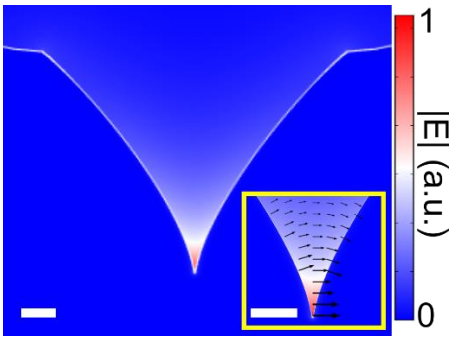

Figure 6-3 Electric field mode amplitude |E| profile of the fundamental CPP mode supported by a VG waveguide at 870 nm. The CPP mode is confined at the bottom of the VG with electric field lines mainly transversal to the VG long axis (inset). Scale bars are 300 nm.

6.3.3 NW transfer and positioning into the VG channels

To transfer the NWs from their as-grown substrate to the VG chip, and position them inside the VGs, we used the same micro and nanopositioning approach described in Chapter 5. Here, we just mention some considerations pertinent to the specific geometry of these NWs. In the micromanipulation step, where a pulled optical fibre tip was used, we found that for NW diameters above ~400 nm it was possible to rely only on this step to perform the full assembly. This allowed for the rapid assembly of our devices, as the use of the AFM nanomanipulation technique was not required.

Figure 6-4 presents a sequence of optical microscope images (a-d) during one of the assembly runs. We can appreciate four NWs that have been previously positioned alongside the 30 μm long VGs (Figure 6-4a). In Figure 6-4b&c, two devices have already been assembled, while the fibre tip can be observed positioning the top-left NW into the VG. Finally, in Figure 6-4d the four devices have been assembled, which can be seen in detail in the corresponding SEM images (Figure 6-4e-h), demonstrating the reproducibility of this simple approach. In Figure 6-4i, we present a bird´s eye view of the device outlined in Figure 6-4g, together with a closed-up view of one of the NW end facets (Figure 6-4j), confirming a symmetric placement of the NW within the VG channel.

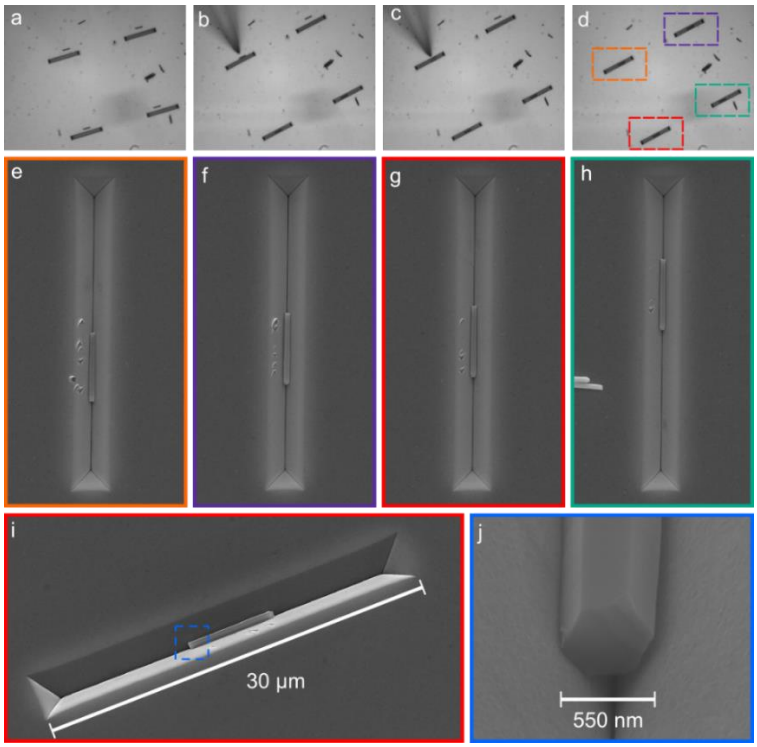

Figure 6-4 Assembly of the hybrid NW-VG devices. (a)-(d) Sequence of optical microscope images of the glass-tip based micro-positioning of a NW into a VG channel. (e)-(h) Top view SEM images of the four NW-VG devices outlined in coloured dashes in (d) showing the positioning reproducibility in our approach. (i) Angle-tilted SEM image of the device outlined in (d) with red dashes. The VG channel is 30 µm long while the NW is 6.8 µm long. (j) A zoomed ´bird-eye´ view of the NW facet outlined in (i) with blues dashes. For scale reference, the NW diameter is 550 nm.

Some defect scratches can be appreciated on the sidewalls of the VG, result of the fibreglass tip contact with the metallic walls. This is expected given that we relied on a simple but still manual operation of the micromanipulator, which in future works could be replaced by automated positioning controls. Nevertheless, as will be seen in the optical characterizations, these sidewall defects did not seem to affect the operation of our devices, as the propagating plasmon modes are confined at the bottom of the VGs (Figure 6-3).

For NWs with diameters below 400 nm, the glass tips were not capable of pressing the NWs towards the bottom of the VGs, likely as a result of a geometric constraint between the fibre tip and the VG channel. Under these circumstances, we only positioned the NWs at the border edge of the VGs, and used the AFM nanomanipulation technique to move the NWs down the inclined plane and into the bottom of the channel. It is worth considering that this limitation can be potentially overcome by engineering the glass tip geometry and mounting angle relative to the sidewall profile, such that the slip condition is inhibited.

6.3.4 Experimental setup

To optically characterize the NWs and hybrid devices, we implemented a homemade photoluminescence optical microscope, as shown schematically in Figure 6-5. We used pulsed optical excitation with a Ti: Sapphire laser tuned at 730 nm (~200 fs pulses with 80 MHz repetition rate). Since our optical microscope and laser system were in separate optical tables, we coupled the laser to a single-mode fibre in order to bridge the excitation source to our microscope setup. The excitation laser was then collimated and sent into a 40x 0.65NA objective. Inserting a cylindrical lens (f=1 m) on the excitation path provided us with an elliptical beam of approximately 18.8 μm^2 (diameter along the major and minor axes of 20 um and 1.2 um respectively, see the inset in Figure 6-5). The beam spot was sufficiently large to fully excite NWs and achieve sufficient gain in our system. Before the objective, we installed a 50:50 beam-splitter (BS). A neutral density (ND) filter wheel was placed before the BS in order to control the excitation power reaching the sample, which was measured with a power meter just after the ND filter.

The substrates with VGs and NWs were mounted on a 3-axis piezoelectric stage installed on a 2-axis micrometre stage, providing short and long-range movements across the plane of the sample. The emission from the NWs was collected through the same objective. We placed a 785 nm long-pass filter along with a linear polarizer after the BS, allowing us to perform polarization dependent collection analysis. The emission was split into two channels using another 50:50 BS. On one channel, we focused the emission into an EMCCD camera, providing us with a wide-field view of the emission at the sample plane. It is useful to observe the emission from the sample in real-time, as it provides the means to observe the lasing transition due to the appearance of interference fringes, but most importantly to evidence the coupled emission into the CPPs supported by the VGs. On the second channel, we focused the emission into a single-mode (SM) optical fibre, which was coupled to a spectrometer. By steering a mirror, we could selectively collect the emission into the fibre from different areas within our field of view, allowing us to independently collect the spectra from the NW or the out-coupled emission at the VG ends. We also introduced ND filters in the collection channels when necessary, as the emission from the NW facets was often several orders of magnitude higher than at the VG ends under the same excitation conditions.

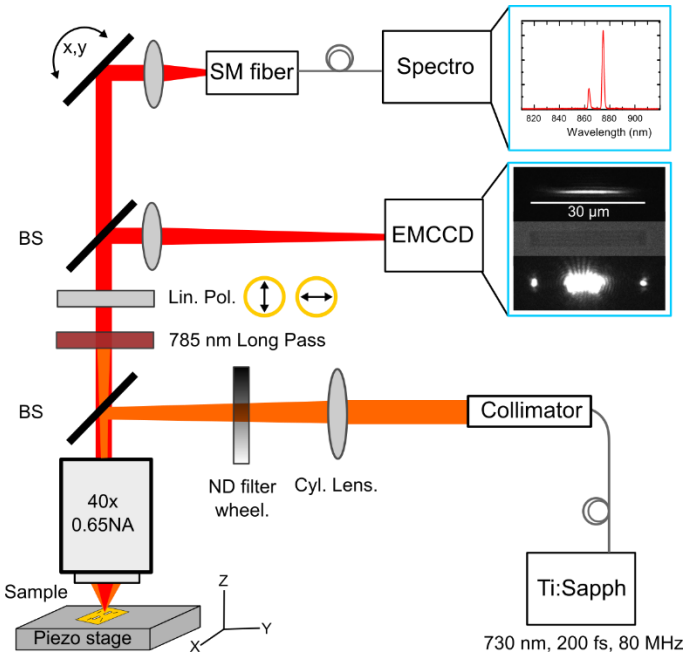

Figure 6-5 Basic features of the experimental setup. The excitation is carried out with a Ti: Sapphire laser under pulsed operation at 730 nm. A cylindrical lens forms an elliptical spot at the sample allowing to fully excite the NWs with a 40x 0.65 NA objective lens. The emission is collected through the same objective and analysed in two separate channels after filtering with a 785 nm long-pass filter and a linear polarizer. One channel images the sample on a EMCCD camera (the insets show examples from the elliptical excitation spot, a white-light illuminated image of a 30 µm VG, and the emission from a NW positioned inside the VG under lasing action). The second channel collects the emission into a single-mode fibre coupled to a spectrometer (the inset shows an example of the lasing emission line of a NW).

6.4 Integrated NW laser devices

In this Section, we present the results of the Type I, II and III NWs, which provide convincing evidence of the lasing emission and coupling to the propagating modes supported by the VGs. The different behaviours, both on top of the Au metallic film and in the hybrid NW-VG device geometry, help us understand the operation of these type of devices.

6.4.1 Type I NWs: initial plasmonic waveguide-integrated NW lasers

Our first realization of a plasmonic waveguide-integrated NW laser was achieved with the Type I NWs (total diameter in the range of 550 nm). The recorded EMCCD images for the device detailed in Figure 6-4g, are presented in Figure 6-6. The white arrows indicate the orientation of the linear polarizer at the collection channel, where we have focused on two distinct orthogonal polarizations, namely parallel and transversal to the VG long axis. Figure 6-6a-b correspond to an excitation power below the lasing threshold. Already at this point, we get the first evidence that a fraction of the emission from the NW couples to the

CPP mode supported by the VG, concluded from the stronger contributions at the VG end mirrors for the transversal polarization.

We recall that the CPPs supported by these VGs are TE-polarized modes, with the electric field pointing in the transversal direction with respect to the VG long axis. The EMCCD images for both polarizations were also obtained above the lasing threshold (Figure 6-6c-d), where we can notice the presence of interference fringes, associated with the coherent emission under this lasing regime. As it can be observed, the CPP coupling of the emission is preserved in the lasing regime, with the signal at the VG ends being stronger for the transversal polarization. We attribute the non-zero contributions observed for the parallel polarization images (Figs. 6.7a&c), to either free-space scattered light at the VG edges or from other higher order modes supported by the NW-VG system.

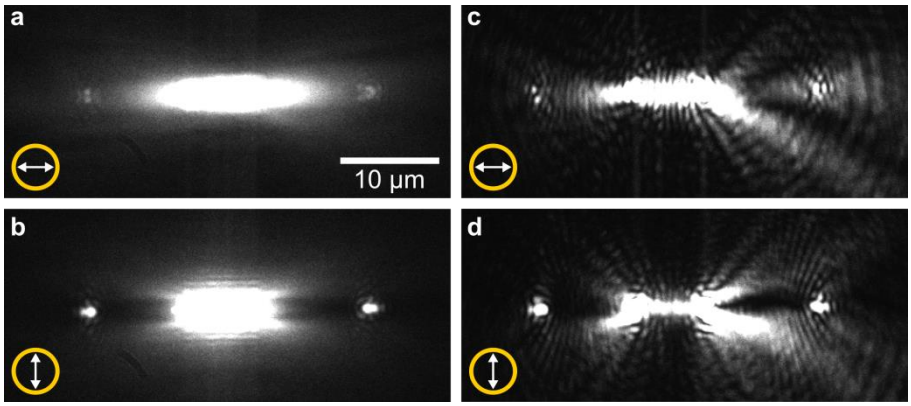

Figure 6-6 EMCCD emission intensity images of the hybrid NW-VG device. (a)-(b) correspond to low excitation power well below threshold (150 µW) while (c)-(d) correspond to excitation above the lasing threshold (2.4 mW). The white arrows represent the filtered collection polarization. A clear difference is observed for the emission out-coupled at the VG ends in (b) and (d) as compared to (a) and (c), with dominance of the polarization transversal to the VG main axis, in agreement to the CPP nature of the supported mode inside the VG channel. The presence of interference fringes in (c)-(d) is a signature of lasing action in this device.

Figure 6-7a presents the spectra collected from the right VG end, below and above the lasing threshold (sky blue and orange respectively). Below the lasing threshold, the spectrum is characterized by a broad emission featuring FP like oscillations. As the system enters the lasing regime, a strong peak dominates the spectra at about 876.7 nm. To confidently claim that the system has indeed transitioned into the lasing regime, we can analyse the emission intensity of this peak as a function of the excitation power in a log-log scale (P_{in}-P_{out} plot in Figure 6-7b). We clearly see that the device exhibits the typical "S-shape" curve, where the system transitions from a linear regime of spontaneous emission (broad spectrum) to a second linear regime of lasing oscillation via a superlinear regime (shaded area in Figure 6-7b roughly delimits the ASE regime). The sky-blue and orange data points correspond to the graphs presented in Figure 6-7a.

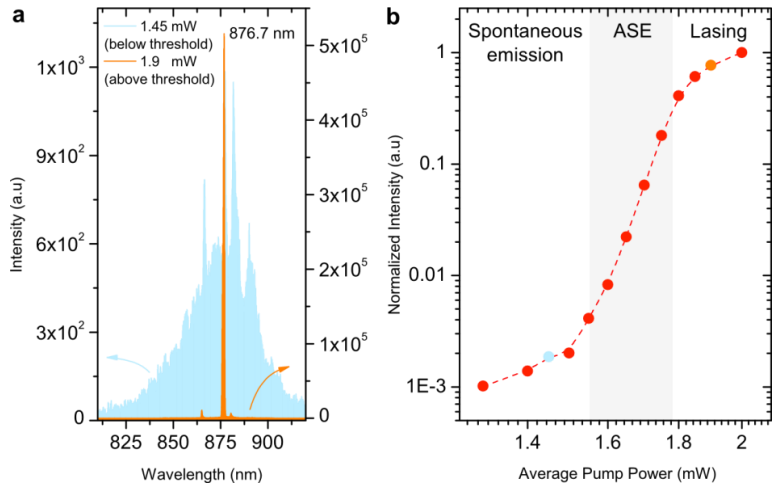

Figure 6-7 Emission characterization of the NW-VG device. a) Emission spectra collected with transversal polarization from the left VG end (Fig. 6.6b&d), below the lasing threshold (1.45mW, sky blue) and above lasing threshold (1.9mW, orange). Fabry-Perot oscillations can be observed below threshold. b) P_{in}-P_{out} in a log-log scale, plotting the intensity of the emission peak at 876.7 nm as a function of average excitation power. The S-shape confirms the observation of a transition from the two linear regimes (spontaneous emission and lasing) via the superlinear regime characteristic of ASE regime. The sky-blue and orange data points correspond to the traces in (a).

MONITORING THE LASING BEHAVIOUR OUTSIDE AND INSIDE THE VGS

To further understand the behaviour of our hybrid devices, we studied the evolution of the lasing properties of specific NWs from a position on top of the flat Au surface alongside the VGs, to the position at the bottom of the VG. Figure 6-8a-b shows optical microscope and EMCCD images for the "outside" (a) and "inside" (b) cases. The EMCCD images were acquired at an excitation above the lasing threshold (presence of interference fringes) for the transversal polarization in collection. The emission collected from the left NW end corresponds to the grey trace in Figure 6-8c, which exhibits a lasing peak at 871 nm. The associated S-shape curve is plotted in Figure 6-8d with the filled orange circles.

Once the NW is positioned at the bottom of the VG, we can observe the presence of the two out-coupled spots at the VG ends, confirming that the emission is coupled to the CPPs supported by the VG. The black trace in Figure 6-8c corresponds to the emission collected from the left VG end, exhibiting a strong peak at 871 nm. The associated power dependence plot for the main lasing peak (open orange circles in Figure 6-8d), confirms that the bright spot observed in the EMCCD image indeed has lasing characteristics.

A slight reduction in the superlinear step is noted (i.e., from the spontaneous emission regime to the lasing regime), which we associate to an increase in the β-factor of the hybrid NW-VG system. Additionally, minor side peaks were present in our spectra, some of which were only weakly contributing when the NW was on top of the Au film. The peak at 875 nm

(blue data points in Figure 6-8d) exhibits a similar S-shape in the P_{in}-P_{out} plot, suggesting it is a second lasing peak. However, the peak at 880 nm (green data points in Figure 6-8d) only exhibited a superlinear increase without transitioning into a second linear regime, suggesting that for the associated mode at the current excitation conditions, we only entered into the ASE regime.

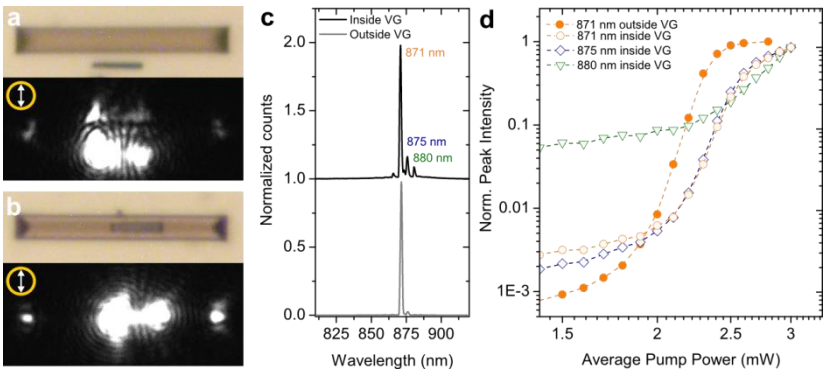

Figure 6-8 Emission characteristics of a NW laser before and after its assembly into the VG. a&b) Optical microscopy images (top) and corresponding EMCCD images (bottom) for the NW in the lasing regime (note the interference fringes). The length of the VGs is 30 µm. The EMCCD image in b) shows the signature of the CPP coupling (out-coupled emission at the VG ends). c) Spectra collected from the left NW end in the outside configuration (grey trace) and from the left VG ends in the inside configuration (black trace). d) Normalized P_{in}-P_{out} plots tracking the relevant peaks in c). The main peak at 871 nm (orange circles) undergoes a slight modification in the magnitude of the jump from the two linear regimes when going from the outside case (open circles) and the inside case (filled circles). The peak at 875 nm (blue symbols) also shows an S-shape behaviour, hinting that a second mode is able to lase. On the other hand, the data for the 880 nm peak (green symbols) shows only one transition, suggesting that this mode has only entered into the ASE regime.

Evidence of SPP generation for the NW-on-film configuration

Here, we briefly bring the attention to a special feature noticed when performing these experiments, as we think it can be implemented as direct evidence of the plasmon lasing nature of NW-on-metallic-film configurations.

In Figure 6-8a, we can appreciate the presence of the VG in the vicinity of the NW due to the scattering signals from the VG edges. These contributions are observed both at the VG border opposite to the NW and at the corners of the VG ends. We think that these are a consequence of surface plasmons polaritons (SPPs) generated at the Au/air interface, that can propagate along the film and eventually scatter out into free-space when encountering the edges of the VGs (scattering defects).

Figure 6-9a schematically illustrates this mechanism, where the top-view diagram shows a NW with two distinct emission channels, one being the free-space scattering from the NW end facets (red stars) and the second, the SPPs launched by the NW emission (arrows). The latter, can eventually scatter out into free-space when encountering defects along their path,

such as the VG edges. As it is well known, the SPPs have electric field lines pointing in the out-of-plane direction. When these SPPs reach a discontinuity, such as the VG trench, they will scatter out into free-space modes. In our case, due to the geometry of the open VG channel, they will reflect off the VG side wall and re-direct into the objective with a polarization component transversal to the edge´s long axis, as illustrated in the transversal view in Figure 6-9a, following the same principle when a polarized beam reflects of a angled mirror.

This mechanism is better appreciated with polarization dependent EMCCD images for another NW placed alongside a VG (Figure 6-9b). The recorded EMCCD images above the lasing threshold for the collection with parallel and transversal polarizations are shown in Figure 6-9c&d respectively. We can notice that the scattered contributions at the VG edge opposite to the NW exhibit stronger transversal polarization contributions when compared to the parallel collection. The signals at the VG ends do not exhibit a strong anisotropy, which can be explained as those VG edges are not orthogonal to either polarization.

We think that this is the first direct observation of the SPP launching by a NW laser on a metallic film system. Previous works have only focused on the lasing emission from the NW end facets,[95,96] leaving an open question regarding the discrimination as to whether a plasmonic or photonic mode is lasing in the system, which is typically based on theoretical considerations of the supported modes.

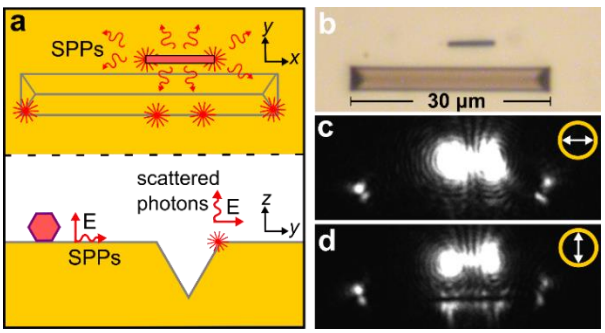

Figure 6-9 Surface plasmon lasing evidenced. a) Schematic illustrations of the emission channels in a NW-on-metallic film configuration, including free-space scattering and SPP launching. The SPPs that travel along the Au-air interface can scatter out to free-space and exhibit a polarization transversal to the edge defect. b) Optical microscope image of a NW alongside a 30 µm VG. c-d) EMCCD images of the NW excited above the lasing threshold for the parallel and transversal polarization respectively.

DETAILS OF THE CPP-COUPLED LASING EMISSION

Previously, we based the claim of the CPP-coupled lasing emission upon the comparison of the EMCCD images for the two orthogonal polarizations. Here we present data for another NW-VG device, also showing the EMCCD images for the collection polarization parallel

and transversal to the VG long axis (Figure 6-10a&b respectively), where we again observe stronger contributions at the VG ends for the transversal polarization.

The schematic illustration in Figure 6-10c can help to visualize the two emission channels in this NW-VG hybrid geometry, the direct free-space scattering at the NW facets, and the coupling to CPPs that propagate along the waveguide and eventually out-couple to free-space at the VG end mirrors. To understand better the polarization anisotropy, we recorded the spectra from four different positions along the NW-VG device, namely from the VG and NW ends (dashed circles), for the parallel (magenta) and transversal (orange) polarizations (Figure 6-10c).

The out-scattered emission from the NW facets does not exhibit a distinct preference in polarization, as some lasing peaks dominate in the transversal polarization and others in the parallel contribution. On the other hand, the emission collected from both VG ends (top and down plots in Figure 6-10c), show a clear anisotropy with a dominating transversal polarization contribution (orange). These observations are in agreement with what we expect from the TE polarized nature of the supported propagating CPP modes in the VG waveguides. We note that the coupled spectra from both ends of the VG exhibit differences in the dominating lasing peak, which we attribute to the potential multimode nature of such a thick NW and how the different NW facet geometries can influence the transfer efficiencies from the hybrid NW-VG modes to the bare CPP modes.

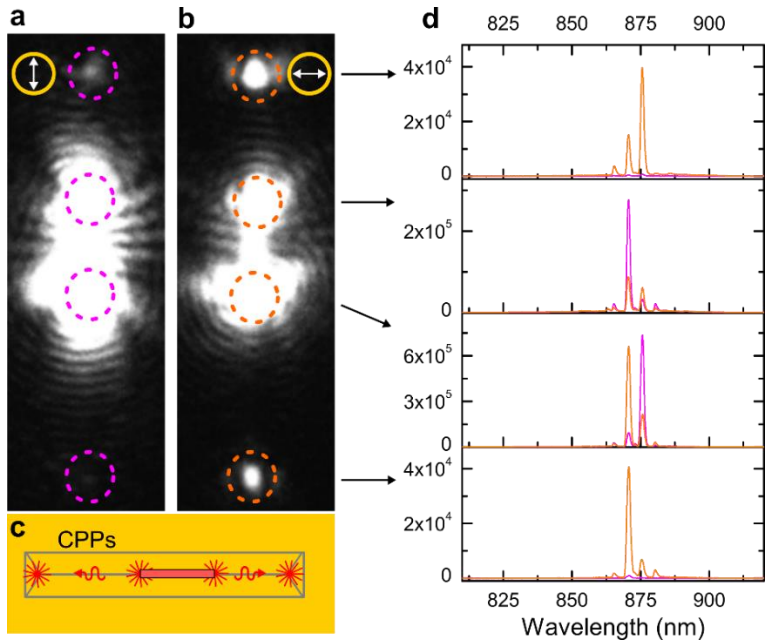

Figure 6-10 Details on the CPP coupling. a&b) EMCCD images of the device under laser action for the collection polarization parallel and transversal to the long axis of the VG respectively. There is a stronger signal from the VG ends when the polarization is transversal to the VG, as expected from the TE polarization of the CPP mode. c) Spectra collected from the NW and VG ends for a collection polarization parallel (magenta) and transversal

(orange) to the VG long axis. At the NW ends there is no distinct preference of polarization. On the other hand, the emission at both VG ends is clearly dominated by the transversal collection.

6.4.2 Type II NWs : towards single-mode lasing

As the NW diameter is reduced, we inherently reduce the number of supported modes by the hybrid system.[89] This section presents the results obtained with the Type II NWs, namely those with a total diameter in the order of 370 nm.

Figure 6-11 summarizes the characterization of a Type II NW (385 nm ± 26 nm diameter and 5.5 µm length) that was initially positioned along side a 30 µm VG and later brought inside the VG. The EMCCD images were acquired above the lasing threshold and thus exhibit interference fringes. A set of two images for each case is shown, corresponding to transversal (Figure 6-11a&d) and parallel (Figure 6-11b&e) polarization collection. Similar to the results shown previously for the Type I NWs, we can distinguish that for the "Outside VG" case, SPPs launched at the Au film eventually are out-scattered by the VG border edges. For the "Inside VG" case, we observe stronger contributions at the VG ends from the transversal polarization collection, revealing the CPP coupled emission in our system.

In Figure 6-11c, we present the normalized spectra collected from the right NW facet under the transversal polarization collection below (sky-blue) and above (orange) the lasing threshold, when the NW was placed alongside the VG. Similar data was recorded after assembling the hybrid device (Figure 6-11f), with collection from the right VG end. Below threshold, FP oscillations are observed within the broad spontaneous emission spectra of the GaAs NW. Above threshold, strong lasing peaks rise, and we note a change in the mode spacing and position of the lasing peaks when the NW is inside the VG. This is reasonable given that the supported hybrid modes can change from a NW-on-metallic-film to a NW-in-VG configuration.

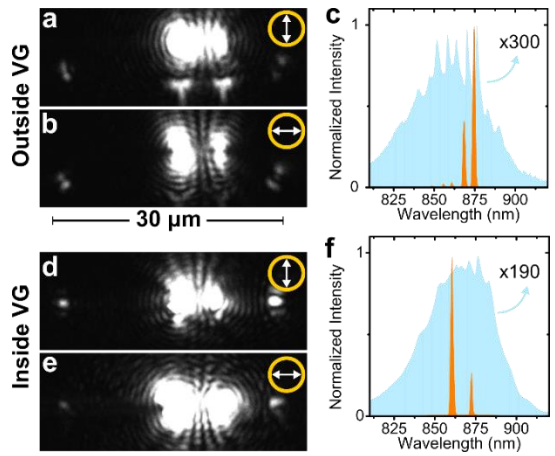

Figure 6-11 Characterization of a Type II NW outside and inside the VG. a&b) EMMCD images for transversal and parallel collection respectively, for the NW alongside the VG. c) Normalized emission spectra for a NW placed on top of a Au film, below (blue-sky) and above (orange) the lasing threshold. d&e) EMMCD images for

the transversal and parallel collection respectively, for the NW inside the VG. f) Normalized emission spectra for the same NW positioned inside the VG, below (blue-sky) and above (orange) the lasing threshold.

EVALUATING THE CPP COUPLING FOR A TYPE II NW

Next, we have a closer look into the polarization dependent emission properties of a second NW-VG device. Here, we present EMCCD images for the collection with polarization parallel and transversal to the VG main axis (Figure 6-12a&c respectively), together with a SEM image of the device to visualize the relative positions of the out-coupled signals (Figure 6-12b). The NW (376 nm ± 35 nm in diameter and 6.4 µm long) is symmetrically centred inside the VG, both across and along the VG axis. We observe an evident anisotropy in the emission out-coupled from the VG ends for the transversal polarization configuration, providing additional support to the finding that the NW-VG device is able to launch CPPs.

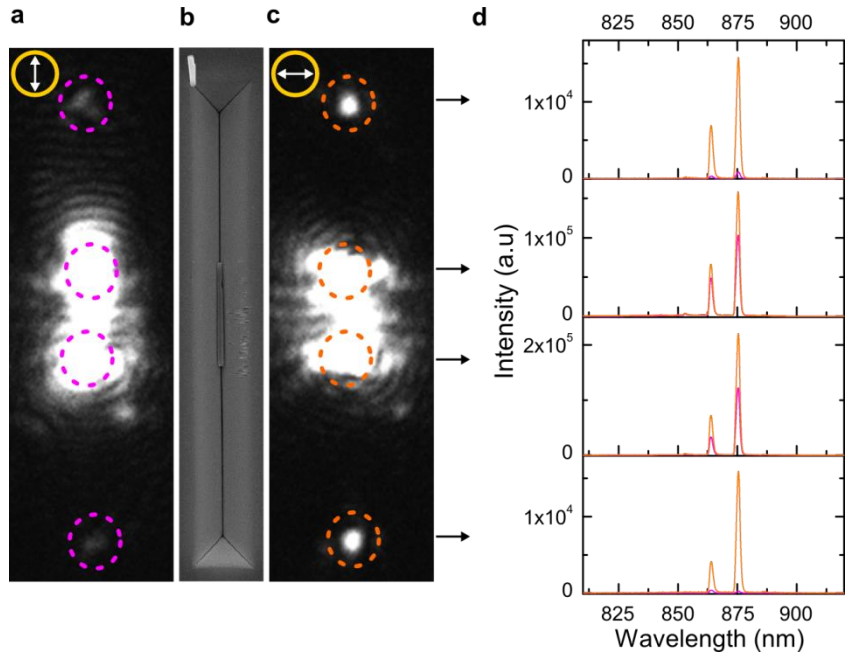

Figure 6-12 Evidence of CPP coupling with a Type II NW-VG device. a&c) EMCCD images of the device under laser action for a collection polarization parallel and transversal to the long axis of the VG respectively. b) Shows an SEM image of the assembled device. d) Spectra collected from both NW and VG ends for a collection polarization parallel (magenta) and transversal (orange) to the VG axis.

To quantify the polarization dependence, we turn to the spectra collected from four different positions along the VG axis, namely from the NW and VG ends (Figure 6-12d). The spectra are colour coded according to the highlighted dashed circles in Figure 6-12a&c (parallel and transversal polarization in magenta and orange respectively). We can extract the degree of linear polarization (DOLP) for the lasing peak at ~875 nm, given by $DOLP = (I_{\perp} - I_{\parallel})/(I_{\perp} + I_{\parallel})$, where $I_{\perp}$and $I_{\parallel}$ correspond to the peak intensity for the transversal and

parallel polarization collection respectively. At the NW facets, the emission does not exhibit a strong polarization preference, exhibiting $DOLP$ values of 0.21 and 0.29 for the upper and lower NW ends respectively. On the other hand, the situation at the VG ends is drastically different, with large $DOLP$ values of 0.89 and 0.97 for the upper and lower VG ends respectively.

These results confirm the excitation of CPPs from the laser emission coupling in our NW-VG platform, given the strong anisotropy in the transversal polarization contributions at the VG ends, and in agreement with the CPP characteristics (electric field lines in Figure 6-3). The results also shed light on the capability of these hybrid devices to provide well defined polarization states, thanks to the mode filtering properties of the VGs.

Simulated Hybrid NW-VG modes

To understand the behaviour of our hybrid NW-VG system, 2D and 3D EM simulations were carried out using COMSOL Multiphysics by Javier Cuerda in the group of Prof. Francisco J. García-Vidal at the UAM.

First, we determined the propagating EM modes supported by the hybrid NW-VG configuration. Several modes were found, many of which have the EM fields mainly confined inside the NW, given its ability to support photonic-like modes.[89] However, only four EM propagating modes are compatible with lasing action, as the other modes exhibit propagation lengths that are shorter than the length of the NWs.

The E-field profiles of these four modes are presented in Figure 6-13a-d, which we labelled as M_{VG1}-M_{VG4}. One of the modes exhibits a CPP-like distribution at the bottom of the VG (M_{VG1}), with Figure 6-3 as reference, while the other three modes mainly present photonic-like confinements inside the NWs (M_{VG2}-M_{VG4}). The M_{VG1} in particular exhibits a good mode overlap[148] with the bare CPP mode supported by the VG (25.5% versus <0.2% for M_{VG2}-M_{VG4}). While this can be a fair indication of the mode-matching between the NW-VG modes and the bare CPP mode, the mode overlaps do not account for the physical effects occurring at the NW facets, which include back-reflections and scattering out of the NW ends.

Instead, to quantify the transfer of energy into the subwavelength confined propagating modes, rigorous 3D FEM simulations were carried out to calculate the fraction of energy that channels into the CPP mode compared to the total energy exiting the NW facet, which we term here as the transfer efficiency (ξ). Note that this definition excludes the fraction of energy that provides the cavity feedback (i.e., the reflection coefficient). The M_{VG1} presents the largest value of ξ (23.8%), at least a factor of 15 larger compared to M_{VG3} (ξ =1.6%), while the other two modes exhibit negligible ξ values (<0.01%). Details of the mode characteristics are found in the Table 6.1.

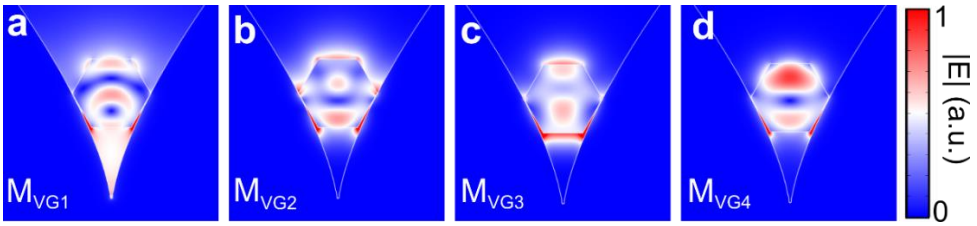

Figure 6-13 Supported hybrid modes of the NW-VG system. a-d) Simulated |E|-field mode amplitude profiles of the NW-VG system (M_{VG1-4}). M_{VG1} is a CPP-like mode while M_{VG2-4} mainly present photonic confinements within the NW geometry.

Mode	n_{eff}	L_p (μm)	R	ξ
M_{VG1}	$1.24+i*6.5x10^{-3}$	10.6	0.46	23.8%
M_{VG2}	$1.55+i*1.0x10^{-2}$	6.9	0.87	0.001%
M_{VG3}	$2.06+i*4.7x10^{-3}$	14.6	0.86	0.006%
M_{VG4}	$2.52+i*4.0x10^{-3}$	17.3	0.73	1.6%

Table 6.1. NW-VG supported mode parameters. From left to right: the effective refractive index, propagation length, reflection coefficient at the NW facets, and transfer efficiency into the CPP mode.

EXPERIMENTAL TRANSFER EFFICIENCY

Experimentally, the transfer efficiency of our NW-VG device was estimated from the measurements presented in Figure 6-12, by quantifying the contributions of the strongest lasing peak (875 nm) collected from one VG end and comparing it to the total emission decoupled from the corresponding NW facet (free-space scattering and the VG end contribution). From this simple calculation, we obtain transfer efficiency values of ξ =9.3% and ξ =7.1% for the upper and lower halves of the device, respectively. These experimental values represent a lower boundary since we used the simulated propagation length of the CPP mode (19.96 μm) to compensate for the intensities measured from the VG ends and we did not consider the fraction of energy lost from the CPP to free/space energy conversion at the VG end mirrors. The latter of these, together with experimental imperfections not present in the theoretical design, can explain the discrepancy with the simulated values.

Nevertheless, with an underestimated experimental transfer efficiency of nearly 10%, our device stands very well against previous realizations when considering the transfer of energy from an on-chip laser to a subwavelength confined propagating mode.[149–151] However, it is difficult to compare against previous NW plasmon lasers (i.e., NWs on metal films), because the SPP transfer signature has remained elusive (i.e., emission only collected from the

scattering at the NW facets).[95,96,152,153] Our numerical and experimental results suggest that the CPP-like mode supported by the NW-VG system (M_{VG1}) enables the lasing action observed in our experiments, because the emission contributions observed at the VG are compatible with the simulated values for M_{VG1}.

DETAILS OF THE NW-VG LASING SEQUENCE

To demonstrate that our hybrid NW-VG device exhibits lasing action and not just amplified spontaneous emission (ASE),[83,85] we provide here detailed results on the emission behaviour as a function of the incident pump power for the device presented in Figure 6-12. The peak intensity of the dominating emission peak (~875 nm), as obtained from the spectra collected from the right VG end (transversal polarization), is related to the average pump power measured before our beam splitter and objective (Figure 6-14a). The P_{in}-P_{out} clearly exhibits the three main emission regimes. We stress here the importance of presenting lasing data on a log-log scale[85,154], since a system entering only into the ASE regime will also exhibit a kink in a linear-linear plot (superlinear increase of intensity) and linewidth narrowing.

The details on the spectra collected from both VG ends are also presented here (Figure 6-14b&d), along with the associated EMCCD images (Figure 6-14c) corresponding to each of the coloured data points in Figure 6-14a. At low excitation power (below 450 μW) the system is clearly in the SE regime, with spectra characterized by a broad emission with FP oscillations. The EMCCD image exhibits a bright emission from the NW body and two dim spots at the VG ends (CPP-coupled SE). The sky-blue data point (500 μW) marks the transition into the ASE regime. At the mid-point of this regime (dark-blue data at 550 μW), the spectra are characterized by two narrow and intense peaks. However, if one looks at the EMCCD images, it is not until we surpass the mid-point of the S-shape in the P_{in}-P_{out} curve (e.g., green data at 625 μW), that we observe interference fringes characteristic of transitioning into the well-developed lasing regime.

From this point forward, the spectra are characterized by the strongly dominating lasing peaks and pinning of the spontaneous emission fraction. The lasing peak intensity follows a linear dependence as a function of excitation pump power (orange and maroon data points). The EMCCD images were acquired under the same exposure parameters and thus have been post-processed (for brightness) to clearly distinguish the CPP related out-coupling spots at the VG ends.

The solid red line in Figure 6-14a is a fit to the experimental data using a laser rate-equations analysis. This fit was carried out by Dr. Jorge Bravo-Abad in the group of Prof. Francisco J. García-Vidal at the UAM. In this case, we considered the CPP-like M_{VG1} mode as the input EM field for the analysis. There are two fitting parameters in the modelling, namely the coupling factor of spontaneous emission into the lasing mode (β-factor), and the reflectivity (R) of the mode at the NW end facet. We obtained values of $\beta=5.5\text{x}10^{-4}$ and

R=0.44. The latter agrees very well with the one obtained from a 3D linear EM simulation for the M_{VG1} mode (R=0.46, see Table 6.1).

It is worth mentioning that when fitting the same experimental data to the other three modes, we obtained similar values for β, but values of R that depart considerably from the ones obtained with the linear simulations (for instance, for M_{VG4} the rate-equations fit yields $\beta=4.5x10^{-4}$ and R=0.35, while full-wave simulations predict R=0.73).

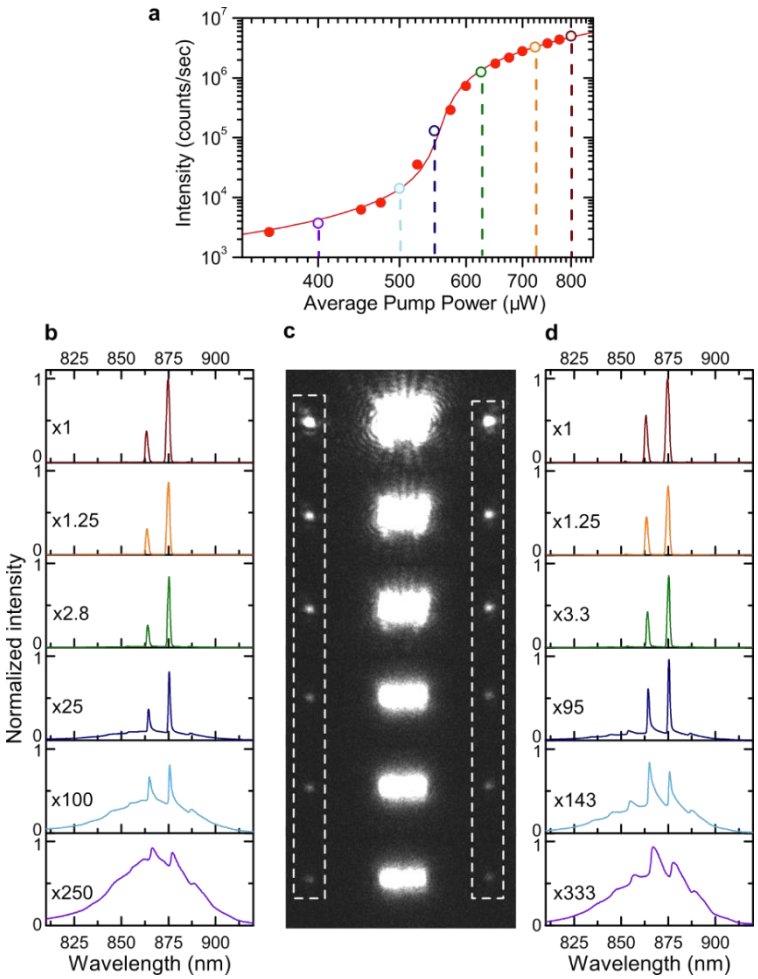

Figure 6-14 Emission sequence as a function of excitation power. a) Pin-Pout plot of the peak intensity as a function of average pump power (μW) for the dominating lasing peak of a NW-VG device. The signal was collected from the right VG end. The solid red line is a fit using laser rate-equations analysis, which yielded β=5.5 x 10-4 and R=0.44.). b&d) Normalized emission spectra collected from the left and right VG ends respectively, where the spectra are colour coded accordingly to the data points in the Pin-Pout plot. **c)** EMCCD images of the NW-VG device at the respective pump excitation power of each coloured data point. Bright spots are observed at both VG ends, from which the spectra were collected. Interference fringes appear in the images associated to the green data point and beyond (625 μW), corresponding to the spatial coherence from the NW facet´s emission in the established lasing regime.

The very good agreement between the reflectivity deduced from our rate-equations analysis and 3D simulations for the CPP-like mode, together with the experimental evidence that our system clearly couples its lasing emission into the propagating CPP modes, provide convincing arguments to confirm that we indeed observe lasing action from the M_{VG1} mode supported by the NW-VG architecture.

6.4.3 Type III NWs: No lasing inside the VGs

Reducing even more the total diameter of our NWs led to an interesting observation, that even though the NWs lased in the NW-on-metallic-film configuration, they ceased to lase in the NW-in-VG geometry. Figure 6-15 shows the typical behaviour observed for this type of NWs.

When the NW was on top of the Au film, alongside a VG, the NW did exhibit lasing emission, as seen in Figure 6-15a, which shows the spectra below (sky-blue) and above (orange) the lasing threshold. The P_{in}-P_{out} plot of the strongest lasing peak (~863 nm) is shown in Figure 6-15b, where we can distinguish the S-shape. We did notice that the threshold was at higher excitation powers when compared with the Type I and II NWs. When the NW was positioned into the VG, although we did observe coupling of the NW emission to the CPPs (Figure 6-15c), the system did not transition into the lasing regime even at much excitation powers, as can be seen in the P_{in}-P_{out} plot in Figure 6-15d.

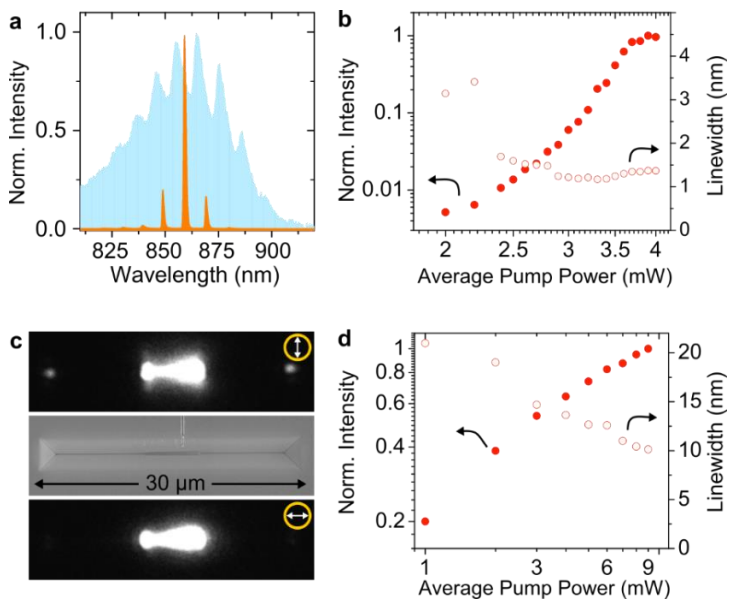

Figure 6-15 Optical characterization of a Type III NW. a) P_{in}-P_{out} of the lasing emission peak at 859 nm. Filled circles correspond to the intensity of the peak while the open circles to the linewidth. Lasing threshold is reached approximately at 3.7mW. b) Spectra of the NW outside the VG below (sky-blue) and above (orange) lasing threshold. c) P_{in}-P_{out} of a FP peak when the NW was inside the VG, no lasing was observed. d) EMCCD images with polarization collection transversal (top) and parallel (bottom) for the NW-VG device as shown in the SEM image (middle). CPP coupling of the GaAs emission is clearly appreciated.

Several devices were assembled with the Type III NWs, however with no success in achieving lasing action. To understand this behaviour, we can look at the spectra in the spontaneous emission regime (Figure 6-16), when the NWs are outside (purple) and inside (green) the VGs. We notice a clear change in the FP oscillations, with an increase in mode-spacing and broadening of the peaks, which can be attributed to a supported mode with higher losses for the case of the NW-in-VG geometry. These mode losses dominate over the gain and thus limit the NWs to enter the lasing regime under this geometry.

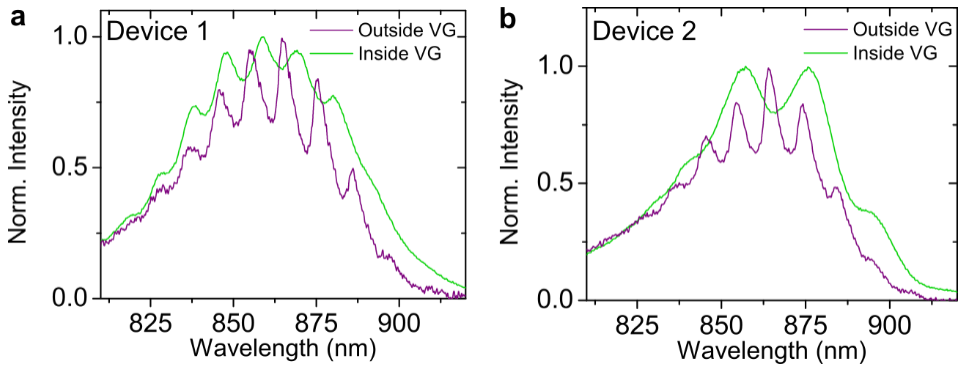

Figure 6-16 Fabry-Perot oscillations for Type III NWs in and out of a VG. a&b) Spectra of two different NWs with diameter in the range of 310 nm (Type III) at low excitation power when the NWs were placed outside the VGs (purple) and inside the VGs (green). We observe a change in the FP mode spacing when the NWs are brought inside the VG, where lasing is no longer achieved. The FP modes inside the VG suggest that the supported mode inside the VG is lossier (wider oscillations) and thus the mode gain cannot overcome the mode losses, inhibiting the lasing action.

6.5 Conclusions and Outlook

In conclusion, we introduced a new class of integrated nanolaser platform, based upon hybrid NW-VG devices operating at room temperature. To achieve this, we have combined state-of-the-art semiconducting NWs based on III-V materials, namely with a GaAs core as our gain medium, together with a new type of wafer-scale V-groove plasmonic waveguides. We showed the reproducible assembly of the hybrid systems implementing micro and nano-manipulation techniques to position individual NWs across a Au substrate and into the V-groove channels.

Thorough evidence of the lasing emission and coupling to the CPPs supported by the VGs was provided by means of photoluminescence experiments upon pulsed excitation of the NWs. NWs with diameters roughly above 370 nm are able to lase both on top of the Au film and inside the VGs, with the coupled CPP signals exhibiting strong polarization anisotropy. Theoretical simulations shed light on the supported modes by the hybrid NW-VG geometry and provide supporting data that a hybrid CPP-like mode in the NW-VG geometry enables the observed lasing behaviour in our devices. The estimated experimental transfer efficiency for the energy exiting the NW facets into the VG CPP mode of nearly

10% sets a new standard in terms of lasing coupling from a nanolaser to an on-chip subwavelength waveguide.

Strictly speaking, ours is not the first observation of a NW laser coupled to a plasmonic waveguide, since coupling of a CdSe NW laser to colloidal silver NWs has been recently reported.[150] However, the silver NWs in that report acted just as one of the output channels for the photonic lasing mode of the CdSe NW, while in our case we truly have a hybrid photonic-plasmonic mode responsible for the lasing. Furthermore, our hybrid structure represents a first of its kind, in the sense that it involves a custom designed plasmonic circuit that is wafer-scale compatible, as opposed to randomly deposited colloidal nanowire plasmonic waveguides.

Our platform provides facile launching and routing of laser emission into the plasmonic waveguides with a distinct polarization state. Currently, our system relies on the free-space excitation of the NW inside the VG, nevertheless, this can eventually circumvent by implementing electrical injection-based pumping of the gain medium. Previous works on similar NW heterostructures should make the latter feasible.[36,155]

We envision that the open-channel nature and EM field confinement of the CPPs will provide the means to build high-sensitivity chemical or bio-sensing platforms with an integrated nanolaser source.[156] The type of hybrid system we demonstrate in this work is not limited to lasing NWs, but can be extended to more complex NW heterostructures with either embedded single photon sources (as in Chapter 4) or p-n junctions to have a multifunctional device integrated within the same waveguiding element. Additionally, the NWs can be integrated with other elements along the VG to build functional photonic circuitry, for example in quantum optics experiments employing single quantum emitters coupled to the CPPs (such as colloidal QDs and defect centres),[15,143] or integrating electro-optic elements in high-speed plasmonic modulators for data communication.[32,33]

Future directions should focus on the development of electrical injection based waveguide integrated NW lasers, with previous efforts indicating this is feasible.[36,155,157] This, combined with integrated modulators and photodetectors, could bring us a step closer to optics-less hybrid photonic-plasmonic circuit platforms.

Chapter 7: Conclusions and Outlook

The results presented in this thesis contribute to the ongoing developments of potential hybrid photonic-plasmonic platforms applicable in future integrated photonic chip technologies. Hybrid systems combining solid-state nanoscale light sources with plasmonic structures are capable of enhancing the emission dynamics of the emitters and channelling the energy into subwavelength confined modes. In this thesis, we demonstrated a number of hybrid photonic-plasmonic systems by deterministically integrating individual nanoscale light emitters with on-chip plasmonic structures.

State of the art nanopositioning techniques were implemented to bring the emitters within the regions of enhanced light-matter interactions (i.e., the near-fields of the supported modes) provided by the plasmonic architectures. We exploited fluorescence microscopy techniques such as confocal imaging, emission lifetime measurements and wide-field imaging to reveal the manifestation of the emission coupling from the emitters to the modes supported by the plasmonic structures.

Semiconductor colloidal quantum dots were positioned at the hotspot regions of disc and disc dimer gap antennas to study the excitation enhancement offered by these structures. The QD-antenna devices were assembled by means of a combined electron beam lithography and chemical functionalization positioning technique.

Nanodiamond particles containing single Nitrogen Vacancy defect centres where positioned inside narrow V-shaped plasmonic waveguides by means of a scanning probe nanopositioning technique, which allowed us to demonstrate for the first time the coupling of a single quantum emitter to this class of promising plasmonic waveguides.

Semiconducting nanowires (NWs) containing recently developed self-assembled quantum dots, were positioned by means of micro- and nano-positioners, inside wafer-scale compatible V-groove (VG) plasmonic waveguides. We were able to demonstrate for the first time the coupling of these embedded emitters to the propagating modes supported by the VG waveguides.

Finally, under a similar configuration of a nanowire and VG device, but utilizing core-shell-cap semiconducting nanowire lasers, we demonstrated a plasmonic waveguide integrated nanowire laser platform with unprecedented performance in the transfer of energy from the hybrid NW-VG mode to the propagating sub-wavelength confined mode of the waveguide.

The different platforms presented in this work contribute to the efforts of developing and understanding how hybrid photonic-plasmonic systems can control light emission from nanoscale emitters. Certainly, there is still plenty of room for improvements within the systems presented here as well as in other novel hybrid configurations. For example, future work could study the plasmon mode mediated interaction between individual quantum emitters deterministically positioned within the same plasmonic V-groove. A major challenge in this type of configurations is the deterministic alignment of the emitters' associated dipole moment. A potential solution could exploit particle trapping techniques in order to orient the particles prior to the positioning within the waveguide.[158]

In terms of plasmonic waveguide coupled emitters, it will be interesting to see progress in the integration of other photonic elements along the same waveguide. For example to include modulator and detectors, so that ideally, together with electrically driven single emitters and nanolasers, all the desired functionalities are integrated within the same device.

As the field of nanophotonics progresses and the demand for compact and powerful integrated photonic circuits increases, hybrid systems combining solid-state nanoscale light sources with plasmonic structures will play an important role in the quest for next-generation integrated photonic circuits. These systems can potentially become part of the building blocks in future quantum communication and computation technologies, as well as highly sensitive monitoring platforms.

In this context, this thesis provides an important contribution to this cause and hopefully can guide or motivate future work in this exciting area of photonics science and technology.

Bibliography

(1) Koenderink, A. F.; Alù, A.; Polman, A. *Science* **2015**, *348* (6234), 516–521.

(2) Eisaman, M. D.; Fan, J.; Migdall, A.; Polyakov, S. V. *Rev. Sci. Instrum.* **2011**, *82* (7), 71101.

(3) Aharonovich, I.; Englund, D.; Toth, M. *Nat. Photon.* **2016**, *10* (10), 631–641.

(4) Hill, M. T.; Gather, M. C. *Nat. Photonics* **2014**, *8* (12), 908–918.

(5) Pelton, M. *Nat. Photonics* **2015**, *9* (7), 427–435.

(6) Barnes, W. L.; Dereux, A.; Ebbesen, T. W. *Nature* **2003**, *424* (6950), 824–830.

(7) Zayats, A. V; Smolyaninov, I. I. *J. Opt. A-Pure Appl. Opt.* **2003**, *5*, S16–S50.

(8) Gramotnev, D. K.; Bozhevolnyi, S. I. *Nat Phot.* **2010**, *4* (2), 83–91.

(9) Wang, X.; Zhan, S.; Huang, Z.; Hong, X. *Instrum. Sci. Technol.* **2013**, *41* (6), 574–607.

(10) Benson, O. *Nature* **2011**, *480* (7376), 193–199.

(11) Tame, M. S.; McEnery, K. R.; Ozdemir, S. K.; Lee, J.; Maier, S. A.; Kim, M. S. *Nat Phys* **2013**, *9* (6), 329–340.

(12) Chang, D. E.; Sørensen, A.; Hemmer, P.; Lukin, M. *Phys. Rev. B* **2007**, *76* (3), 35420.

(13) Hümmer, T.; García-Vidal, F. J.; Martín-Moreno, L.; Zueco, D. *Phys. Rev. B* **2013**, *87* (11), 115419.

(14) Törmä, P.; Barnes, W. L. *Reports Prog. Phys.* **2015**, *78* (1), 13901.

(15) Gonzalez-Tudela, A.; Martin-Cano, D.; Moreno, E.; Martin-Moreno, L.; Tejedor, C.; Garcia-Vidal, F. J. *Phys. Rev. Lett.* **2011**, *106* (2), 20501.

(16) Chen, G.-Y.; Lambert, N.; Chou, C.-H.; Chen, Y.-N.; Nori, F. *Phys. Rev. B* **2011**, *84* (4), 45310.

(17) Gullans, M.; Tiecke, T. G.; Chang, D. E.; Feist, J.; Thompson, J. D.; Cirac, J. I.; Zoller, P.; Lukin, M. D. *Phys. Rev. Lett.* **2012**, *109* (23), 235309.

(18) Lee, C.; Tame, M.; Noh, C.; Lim, J.; Maier, S. A.; Lee, J.; Angelakis, D. G. *New J. Phys.* **2013**, *15* (8), 83017.

(19) Kimble, H. J. *Nature* **2008**, *453* (7198), 1023–1030.

(20) Akimov, A. V; Mukherjee, A.; Yu, C. L.; Chang, D. E.; Zibrov, A. S.; Hemmer, P. R.; Park, H.; Lukin, M. D. *Nature* **2007**, *450* (7168), 402–406.

(21) Tame, M. S.; Lee, C.; Lee, J.; Ballester, D.; Paternostro, M.; Zayats, A. V.; Kim, M. S. *Phys. Rev. Lett.* **2008**, *101* (19), 1–4.

(22) Kumar, S.; Kristiansen, N. I.; Huck, A.; Andersen, U. L. *Nano Lett.* **2014**, *14* (2), 663–669.

(23) Rewitz, C.; Razinskas, G.; Geisler, P.; Krauss, E.; Goetz, S.; Pawłowska, M.; Hecht, B.; Brixner, T. *Phys. Rev. Appl.* **2014**, *1* (1), 14007.

(24) Chang, D. E.; Sørensen, A. S.; Demler, E. a.; Lukin, M. D. *Nat. Phys.* **2007**, *3* (11), 807–812.

(25) Heeres, R. W.; Kouwenhoven, L. P.; Zwiller, V. *Nat. Nanotechnol.* **2013**, *8* (10), 719–722.

(26) Sun, C.; Wade, M. T.; Lee, Y.; Orcutt, J. S.; Alloatti, L.; Georgas, M. S.; Waterman, A. S.; Shainline, J. M.; Avizienis, R. R.; Lin, S.; Moss, B. R.; Kumar, R.; Pavanello, F.; Atabaki, A. H.;

Cook, H. M.; Ou, A. J.; Leu, J. C.; Chen, Y.-H.; Asanović, K.; Ram, R. J.; Popović, M. A.; Stojanović, V. M. *Nature* **2015**, *528* (7583), 534–538.

(27) Novotny, L.; van Hulst, N. *Nat. Photon.* **2011**, *5* (2), 83–90.

(28) Fang, Y.; Sun, M. *Light Sci. Appl.* **2015**, *4* (e294), 1–11.

(29) Kolesov, R.; Grotz, B.; Balasubramanian, G.; Stohr, R. J.; Nicolet, A. A. L.; Hemmer, P. R.; Jelezko, F.; Wrachtrup, J. *Nat Phys* **2009**, *5* (7), 470–474.

(30) Martin-Cano, D.; Gonzlez-Tudela, A.; Martin-Moreno, L.; Garcia-Vidal, F. J.; Tejedor, C.; Moreno, E.; Martín-Cano, D.; González-Tudela, A.; Martín-Moreno, L.; García-Vidal, F. J.; Tejedor, C.; Moreno, E. *Phys. Rev. B - Condens. Matter Mater. Phys.* **2011**, *84* (23), 235306.

(31) Krasavin, A. V.; Vo, T. P.; Dickson, W.; Bolger, P. M.; Zayats, A. V. *Nano Lett.* **2011**, *11* (6), 2231–2235.

(32) Melikyan, A.; Alloatti, L.; Muslija, A.; Hillerkuss, D.; Schindler, P. C.; Li, J.; Palmer, R.; Korn, D.; Muehlbrandt, S.; Van Thourhout, D.; Chen, B.; Dinu, R.; Sommer, M.; Koos, C.; Kohl, M.; Freude, W.; Leuthold, J. *Nat. Photon.* **2014**, *8* (3), 229–233.

(33) Haffner, C.; Heni, W.; Fedoryshyn, Y.; Niegemann, J.; Melikyan, A.; Elder, D. L.; Baeuerle, B.; Salamin, Y.; Josten, A.; Koch, U.; Hoessbacher, C.; Ducry, F.; Juchli, L.; Emboras, A.; Hillerkuss, D.; Kohl, M.; Dalton, L. R.; Hafner, C.; Leuthold, J. *Nat. Photon.* **2015**, *9* (8), 525–528.

(34) Heeres, R. W.; Dorenbos, S. N.; Koene, B.; Solomon, G. S.; Kouwenhoven, L. P.; Zwiller, V. *Nano Lett.* **2010**, *10* (2), 661–664.

(35) Falk, A. L.; Koppens, F. H. L.; Yu, C. L.; Kang, K.; de Leon Snapp, N.; Akimov, A. V; Jo, M.-H.; Lukin, M. D.; Park, H. *Nat Phys* **2009**, *5* (7), 475–479.

(36) Fan, P.; Colombo, C.; Huang, K. C. Y.; Krogstrup, P.; Nygård, J.; Fontcuberta I Morral, A.; Brongersma, M. L. *Nano Lett.* **2012**, *12* (9), 4943–4947.

(37) Curto, A. G.; Volpe, G.; Taminiau, T. H.; Kreuzer, M. P.; Quidant, R.; van Hulst, N. F. *Science* **2010**, *329* (5994), 930–933.

(38) Huck, A.; Kumar, S.; Shakoor, A.; Andersen, U. L. *Phys. Rev. Lett.* **2011**, *106* (9).

(39) Ropp, C.; Cummins, Z.; Nah, S.; Fourkas, J. T.; Shapiro, B.; Waks, E. *Nat Commun* **2013**, *4*, 1447.

(40) Barth, M.; Schietinger, S.; Schröder, T.; Aichele, T.; Benson, O. *J. Lumin.* **2010**, *130* (9), 1628–1634.

(41) Casadei, A.; Pecora, E. F.; Trevino, J.; Forestiere, C.; R??ffer, D.; Russo-Averchi, E.; Matteini, F.; Tutuncuoglu, G.; Heiss, M.; Fontcuberta I Morral, A.; Dal Negro, L. *Nano Lett.* **2014**, *14* (5), 2271–2278.

(42) Kress, S. J. P.; Antolinez, F. V; Richner, P.; Jayanti, S. V; Kim, D. K.; Prins, F.; Riedinger, A.; Fischer, M. P. C.; Meyer, S.; McPeak, K. M.; Poulikakos, D.; Norris, D. J. *Nano Lett.* **2015**, *15* (9), 6267–6275.

(43) Roth, F.; König, A.; Fink, J.; Büchner, B.; Knupfer, M. *J. Electron Spectros. Relat. Phenomena* **2014**, *195*, 85–95.

(44) Johnson, P. B.; Christy, R. W. *Phys. Rev. B* **1972**, *6*, 4370–4379.

(45) Otto, A. *Zeitschrift für Phys. A Hadron. Nucl.* **1968**, *216* (4), 398–410.

(46) Kretschmann, E.; Raether, H. *Zeitschrift fur Naturforsch. - Sect. A J. Phys. Sci.* **1968**, *23* (12), 2135–2136.

(47) Ritchie, R. H.; Arakawa, E. T.; Cowan, J. J.; Hamm, R. N. *Phys. Rev. Lett.* **1968**, *21* (22), 1530–1533.

(48) Hecht, B.; Bielefeldt, H.; Novotny, L.; Inouye, Y.; Pohl, D. W. *Phys. Rev. Lett.* **1996**, *77* (9), 1889–1892.

(49) Fischer, U. C.; Pohl, D. W. *Phys. Rev. Lett.* **1989**, *62* (4), 458–461.

(50) Ebbesen, T. W.; Genet, C.; Bozhevolnyi, S. I. *Phys. Today* **2008**, *61* (5), 44–50.

(51) Sorger, V. J.; Oulton, R. F.; Ma, R.-M.; Zhang, X. *MRS Bull.* **2012**, *37* (8), 728–738.

(52) Pile, D. F. P.; Gramotnev, D. K. *Opt. Lett.* **2004**, *29* (10), 1069–1071.

(53) Bozhevolnyi, S. I.; Nerkararyan, K. V. *Opt. Lett.* **2009**, *34* (13), 2039–2041.

(54) Smith, C. L. C.; Stenger, N.; Kristensen, A.; Mortensen, N. A.; Bozhevolnyi, S. I. *Nanoscale* **2015**, *7*, 9355–9386.

(55) Bozhevolnyi, S. I.; Volkov, V. S.; Devaux, E.; Laluet, J.-Y.; Ebbesen, T. W. *Nature* **2006**, *440* (7083), 508–511.

(56) Smith, C. L. C.; Thilsted, A. H.; Garcia-Ortiz, C. E.; Radko, I. P.; Marie, R.; Jeppesen, C.; Vannahme, C.; Bozhevolnyi, S. I.; Kristensen, A. *Nano Lett.* **2014**, *14* (3), 1659–1664.

(57) Volkov, V. S.; Bozhevolnyi, S. I.; Rodrigo, S. G.; Martín-Moreno, L.; García-Vidal, F. J.; Devaux, E.; Ebbesen, T. W. *Nano Lett.* **2009**, *9* (3), 1278–1282.

(58) Burgos, S. P.; Lee, H. W.; Feigenbaum, E.; Briggs, R. M.; Atwater, H. A. *Nano Lett.* **2014**, *14* (6), 3284–3292.

(59) Søndergaard, T.; Bozhevolnyi, S. I.; Novikov, S. M.; Beermann, J.; Devaux, E.; Ebbesen, T. W. *Nano Lett.* **2010**, *10* (8), 3123–3128.

(60) Søndergaard, T.; Novikov, S. M.; Holmgaard, T.; Eriksen, R. L.; Beermann, J.; Han, Z.; Pedersen, K.; Bozhevolnyi, S. I. *Nat. Commun.* **2012**, *3*, 969.

(61) Anker, J. N.; Hall, W. P.; Lyandres, O.; Shah, N. C.; Zhao, J.; Van Duyne, R. P. *Nat. Mater.* **2008**, *7* (6), 442–453.

(62) Scheel, S. *J. Mod. Opt.* **2009**, *56* (2–3), 141–160.

(63) Shirasaki, Y.; Supran, G. J.; Bawendi, M. G.; Bulović, V. *Nat. Photon.* **2013**, *7* (1), 13–23.

(64) Gaponik, N.; Hickey, S. G.; Dorfs, D.; Rogach, A. L.; Eychmüller, A. *Small* **2010**, *6* (13), 1364–1378.

(65) Kim, J. Y.; Voznyy, O.; Zhitomirsky, D.; Sargent, E. H. *Adv. Mater.* **2013**, *25* (36), 4986–5010.

(66) Ji, B.; Giovanelli, E.; Habert, B.; Spinicelli, P.; Nasilowski, M.; Xu, X.; Lequeux, N.; Hugonin, J.-P.; Marquier, F.; Greffet, J.-J.; Dubertret, B. *Nat. Nanotechnol.* **2015**, *10*, 1–6.

(67) Muskens, O. L.; Giannini, V.; Sánchez-Gil, J. A.; Gómez Rivas, J. *Nano Lett.* **2007**, *7* (9), 2871–2875.

(68) Shields, A. J.; Limited, E.; Park, C. S. *Nat Phot.* **2007**, *1* (4), 215–223.

(69) Wang, Z. M. *Self-assembled Quantum Dots*, 1st ed.; Wang, Z. M., Ed.; Springer-Verlag New York: New York, 2008.

(70) Tatebayashi, J.; Ota, Y.; Ishida, S.; Nishioka, M.; Iwamoto, S.; Arakawa, Y.; Tatebayashi, J.; Ota, Y.; Ishida, S.; Nishioka, M.; Iwamoto, S.; Arakawa, Y. **2016**, *263101* (2012), 1–5.

(71) Borgström, M. T.; Zwiller, V.; Müller, E.; Imamoglu, A.; Borgstro, M. T.; Zwiller, V.; Mu, E. *Nano Lett.* **2005**, *5* (7), 1439–1443.

(72) Reimer, M. E.; Bulgarini, G.; Akopian, N.; Hocevar, M.; Bavinck, M. B.; Verheijen, M. A.; Bakkers, E. P. A. M.; Kouwenhoven, L. P.; Zwiller, V. **2012**.

(73) Heiss, M.; Fontana, Y.; Gustafsson, A.; Wüst, G.; Magen, C.; O'Regan, D. D.; Luo, J. W.; Ketterer, B.; Conesa-Boj, S.; Kuhlmann, a V; Houel, J.; Russo-Averchi, E.; Morante, J. R.; Cantoni, M.; Marzari, N.; Arbiol, J.; Zunger, A.; Warburton, R. J.; Fontcuberta i Morral, A. *Nat. Mater.* **2013**, *12* (5), 439–444.

(74) Jeon, N.; Loitsch, B.; Morkoetter, S.; Abstreiter, G.; Finley, J.; Krenner, H. J.; Koblmueller, G.; Lauhon, L. J. *ACS Nano* **2015**, *9* (8), 8335–8343.

(75) Francaviglia, L.; Fontana, Y.; Conesa-Boj, S.; Tutuncuoglu, G.; Duchene, L.; Tanasescu, M. B.; Matteini, F.; Fontcuberta I Morral, A. *Appl. Phys. Lett.* **2015**, *33106*, 2–5.

(76) Doherty, M. W.; Manson, N. B.; Delaney, P.; Jelezko, F.; Wrachtrup, J.; Hollenberg, L. C. L. *Phys. Rep.* **2013**, *528* (1), 1–45.

(77) Pezzagna, S.; Rogalla, D.; Wildanger, D.; Meijer, J.; Zaitsev, A. *New J. Phys.* **2011**, *13*.

(78) Orwa, J. O.; Greentree, A. D.; Aharonovich, I.; Alves, A. D. C.; Van Donkelaar, J.; Stacey, A.; Prawer, S. *J. Lumin.* **2010**, *130* (9), 1646–1654.

(79) Jelezko, F.; Wrachtrup, J. *Phys. Status Solidi Appl. Mater. Sci.* **2006**, *203* (13), 3207–3225.

(80) Mohtashami, A.; Femius Koenderink, A. *New J. Phys.* **2013**, *15*, 43017.

(81) Huang, M. H. *Science* **2001**, *292* (5523), 1897–1899.

(82) Johnson, J. C.; Choi, H.-J.; Knutsen, K. P.; Schaller, R. D.; Yang, P.; Saykally, R. J. *Nat. Mater.* **2002**, *1* (2), 106–110.

(83) Samuel, I. D. W.; Namdas, E. B.; Turnbull, G. a. *Nat. Photon.* **2009**, *3* (10), 546–549.

(84) Van Vugt, L. K.; Ruhle, S.; Vanmaekelbergh, D. *Nano Lett.* **2006**, *6* (12), 2707–2711.

(85) Zimmler, M. A.; Bao, J.; Capasso, F.; Müller, S.; Ronning, C. *Appl. Phys. Lett.* **2008**, *93* (5), 3–5.

(86) Couteau, C.; Larrue, A.; Wilhelm, C.; Soci, C. *Nanophotonics* **2015**, *4*, 90–107.

(87) Eaton, S.; Fu, A.; Wong, A.; Ning, C.; P. Yang. *Nat. Rev. Mater.* **2016**, *1* (1), 1–11.

(88) Roy Szweda. *Gallium Arsenide Electronic Materials and Devices*; Elsevier, 2000.

(89) Saxena, D.; Mokkapati, S.; Parkinson, P.; Jiang, N.; Gao, Q.; Tan, H. H.; Jagadish, C. *Nat Phot.* **2013**, *7* (12), 963–968.

(90) Mayer, B.; Rudolph, D.; Schnell, J.; Morkötter, S.; Winnerl, J.; Treu, J.; Müller, K.; Bracher, G.; Abstreiter, G.; Koblmüller, G.; Finley, J. J. *Nat. Commun.* **2013**, *4*, 2931.

(91) Mayer, B.; Janker, L.; Rudolph, D.; Loitsch, B.; Kostenbader, T.; Abstreiter, G.; Koblmüller, G.; Finley, J. J. *Appl. Phys. Lett.* **2016**, *108* (7), 7–12.

(92) Mayer, B.; Janker, L.; Loitsch, B.; Treu, J.; Kostenbader, T.; Lichtmannecker, S.; Reichert, T.; Morkötter, S.; Kaniber, M.; Abstreiter, G.; Gies, C.; Koblmüller, G.; Finley, J. J. *Nano Lett.* **2016**, *16* (1), 152–156.

(93) Burgess, T.; Saxena, D.; Mokkapati, S.; Li, Z.; Hall, C. R.; Davis, J. A.; Wang, Y.; Smith, L. M.; Fu, L.; Caroff, P.; Tan, H. H.; Jagadish, C. *Nat Commun* **2016**, *7*, 11927.

(94) Saxena, D.; Jiang, N.; Yuan, X.; Mokkapati, S.; Guo, Y.; Tan, H. H.; Jagadish, C. *Nano Lett.* **2016**,

16 (8), 5080–5086.

(95) Ho, J.; Tatebayashi, J.; Sergent, S.; Fong, C. F.; Iwamoto, S.; Arakawa, Y. *ACS Photonics* **2015**, *2* (1), 165–171.

(96) Ho, J.; Tatebayashi, J.; Sergent, S.; Fong, C. F.; Ota, Y.; Iwamoto, S.; Arakawa, Y. *Nano Lett.* **2016**, *16* (4), 2845–2850.

(97) Tatebayashi, J.; Kako, S.; Ho, J.; Ota, Y.; Iwamoto, S.; Arakawa, Y. *Nat. Photon.* **2015**, *9* (8), 501–505.

(98) Geiselmann, M.; Juan, M. L.; Renger, J.; Say, J. M.; Brown, L. J.; de Abajo, F. J. G.; Koppens, F.; Quidant, R. *Nat. Nanotechnol.* **2013**, *8* (3), 175–179.

(99) Pfaff, W.; Vos, A.; Hanson, R. *J. Appl. Phys.* **2013**, *113* (2), 24310.

(100) Dregely, D.; Lindfors, K.; Dorfmüller, J.; Hentschel, M.; Becker, M.; Wrachtrup, J.; Lippitz, M.; Vogelgesang, R.; Giessen, H. *Phys. Status Solidi* **2012**, *249* (4), 666–677.

(101) Dregely, D.; Lindfors, K.; Lippitz, M.; Engheta, N.; Totzeck, M.; Giessen, H. *Nat. Commun.* **2014**, *5*, 4354.

(102) Schietinger, S.; Barth, M.; Aichele, T.; Benson, O. *Nano Lett.* **2009**, *9* (4), 1694–1698.

(103) Schell, A. W.; Kewes, G.; Hanke, T.; Leitenstorfer, A.; Bratschitsch, R.; Benson, O.; Aichele, T. *Opt. Express* **2011**, *19* (8), 7914–7920.

(104) Van Der Sar, T.; Heeres, E. C.; Dmochowski, G. M.; De Lange, G.; Robledo, L.; Oosterkamp, T. H.; Hanson, R. *Appl. Phys. Lett.* **2009**, *94* (17), 3–5.

(105) Munechika, K.; Chen, Y.; Tillack, A. F.; Kulkarni, A. P.; Plante, I. J. La; Munro, A. M.; Ginger, D. S. *Nano Lett.* **2010**, *10* (7), 2598–2603.

(106) Kulakovich, O.; Strekal, N.; Yaroshevich, A.; Maskevich, S.; Gaponenko, S.; Nabiev, I.; Woggon, U.; Artemyev, M. *Nano Lett.* **2002**, *2* (12), 1449–1452.

(107) Aouani, H.; Itzhakov, S.; Gachet, D.; Devaux, E.; Ebbesen, T. W.; Rigneault, H.; Oron, D.; Wenger, J. *ACS Nano* **2010**, *4* (8), 4571–4578.

(108) Ratchford, D.; Shafiei, F.; Kim, S.; Gray, S. K.; Li, X. *Nano Lett* **2011**, *11* (3), 1049–1054.

(109) Pons, T.; Medintz, I. L.; Sapsford, K. E.; Higashiya, S.; Grimes, A. F.; English, D. S.; Mattoussi, H. *Nano Lett.* **2007**, *7* (10), 3157–3164.

(110) Curto, A. G.; Taminiau, T. H.; Volpe, G.; Kreuzer, M. P.; Quidant, R.; van Hulst, N. F. *Nat. Commun.* **2013**, *4*, 1750.

(111) Gruber, C.; Kusar, P.; Hohenau, A.; Krenn, J. R. *Appl. Phys. Lett.* **2012**, *100* (23), 231102.

(112) Fulmes, J.; Jäger, R.; Bräuer, A.; Schäfer, C.; Jäger, S.; Gollmer, D. A.; Horrer, A.; Nadler, E.; Chassé, T.; Zhang, D.; Meixner, A. J.; Kern, D. P.; Fleischer, M. *Nanoscale* **2015**, *7* (35), 14691–14696.

(113) Bermúdez-Ureña, E.; Kreuzer, M. P.; Itzhakov, S.; Rigneault, H.; Quidant, R.; Oron, D.; Wenger, J. *Adv. Mater.* **2012**, *24* (44), 314–320.

(114) Klimov, V. I. *Annu. Rev. Phys. Chem.* **2007**, *58*, 635–673.

(115) Fisher, B.; Caruge, J. M.; Zehnder, D.; Bawendi, M. *Phys. Rev. Lett.* **2005**, *94* (8), 1–4.

(116) Jin, S.; Song, N.; Lian, T. *ACS Nano* **2010**, *4* (3), 1545–1552.

(117) Fisher, B.; Caruge, J. M.; Chan, Y. T.; Halpert, J.; Bawendi, M. G. *Chem. Phys.* **2005**, *318* (1–2),

71–81.

(118) Huang, C.; Bouhelier, A.; Colas Des Francs, G.; Bruyant, A.; Guenot, A.; Finot, E.; Weeber, J. C.; Dereux, A. *Phys. Rev. B - Condens. Matter Mater. Phys.* **2008**, *78* (15), 1–7.

(119) Rabouw, F. T.; Frimmer, M.; Mohtashami, A.; Koenderink, A. F. *Opt. Mater. (Amst).* **2013**, *35* (7), 1342–1347.

(120) Macintyre, D. S.; Ignatova, O.; Thoms, S.; Thayne, I. G. *J. Vac. Sci. Technol. B* **2009**, *27* (6), 2597–2601.

(121) Gaebel, T.; Domhan, M.; Popa, I.; Wittmann, C.; Neumann, P.; Jelezko, F.; Rabeau, J. R.; Stavrias, N.; Greentree, A. D.; Prawer, S.; Meijer, J.; Twamley, J.; Hemmer, P. R.; Wrachtrup, J. *Nat Phys* **2006**, *2* (6), 408–413.

(122) Bernien, H.; Hensen, B.; Pfaff, W.; Koolstra, G.; Blok, M. S.; Robledo, L.; Taminiau, T. H.; Markham, M.; Twitchen, D. J.; Childress, L.; Hanson, R. *Nature* **2013**, *497* (7447), 86–90.

(123) Huck, A.; Andersen, U. L. *Nanophotonics* **2016**, 1–14.

(124) Kumar, S.; Huck, A.; Andersen, U. L. *Nano Lett.* **2013**, *13* (3), 1221–1225.

(125) Kusar, P.; Gruber, C.; Hohenau, A.; Krenn, J. R. *Nano Lett.* **2012**, *12* (2), 661–665.

(126) Alaverdyan, Y.; Vamivakas, N.; Barnes, J.; Lebouteiller, C.; Hare, J.; Atatüre, M. *Opt. Express* **2011**, *19* (19), 18175–18181.

(127) Moreno, E.; Rodrigo, S. G.; Bozhevolnyi, S. I.; Martín-Moreno, L.; García-Vidal, F. J. *Phys. Rev. Lett.* **2008**, *100* (2), 23901.

(128) Martín-Cano, D.; Martín-Moreno, L.; García-Vidal, F. J.; Moreno, E. *Nano Lett.* **2010**, *10* (8), 3129–3134.

(129) Vial, A.; Grimault, A.-S.; Macías, D.; Barchiesi, D.; de la Chapelle, M. *Phys. Rev. B* **2005**, *71* (8), 85416.

(130) Anger, P.; Bharadwaj, P.; Novotny, L. *Phys. Rev. Lett.* **2006**, *96* (11), 113002.

(131) Kühn, S.; Håkanson, U.; Rogobete, L.; Sandoghdar, V. *Phys. Rev. Lett.* **2006**, *97* (1), 17402.

(132) Brown, R. H.; Twiss, R. Q. *Nature* **1956**, *177* (4497), 27–29.

(133) Inam, F. A.; Grogan, M. D. W.; Rollings, M.; Gaebel, T.; Say, J. M.; Bradac, C.; Birks, T. A.; Wadsworth, W. J.; Castelletto, S.; Rabeau, J. R.; Steel, M. J. *ACS Nano* **2013**, *7* (5), 3833–3843.

(134) Mohamed, M. B.; Volkov, V.; Link, S.; El-Sayed, M. A. *Chem. Phys. Lett.* **2000**, *317* (6), 517–523.

(135) Barthes, J.; Bouhelier, A.; Dereux, A.; Francs, G. C. des. *Sci. Rep.* **2013**, *3*.

(136) Neu, E.; Steinmetz, D.; Riedrich-Möller, J.; Gsell, S.; Fischer, M.; Schreck, M.; Becher, C. *New J. Phys.* **2011**, *13* (2), 25012.

(137) Qian, Y.; Zhu, Z. H.; Lo, Y. H.; Huffaker, D. L.; Deppe, D. G.; Hou, H. Q.; Hammons, B. E.; Lin, W.; Tu, Y. K. *Appl. Phys. Lett.* **1997**, *71* (1), 25.

(138) Moreau, E.; Robert, I.; Manin, L.; Gã, J. M.; Abram, I. **2002**, *13*, 418–422.

(139) Malik, N. S.; Bazin, M.; Gregersen, N.; Sauvan, C.; Lalanne, P.; Ge, J.; Claudon, J.; Bleuse, J.; Malik, N. S.; Bazin, M.; Jaffrennou, P.; Gregersen, N.; Sauvan, C.; Lalanne, P.; Gérard, J.-M. *Nat. Photon.* **2010**, *4* (3), 174–177.

(140) Dalacu, D.; Mnaymneh, K.; Lapointe, J.; Wu, X.; Poole, P. J.; Bulgarini, G.; Zwiller, V.; Reimer, M. E. **2012**.

(141) Minot, E. D.; Kelkensberg, F.; Kouwen, M. Van; Dam, J. A. Van; Kouwenhoven, L. P.; Zwiller, V.; Borgstro, M. T.; Verheijen, M. A.; Bakkers, E. P. A. M. **2007**.

(142) Zadeh, I. E.; Elshaari, A. W.; Jo, K. D.; Fognini, A.; Dalacu, D.; Poole, P. J.; Reimer, M. E.; Zwiller, V. **2016**.

(143) Bermúdez-Ureña, E.; Gonzalez-Ballestero, C.; Geiselmann, M.; Radko, I. P.; Holmgaard, T.; Alaverdyan, Y.; Moreno, E.; Bozhevolnyi, S. I.; Quidant, R. *Nat. Commun.* **2015**, *6*, 7883.

(144) Mancini, L.; Fontana, Y.; Blum, I.; Vurpillot, F.; Francaviglia, L.; Heiss, M.; Arbiol, J.; Rigutti, L. **2014**, *243106*, 12–16.

(145) Smit, M.; Leijtens, X.; Ambrosius, H.; Bente, E.; Tol, J. van der; Smalbrugge, B.; Vries, T. de; Geluk, E.-J.; Bolk, J.; Veldhoven, R. van; Augustin, L.; Thijs, P.; Domenico D'Agostino; Rabbani, H.; Lawniczuk, K.; Stopinski, S.; Tahvili, S.; Corradi, A.; Emil Kleijn; Dzibrou, D.; Felicetti, M.; Bitincka, E.; Moskalenko, V.; Zhao, J.; Rui Santos; Gilardi, G.; Yao, W.; Williams, K.; Stabile, P.; Kuindersma, P.; Josselin Pello; Bhat, S.; Jiao, Y.; Heiss, D.; Roelkens, G.; Wale, M.; Firth, P.; Francisco Soares; Grote, N.; Schell, M.; Debregeas, H.; Achouche, M.; Gentner, J.-L.; Arjen Bakker; Korthorst, T.; Gallagher, D.; Dabbs, A.; Melloni, A.; Morichetti, F.; Daniele Melati; Wonfor, A.; Penty, R.; Broeke, R.; Musk, B.; Robbins, D. *Semicond. Sci. Technol.* **2014**, *29* (8), 83001.

(146) Yan, R.; Gargas, D.; Yang, P. *Nat Phot.* **2009**, *3* (10), 569–576.

(147) Bermúdez-Ureña, E.; Tutuncuoglu, G.; Cuerda, J.; Smith, C. L. C.; Bravo-Abad, J.; Bozhevolnyi, S. I.; Fontcuberta i Morral, A.; García-Vidal, F. J.; Quidant, R. *Nano Lett.* **2017**, *17* (2), 747–754.

(148) Robert G. Hunsperger. *Integrated Optics: Theory and Technology*, 6th ed.; Springer-Verlag New York, 2009.

(149) McPolin, C. P. T.; Bouillard, J.-S.; Vilain, S.; Krasavin, A. V.; Dickson, W.; O'Connor, D.; Wurtz, G. A.; Justice, J.; Corbett, B.; Zayats, A. V. *Nat. Commun.* **2016**, *7*, 12409.

(150) Wu, X.; Xiao, Y.; Meng, C.; Zhang, X.; Yu, S.; Wang, Y.; Yang, C.; Guo, X.; Ning, C. Z.; Tong, L. *Nano Lett.* **2013**, *13* (11), 5654–5659.

(151) Li, Y. J.; Lv, Y.; Zou, C. L.; Zhang, W.; Yao, J.; Zhao, Y. S. *J. Am. Chem. Soc.* **2016**, *138* (7), 2122–2125.

(152) Oulton, R. F.; Sorger, V. J.; Zentgraf, T.; Ma, R.-M.; Gladden, C.; Dai, L.; Bartal, G.; Zhang, X. *Nature* **2009**, *461* (October), 629–632.

(153) Sidiropoulos, T. P. H.; Roder, R.; Geburt, S.; Hess, O.; Maier, S. A.; Ronning, C.; Oulton, R. F. *Nat Phys* **2014**, *10* (11), 870–876.

(154) Siegman, A. E. *Lasers*; University Science Books: Sausalito, California, 1986.

(155) No, Y. S.; Choi, J. H.; Ee, H. S.; Hwang, M. S.; Jeong, K. Y.; Lee, E. K.; Seo, M. K.; Kwon, S. H.; Park, H. G. *Nano Lett.* **2013**, *13* (2), 772–776.

(156) Smith, C. L. C.; Thilsted, A. H.; Pedersen, J. N.; Youngman, T. H.; Dyrnum, J. C.; Michaelsen, N. A.; Marie, R.; Kristensen, A. *ACS Nano*.

(157) Huang, K. C. Y.; Seo, M.-K.; Sarmiento, T.; Huo, Y.; Harris, J. S.; Brongersma, M. L. *Nat. Photonics* **2014**, *8* (3), 244–249.

(158) Geiselmann, M.; Marty, R.; Renger, J.; García De Abajo, F. J.; Quidant, R. *Nano Lett.* **2014**, *14* (3), 1520–1525.

List of Publications

This thesis is based on the following publications:

1. **Esteban Bermúdez-Ureña**, Mark P Kreuzer, Stella Itzhakov, Hervé Rigneault, Romain Quidant, Dan Oron, Jérôme Wenger. "Excitation enhancement of a quantum dot coupled to a plasmonic antenna" Advanced Materials **24** (44), OP314-OP320 (2012).
2. **Esteban Bermúdez-Ureña**, Carlos Ballestero, Renaud Marty, Michael Geiselmann, Ilya Radko, Yury Alaverdyan, Tobias Holmgraad, Esteban Moreno, Francisco J. Vidal, Sergey Bozhevolnyi, Romain Quidant. "Coupling of individual quantum emitters to channel plasmons". Nature Communications 6:7883 (2015).
3. **Esteban Bermúdez-Ureña**, Gözde Tütüncüoglu, Javier Cuerda, Cameron LC Smith, Jorge Bravo-Abad, Sergey I Bozhevolnyi, Anna Fontcuberta i Morral, Francisco J García-Vidal, Romain Quidant. "Plasmonic waveguide-integrated nanowire laser". *Nano Lett.*, **2017**, *17* (2), pp 747–754.
4. **Esteban Bermúdez-Ureña,** Javier Cuerda, Luca Francaviglia, Gözde Tütüncüoglu, Cameron LC Smith, Jorge Bravo-Abad, Sergey I Bozhevolnyi, Francisco J García-Vidal, Anna Fontcuberta i Morral, Romain Quidant. "Quantum dots in GaAs/$Al_xGa_{1-x}As$ core-shell nanowires coupled to plasmonic waveguide modes". *under preparation.*

Other publications during the course of this thesis:

1. P. Berto, **Esteban Bermúdez-Ureña**, P. Bon, R. Quidant, H. Rigneault, G. Baffou. "Quantitative absorption spectroscopy of nano-objects" Physical Review B **86** (16), 165417 (2012).
2. Guillaume Baffou, **Esteban Bermudez-Ureña**, Pascal Berto, Serge Monneret, Romain Quidant, Herve Rigneault. "Deterministic Temperature Shaping using Plasmonic Nanoparticle Assemblies". Nanoscale **6**, 8984-8989. (2014).
3. Hadrien ML Robert, Franziska Kundrat, **Esteban Bermúdez-Ureña**, Hervé Rigneault, Serge Monneret, Romain Quidant, Julien Polleux, Guillaume Baffou. "Light-Assisted Solvothermal Chemistry Using Plasmonic Nanoparticles". ACS Omega **1**, 2-8 (2016).
4. Guillaume Baffou, Pascal Berto, **Esteban Bermúdez-Ureña**, Romain Quidant, Serge Monneret, Julien Polleux, Hervé Rigneault. "Photoinduced heating of nanparticle arrays". ACS Nano **7**, 6478-6488 (2013).
5. Kumar Balla, N., Rendon-Barraza, C., Hoang, L. M., Karpinski, P., **Bermúdez-Ureña, E**., & Brasselet, S. "Polarized nonlinear nanoscopy of metal nanostructures". *ACS Photonics*, **2017**, *4* (2), pp 292–301.